2008

Modeling and growth of the 3C-SiC heteroepitaxial system via chloride chemistry

Meralys Reyes-Natal
University of South Florida

Modeling and Growth of the 3C-SiC Heteroepitaxial System via Chloride Chemistry

by

Meralys Reyes-Natal

A dissertation submitted in partial fulfillment
of the requirements for the degree of
Doctor of Philosophy
Department of Chemical Engineering
College of Engineering
University of South Florida

Co-Major Professor: Stephen E. Saddow, Ph.D.
Co-Major Professor: John T.Wolan, Ph.D.
Norma A. Alcantar, Ph.D.
Andrew M. Hoff, Ph.D.
Ryan Toomey, Ph.D.
Olle Kordina, Ph.D.

Date of Approval:
October 24, 2008

Keywords: homogeneous nucleation, hydrogen chloride, computerized fluid dynamics, thermodynamic equilibrium, epitaxial layers

Dedication

I would like to dedicate this dissertation to my family, especially to my parents for raising me with strong moral values and an enormous will to become the best I can be. I would also like to dedicate this work to my husband, for supporting me these past years and helping me achieve my most important growth experiment, Sofia. Without all of you I won't be the person I am today. Thank you.

Acknowledgments

There are many people I would like to acknowledge for their support and guidance throughout my dissertation work. First, I would like to express my gratitude to my co-major professors Dr. Stephen E. Saddow and Dr. John T. Wolan. They have been my most loyal mentors and friends throughout my graduate research studies. Thank you for making this experience possible for me. Next, I would like to thank Dr. Norma Alcantar, Dr. Ryan Toomey, Dr. Andrew M. Hoff, and Dr. Olle Kordina for accepting to be part of my committee. I am truly grateful for their interest in my research and their continued advice to ensure the success of my dissertation.

Next, I wish to thank Suzie Harvey for assisting me in my research and Dr. Y. Shishkin for his continued advice and support during process development. I extend my appreciation to past and current members of the SiC group; especially to Chris Frewin, I. Haselbarth, and Chris Locke for ensuring reactor operations ran effortlessly. I would also like to thank Dr. C. Colletti and Alexandra Oliveros for film characterization support. I would also like to show appreciation to Dave Edwards, USF-COT at Largo, FL for providing SEM and AFM support. Additionally I would like to acknowledge the use of the services provided by Research Computing at the University of South Florida.

This work was supported by grants from the Office of Naval Research under grant No. W911NF-05-2-0028 (C.E.C Wood) and the Army Research Laboratory under grant No. DAAD19-R-0017 (B. Geil), which are gratefully acknowledged.

Table of Contents

List of Tables

List of Figures

Modeling and Growth of the 3C-SiC Heteroepitaxial System via Chloride Chemistry

Meralys Reyes-Natal

ABSTRACT

This dissertation study describes the development of novel heteroepitaxial growth of 3C-SiC layers by chemical vapor deposition (CVD). It was hypothesized that chloride addition to the "traditional" propane-silane-hydrogen precursors system will enhance the deposition growth rate and improve the material quality via reduced defect density.

Thermodynamic equilibrium calculations were performed to obtain a criterion for which chloride specie to select for experimentation. This included the chlorocarbons, chlorosilanes, and hydrogen chloride (HCl) chloride containing groups. This study revealed no difference in the most dominant species present in the equilibrium composition mixture between the groups considered. Therefore, HCl was the chloride specie selected to test the hypothesis.

CVD computerized fluid dynamic simulations were developed to predict the velocity, temperature and concentration profiles along the reactor. These simulations were performed using COMSOL Multiphysics and results are presented.

The development of a high-temperature (1300 ºC -1390ºC) 3C-SiC growth process resulted in deposition rates up to ~38 μm/h. This is the highest value reported in the literature to date for 3C-SiC heteroepitaxy. XRD FWHM values obtained varied from 220 to 1160 arcsec depending of the process growth rate or film thickness. These values are superior or comparable to those reported in the literature. It was concluded from this study that at high deposition temperatures HCl addition to the precursor chemistry had the most significant impact on the epitaxial layer growth rate.

Low-temperature (1000-1250ºC) 3C-SiC growth experiments evidenced that the highest deposition rate that could be attained was ~2.5 μm/h. The best quality layer achieved in this study had a FWHM of 278 arcsec; which is comparable to values

reported in the literature and to films grown at higher deposition temperatures in this study. It was concluded from this work that at lower deposition temperatures the HCl addition was more beneficial for the film quality by enhancing the surface. Surface roughness values for films grown with HCl additive were 10 times lower than for films grown without HCl.

Characterization of the epitaxial layers was carried out via Nomarski optical microscopy, FTIR, SEM, AFM, XRD and XPS.

Chapter 1: Introduction

1.1 Overview

Silicon carbide (SiC) is a group IV-IV compound semiconductor that is highly regarded as a suitable material for a myriad of high-voltage, high-frequency and high-temperature device applications under which conventional semiconductors cannot adequately perform. To date, silicon is the semiconductor material of preference for a majority of electronic devices. However, Si-based technology is limited in electronic device performance to temperatures below 250ºC and to temperatures below 600ºC in mechanical device performance.[1,2] SiC is expected to overcome the limitations imposed by silicon-based (Si) technology, mainly due to its excellent physical, chemical, mechanical and electrical properties. Despite the promising potential of SiC and the theoretical studies that suggest its advantages, its technological widespread use has being hindered mainly by challenges associated with the material fabrication. Typical technological barriers that must be overcome include: high growth temperatures, low growth rates, high defect density and a lack of high quality crystalline substrate material.

This dissertation research explores the heteroepitaxial growth of 3C-SiC layers by CVD using chloride addition to the SiH_4-C_3H_8-H_2 chemistry. The hypothesis being that chloride based chemistry will aid to increase the epitaxial layers growth rate and material quality via reduced defects thus addressing two of the technical challenges mentioned above.

Two deposition temperature range (1000-1250ºC) and (1300-1390ºC) were studied during this work. Typically, high deposition temperatures (≥ 1350ºC) are required to ensure high quality films and high deposition rates. However, the implementation of low deposition temperatures would be beneficial for device process fabrication. Lower process temperatures will eliminate or decrease problems due to interdependencies with other process steps during device fabrication processes. This will help to avoid problems

related to auto-doping, solid state diffusion and alleviate stresses in the epitaxial film. In addition, lower deposition temperatures are attractive for selective epitaxial growth (SEG) applications where lower deposition temperatures are needed to avoid damage to the required silicon dioxide (SiO_2) mask.[3]

In order to meet the intended goals of this work, the use of theoretical CVD calculations coupled with statistical design of experiments (DOE) techniques were implemented as major experimental strategies. The CVD theoretical calculations include: (1) a thermodynamic analysis of the product composition under equilibrium conditions to provide an insight in to the role of the chloride specie on deposition rate, (2) computerized fluid dynamic (CFD) calculations which provide information regarding the velocity, temperature and species concentration profiles along the CVD reactor. By using this approach, theoretical and empirical models with adjustable parameters were derived. Such simulations minimize the large number of expensive and time-consuming growth experiments that are typically required for the optimization of reaction chemistry.

To provide the reader with a better understanding of the main material under study, the remainder of this chapter describes the basic properties of SiC and the potential applications for this semiconductor material. In addition, a brief survey of SiC epitaxial growth methods along with an introduction to common crystal defects will be presented.

1.2 SiC crystallography

The basic building block of a SiC crystal consists of a stacking of tetrahedral units composed of four carbon atoms covalently bonded to a silicon atom positioned at the center as shown in Figure 1.1 (alternatively one can view this as four silicon atoms bonded to a single carbon atom but the result is equivalent). SiC crystals are then formed when multiple corners of this basic tetrahedron are joined forming crystal planes. However, disorder in the stacking periodicity of the planes during crystal formation may occur resulting in defective material formed by numerous dissimilar crystal structures called polytypes. In the case of SiC about 170 polytypes have been identified to date.[4] Among all polytypes only three possible crystal lattice structures are known to exist, namely cubic (C), hexagonal (H) and rhombohedral (R).[1,2]

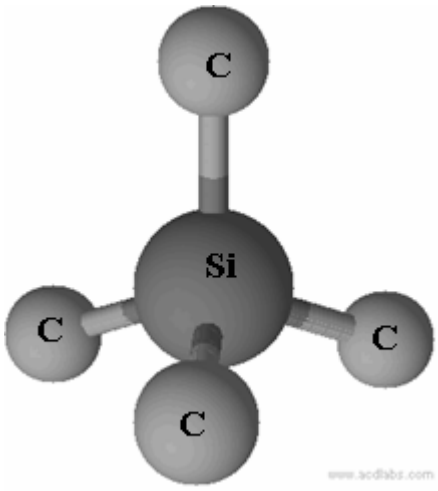

Figure 1.1 Illustration of a SiC tetrahedron that forms the basis for all SiC crystals. Four carbon atoms are covalently bonded to a silicon atom located at the center.[5] (Note an equivalent situation involves a single C atom bonded to four Si atoms).

While the variety of SiC polytypes is extensive, only a few are commonly used for electronic applications: 3C-SiC, 4H-SiC and 6H-SiC. The designation of each polytype follows a widely adopted nomenclature that identifies both crystalline symmetry (letter) and stacking periodicity (number). Figure 1.2 shows the stacking sequence of these common SiC polytypes. A more comprehensive study of SiC crystallography can be found elsewhere.[1,6,7]

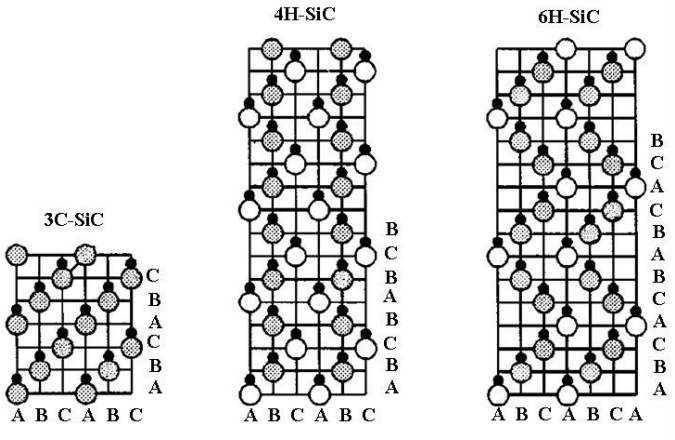

Figure 1.2 Stacking sequence for the most common SiC polytypes.[8]

This work focuses exclusively on the 3C-SiC polytype; commonly known as β-SiC, the only purely cubic polytype known to exist. Denoting each of the three bilayers within the SiC hexagonal frame with the arbitrary letters A, B and C, the stacking sequence for the 3C-SiC polytype is observed to be ABC-ABC… as shown in Figure 1.2. This specific stacking sequence results in a cubic zinc blende crystal structure.

3C-SiC potentially offers superior electrical properties compared to 4H-SiC and 6H-SiC; which include higher electron mobility and a higher electron saturation drift velocity.[4] These properties are of great advantage for the development of high-frequency and high-power switching devices.[9-11] In addition, 3C-SiC is isotropic which has inherent advantages in device operation compared with the highly anisotropic hexagonal polytypes. However, no suitable homoepitaxial technique is commercially available for 3C-SiC, thus making device realization more difficult. This is mainly due to challenges encountered during the 3C-SiC growth process (refer to section 1.4 for a more detailed discussion on 3C-SiC growth and process challenges). Therefore, the growth of 3C-SiC on Si substrates is of great importance in order to obtain high-quality material that can potentially be used as a substrate in the development of bulk 3C-SiC crystals as well as hetero-structure device fabrication.

1.3 SiC properties and applications

Although all the SiC polytypes have the same atomic composition, namely bi-layers of Si and C, each have a characteristic set of electrical properties due to the differences in the stacking sequence of the crystal planes. A comparison of some basic properties of the most common SiC polytypes compared with Si is presented in Table 1.1. As can be seen, many properties of SiC are superior to those of Si except for the mobility parameter.

The properties mentioned above; among others, are justification to choose SiC as a semiconductor material, but the importance of each property will depend on the intended application - i.e., high-temperature, high-power, or high-frequency. Many of these applications are possible for the most part because SiC possesses a wide bandgap, a

property in semiconductors that dictates the energy needed to break covalent bonds in the material and thus generate electrons in the conduction band.[12]

Table 1.1 Comparison of SiC and Si basic parameters at 300 K.[1,2,4,8]

Property	3C-SiC	4H-SiC	6H-SiC	Si
Melting point (ºC)	2827*	2827*	2827*	1415
Physical stability	Excellent	Excellent	Excellent	Good
Thermal conductivity (W/cm-ºC)	3.6	3.7	4.9	1.5
Thermal expansion coefficient (10^{-6}/ºC)	3.8	N/A	4.3 $\perp$ c-axis 4.7 $\parallel$ c-axis	1.0
Energy gap (eV)	2.4	3.2	3.0	1.1
Electron mobility (cm^2/V-s)	800	900	400	1400
Hole mobility (cm^2/V-s)	320	120	90	471
Critical breakdown electric field (MV/cm)	2.1	2.2	2.5	0.25
Saturated electron velocity (10^7 m/s)	2.5	2.0	2.0	1.0

*Sublimation temperature.

The wide bandgap of SiC makes it possible for high-temperature device operation. High-temperature operation is mainly attributed to the thermal ionization of electrons from the valence band to the conduction band.[13] At elevated temperatures the concentration of electron-hole pairs can be higher than the free carrier concentration from intentional impurity doping.[7,14] When this occurs, the material becomes intrinsic resulting in device failure because voltages can not be blocked due to the lack of a p-n junction.[7] It is believed that replacing Si technology with SiC will help to increase device operating temperatures and thus decrease the size of power-electronics modules. A powerful argument implies that SiC technology allows for a 50% increase in power and a 90 % decrease in weight and volume in power modules made of SiC vs. Si.[15] A simple example could be applied to hybrid electric vehicles (HEVs), where smaller, lighter and simpler electrical systems for HEVs would result in reduced vehicle weight and operational costs.

This may make HEVs more attractive and affordable so that greener and more efficient energy utilization can be realized.[16]

The high breakdown voltage and high thermal conductivity are perhaps the most significant properties of SiC for high-power, high-voltage and high-frequency devices. The breakdown voltage determines the maximum field that can be applied before the material breaks down.[13] Conversely the thermal conductivity is a measure of the material's ability to conduct and dissipate heat, which is of great importance for device reliability.[17] In SiC, the breakdown voltage is about an order of magnitude higher and the thermal conductivity is about 2-3 times higher than Si as shown in Table 1.1. The combination of such properties allow lower losses and higher power densities with a smaller on-resistance for high-power devices.[7,18] For high-frequency devices the high electric field strength implies that devices can be made smaller and therefore faster but still be able to hold a large voltage thus achieving high power output.[7,18] High-frequency devices may include metal oxide semiconductor field effect transistors (MOSFET's) and bipolar transistors, among others. However, power MOSFET's exhibit an advantage over bipolar transistors due to their high switching speeds, excellent safe operating area, and better output characteristics for device paralleling.[18]

Although most of the above discussion focuses on the electrical properties of SiC, this material is also attractive due to the combination of its electrical properties with its physical and mechanical properties. Microelectromechanical systems (MEMS) are a principal focus area which is being developed to take advantage of most of the properties of SiC. SiC is a very hard material with hardness values comparable to those of diamond and topaz.[2] In addition, SiC presents a high level of chemical inertness. This will be beneficial, for instance, in NASA space probes and landers that must operate under extreme conditions of high temperatures and pressures (~ 460ºC and 92 bar) and chemically harsh atmospheres such as that on Venus which is composed of highly concentrated sulfuric acid.[19] However, this advantage is also a drawback for device fabrication. Due to its chemical inertness, no efficient wet etchant exists for SiC that could be viable for manufacturing purposes. Consequently, the research community has adopted fabrication techniques based on bulk Si substrates for which fabrication

processes are fully developed.[2] SiC-based MEMS fabrication and device testing have been demonstrated for a variety of sensors for the measurement of temperature, gases, pressure and other parameters. In addition other structures such as resonators and atomizers have been achieved.[2,20] These structures could potentially be used in the fabrication of military and commercial gas turbines.

There is no doubt that SiC technology development could open the door to new systems that could impact a myriad of application sectors such aerospace, military defense, automotive, nuclear power instrumentation, satellites, etc. Therefore, the continued study of SiC growth processes as well as device fabrication techniques and testing is crucial to achieve the much needed scientific breakthroughs that will launch SiC as the preferred semiconductor material for harsh environment applications.

1.4 3C-SiC hetero-epitaxy

1.4.1 Growth process

Chemical vapor deposition (CVD) is the primary deposition technique for the growth of 3C-SiC epitaxial layers. A detailed theoretical background of CVD is discussed in Chapter 2. 3C-SiC has been hetero-epitaxially grown on Si substrates for many years due to the initial lack of commercially available bulk substrates, as mentioned earlier. Unfortunately, the heteroepitaxial growth techniques still fail to yield sufficiently high quality single crystal material for electronic device applications. Two of the main reasons for this are the mismatch in lattice coefficient (~20%) and mismatch in the coefficient of thermal expansion (CTE, ~8%) existing between 3C-SiC and Si. The large mismatches are the main cause of highly defective 3C-SiC/Si interfaces. This problem is typically reduced by introducing a carbonization process to the growth sequence as described below but, unfortunately, a highly defective interface remains.[21]

The 3C-SiC on Si hetero-epitaxial growth sequence is commonly performed in two stages: (i) carbonization of the silicon substrate and (ii) growth of the SiC layer. Sometimes an initial etching of the substrate is carried out before conducting these two stages.[21] This is done primarily to ensure removal of both the Si native oxide and surface damage caused in polishing processes. Therefore, an etching process provides a cleaner,

smoother surface before the growth sequence starts. The substrate surface is commonly etched by conducting a H_2 etching process. A more aggressive alternative utilizes diluted HCl in a hydrogen carrier gas, while a milder alternative includes a mixture of propane and hydrogen. The latter is sometimes preferred because the likelihood of forming silicon droplets is reduced.[22] However in this work an etch step was not employed as the material quality achieved was outstanding as will be discussed in later chapters.

The heteroepitaxial approach to grow 3C-SiC was not possible until the carbonization process was introduced by Nishino *et al.*[23] During the carbonization process a buffer layer formed on the Si surface by heating the substrate in the presence of a hydrocarbon diluted in the hydrogen carrier gas before growth.[24] This stage was performed at temperatures ranging from 700 ºC to 1300 ºC and yielded buffer layers several nanometers thick.[25-27] Even though the carbonization process is not fully understood, there has been speculation that this buffer layer aids to reduce the effect of the large lattice mismatch at the SiC/Si interface.[23,24]

After the carbonization process is performed, the substrate surface is ready for the growth stage at which time a Si containing precursor is added to begin the SiC deposition process. Typically 3C-SiC is grown at temperatures ranging from 1250 ºC to 1390 ºC (as a point of reference the Si substrate melting temperature is (1410 ºC). Studies performed on hot-wall CVD systems usually yield growth rates up to 13 μm/h.[26,28-30]

1.4.2 CVD growth precursors

The typical chemistry used for the epitaxial growth of 3C-SiC consists of hydrogen (H_2), propane (C_3H_8) and silane (SiH_4). In this gas mixture, hydrogen serves as a carrier gas. Other carrier gases used may include argon (Ar) and nitrogen (N_2). However, H_2 is typically preferred, mostly because of cost, high thermal conductivity, low viscosity, and low density which aid to ensure the laminar flow conditions necessary during the growth process. Also, it is believed that H_2 aids in the reaction process functioning as a light surface etchant during growth thus allowing for smoother and cleaner surfaces.[22]

The SiH_4 and C_3H_8 components of the gas chemistry provide the silicon and carbon growth precursors needed to form the desired film. Although these are the most popular compounds, alternative sources have been investigated by numerous research groups mainly due to the highly flammable and toxic nature of SiH_4.[31-35]

To solve the above challenges numerous organic compounds of silicon have been studied, which are often referred to as single precursors. These single precursors are of interest since they are safer to handle than SiH_4. It has also been suggested that since the original molecule already contains Si-C bonds, the Si-C bond formation at the substrate surface is more efficient.[31] Additionally, single precursors are known to offer better stoichiometric control of the gas mixture since they contain both silicon and carbon atoms.[32] Nakasawa *et al.* reported the formation of an interfacial buffer layer for 3C-SiC/Si(100) heteroepitaxy using monomethylsilane (MMS, or CH_3SiH_3) at temperatures as low as 450ºC-650ºC. It was also reported in this study that lower-temperature single crystal 3C-SiC deposition was possible at 900ºC yielding films without the formation of voids at the interface.[33] Ferro *et al.* reported 3C-SiC deposition rates of up to 7 μm/h at process temperatures of 1350ºC by using a hexamethylthysilane-propane (HMDS-propane, or the $Si_2(CH_3)_6$-C_3H_8) precursor system. However, they could not achieve lower deposition temperatures when using HMDS due to its stable nature.[31] Other single precursors used in 3C-SiC growth studies include: tetramethylsilane (TMS, or $Si(CH_3)_4$)[34], and methyltrichlorosilane (MTCS, or CH_3SiCl_3).[35] However all of these suffer from one drawback – the dual precursor system allows for accurate doping control via the gas inlet manipulation of the Si/C ratio using the site-competition effect pioneered by Larkin *et al.*[36] Thus a single-precursor, while attractive especially for MEMS applications, is less attractive for electronic devices where precise doping control is critical.

In addition to single source alternatives, the study of chlorosilanes has also been well explored. Chlorosilanes, specifically dichlorosilane (SiH_2Cl_2), has been employed in silicon homoepitaxy. From these studies it was observed that SiH_2Cl_2 provided a higher sticking coefficient on silicon surfaces, produced higher purity layers at lower deposition temperatures and provided a safer, less toxic environment than silane.[37] Ban *et al.*

conducted a thermodynamic analysis for silicon deposition using SiH_2Cl_2.[38] This study revealed that the main reactions occurring with dichlorosilane lead to the formation of other chlorosilanes and intermediate species such as Si_xCl_y. These intermediate species aid to increase the silicon atomic content in the gas mixture, making it more available to react thus raising deposition rate values.[38] The use of SiH_2Cl_2 has been applied to 3C-SiC heteroepitaxy yielding similar results.[25,28] Wang *et al.* produced 3C-SiC films on Si(100) substrates by using the SiH_2Cl_2-C_2H_2-H_2 precursor system at 750 ºC and 800 ºC, however the resulting films were amorphous and microcrystalline, respectively. However, Yagi *et al.* were able to obtain single crystalline layers using the same precursor chemistry at 1020 ºC by applying a layer-by-layer type of growth.[25]

A similar effect can be obtained when hydrogen chloride (HCl) is added to the standard H_2-C_3H_8-SiH_4 precursor system.[39] It has also been suggested that the addition of HCl allows for the enhancement of both deposition rates and surface morphology. As in the case of SiH_2Cl_2, chloride ions (Cl^-) preferentially attaches to the silicon species resulting in increased silane mole fractions in the gas mixture. This phenomenon is believed to reduce homogeneous nucleation of silicon in the gas phase which creates particulate precipitates. These particles limit the film growth rate by reducing the available silicon in the reaction chemistry.[40,41] In addition, it has been suggested that the presence of Cl^- in the gas chemistry improves the surface morphology of the epitaxial layers by etching high energy surface atoms during deposition due to the formation of HCl.[42] Gao *et al.* were able to achieve 3C-SiC growth on Si(100) surfaces using H_2-SiH_4-C_2H_4-HCl precursor chemistry at temperatures as low as 1000 ºC.[43] They reported that HCl improved the film structure and quality; for instance, the dislocation density decreased from 1.1 x 10^{10} cm^{-2} to 4.27 x 10^9 cm^{-2} when the Cl/Si ratio was increased from 0 to 50, respectively. A study performed as part of this research where HCl was added to the standard H_2-SiH_4-C_3H_8 gas chemistry allowed for a growth rate increase of 3 times the highest 3C-SiC deposition rate value reported in literature for hot-wall epitaxy (~13 μm/h).[44] X-ray diffraction (XRD) measurements of the full width at half maximum (FWHM) of these films are within 220-360 arcseconds; this is as good or better than values reported elsewhere (refer to Chapter 3).[45]

1.4.3 3C-SiC epitaxial film defects

Defects are undesireable in semiconductor films because they disrupt the crystal lattice periodicity which alters the band structure and scatters electrical carriers, and provide paths for electrical leakage and impurity diffusion.[46] The large lattice coefficient and CTE mismatches between SiC and Si are the main cause of defect generation and propagation in 3C-SiC films. Typically defects of zero dimensions (0D) through three dimensions (3D) are encountered in 3C-SiC epitaxial films. Some of these include interfacial voids, threading dislocations, stacking faults and precipitates. Since it is beyond the scope of this work to cover every defect observed, a brief discussion of some of the major defects is provided below.

Dislocations are one-dimensional (1D) defects which represent linear imperfections in the atomic array.[47] In general the introduction of dislocations into epitaxial layers may cause elastic distortions and band bending. In addition, dangling bonds are created along the core of the dislocation. Different types of dislocations include: misfit, threading edge and screw dislocations. Misfit dislocations occur when a missing or dangling bond is present between the substrate and the underlying layer as seen in Figure 1.3 .[48] A consequence of this defect is the formation of two threading dislocations at the end of each misfit dislocation. In addition, the presence of misfits induces stress into the layer as it grows.[49] The layer becomes unconstrained causing the insertion or removal of extra partial lattice planes that terminate in the dislocation line or misfit dislocation.[49,50] This is typically known as an edge dislocation as illustrated in Figure 1.4. External forces cause internal stress in the crystal which results in the movement of a plane. After the dislocation disappears, the crystal is completely stress free and plastically deformed leaving behind an elementary step.[50]

The density of misfit dislocations is dictated by the materials under consideration, therefore it can not be altered by the growth conditions. However the density of threading dislocations may be altered by using a buffer layer.[49] In the case of 3C-SiC this is achieved through the before mentioned carbonization process.

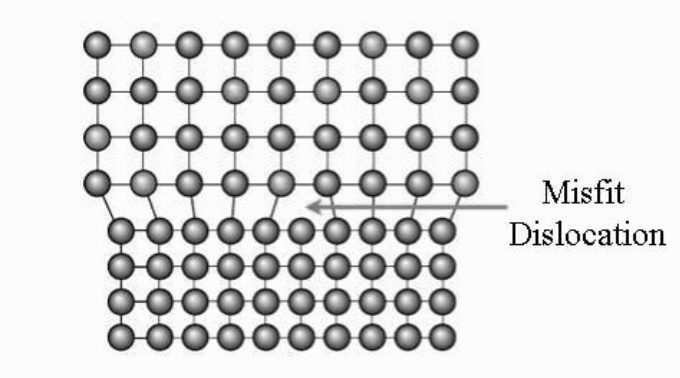

Figure 1.3 Schematic representation of a misfit dislocation. This defect is caused by the presence of a dangling bond between the substrate and the underlying layer due to a lattice coefficient mismatch.[48]

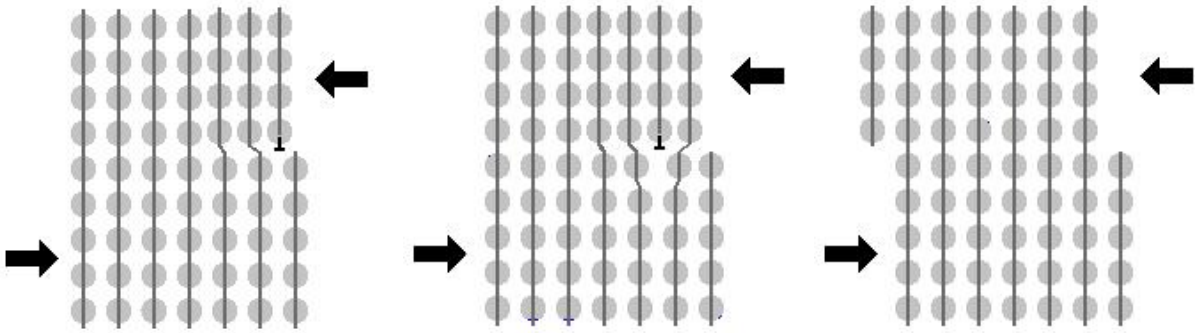

Figure 1.4 Schematic representation of the formation of an edge dislocation. External forces cause internal stress in the crystal which results in the movement of a plane.[50] (a) A biaxial force is present on the top of the crystal which causes a broken bond which (b) then continues to propagate through the crystal until eventually (c) an edge is produced resulting in the lowest system energy.

Stacking faults, twin boundaries, grain boundaries, and anti-phase domain boundaries are typical examples of two-dimensional defects. High densities of stacking faults and twins have been typically observed in 3C-SiC layers regardless of the growth conditions used.[51-53] Stacking faults and twins are known to form due to facetted growth and misfit stress-induced deformation.[49] Stacking faults are misalignments of the crystal planes and they can be classified as intrinsic or extrinsic depending on how they are formed. An intrinsic stacking fault is produced by vacancy agglomeration (Figure 1.5

(a)), while the extrinsic stacking fault is formed by interstitial agglomeration (Figure 1.5 (b)).

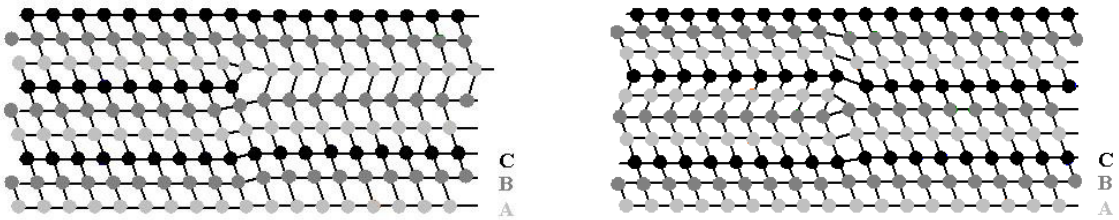

Figure 1.5 Illustration of stacking faults which are defects caused by the misalignments of the crystal planes: (a) intrinsic and (b) extrinsic stacking faults.[50]

Twin boundaries occur when two crystals of the same type inter-grow in such a way that a slight misorientation exists between them. Both crystals are often the mirror image of each other and atoms are shared among them as observed in Figure 1.6.[54] Twin formation is detrimental for growing layers since it may lead to misoriented or polycrystalline phases.[51] Yun *et al*. were able to successfully suppress twin formation by performing a two-step epitaxial process consisting of a nucleation step followed by the growth of 3C-SiC. This nucleation stage appeared to be more efficient than the normal carbonization process.[51]

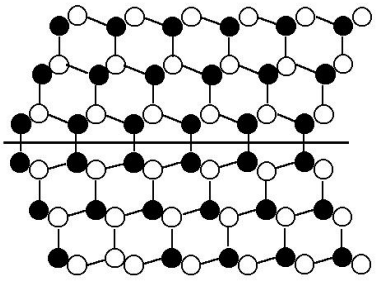

Figure 1.6 Representation of a twin boundary defect. Two slightly misoriented crystals of the same type inter-grow and share atoms.[50] Note that there are no dangling bonds associated with this form of defect but they still impact carrier transport in the films and are therefore detrimental to device performance.

1.5 Summary

SiC is a robust material with many properties superior to Si. In order to develop SiC growth and fabrication techniques, it is crucial to achieve the much needed scientific breakthroughs that will launch SiC as the next generation semiconductor system. However, despite the knowledge of the potential of SiC and the theoretical studies that suggest its numerous advantages, its technological widespread use has been hindered mainly by challenges associated with material fabrication. Typical technological barriers that must be overcome include: high growth temperatures, low growth rates, high defect density and resulting lack of high crystalline quality material.

Therefore, this work was undertaken to investigate the growth of SiC, specifically 3C-SiC, with the aim to overcome some of these technological barriers. A chloride-based CVD precursor chemistry was applied in the heteroepitaxial growth of 3C-SiC on Si (001) surfaces via horizontal hot-wall CVD. To assist and guide the reader, Chapter 2 discusses CVD theory and theoretical simulations performed. In Chapter 3 the development of a high-temperature 3C-SiC process via HCl as a growth additive is presented. The same precursor chemistry was then used to demonstrate low temperature growth of 3C-SiC layers which is presented in Chapter 4. Finally, Chapter 5 provides a summary of the research performed as part of this work followed by experimental trends and suggestions for future work.

Chapter 2: Chemical Vapor Deposition

2.1 Overview

Among the main objective of this study was to determine the effect of chloride addition to the SiH_4-C_3H_8-H_2 precursor chemistry system via thermodynamic equilibrium calculations and to develop CVD process simulations in order to predict the velocity, temperature and species concentration profiles along the reactor; the ultimate goal being prediction of film deposition rates. The aim of this type of calculation is to obtain a deeper understanding of the SiC deposition process and to facilitate process optimization resulting in improved film material. In addition, the simulation work will enable modeling of changes in the reactor hardware and effects of changing process parameters without direct experimentation.

In order to obtain such models, in depth understanding of process thermodynamics, chemical kinetics and transport phenomena are needed. The following sections are intended to introduce the theoretical aspects of these disciplines applicable to CVD, developing the different models and to present the model results.

2.2 Chemical vapor deposition

CVD is a deposition technique in which gases decompose and chemically react near or on a surface with the aim to synthesize a solid product.[42] CVD can be performed in a closed or open system reactor. However, nowadays most deposition processes are carried out in open reactors where the effluent species are removed from the chamber after the reaction takes place. Various open system reactor designs have been used for the development of CVD process including horizontal, vertical, semi-pancake, barrel, and multiple wafer.[42,55,56] Among the most popular geometries are the vertical and horizontal tube reactors.[42] Both of these geometries can be further grouped into cold-wall and hot-wall designs. In the cold-wall design the sample is kept at the required temperature while

all other surfaces bound to the reacting gas flow pathway are at a greatly reduced temperature. This is achieved by surrounding the reactor tube with a cooling jacket which, in theory, causes the reaction to occur only on the hot sample keeping all the remaining surfaces as free as possible of deposits due to a slower reaction rate. However, severe natural convection may occur due to the steep temperature gradient around the substrate. Therefore, one drawback in the cold-wall reactor is the difficulty in maintaining a uniform temperature over the sample area. Such concerns can be eliminated or significantly reduced if the entire chamber is heated at a uniform temperature. This type of heating is achieved if a hot-wall design is implemented as is the case for this work.

Numerous parameters control and affect the CVD process and, hence, the properties of the deposited film. These parameters can be classified into reactor design variables and operator variables. Reactor design variables can include the susceptor tilt angle, gas inlet geometry, wafer/carrier configuration, wafer/reactor wall configuration, exhaust configuration, among others. However, operator variables are the primary control factors for any reactor geometry; these include gas flow rate, gas composition, temperature, reactant chemistry and temperature profile. For instance, the temperature is crucial as it controls the thermodynamics and the kinetics of the process. Optimal temperature must be achieved and maintained in order for gas and surface reactions to overcome activation barriers. Any variance in temperature may lead to inferior material morphology or quality due to variation in the reactions or kinetics.[56]

2.2.1 USF hot-wall CVD system

The USF CVD reactor was designed to be horizontal with hot-walls as illustrated in

Figure 2.1. This reactor was custom built and modified by members of the USF SiC research group.[57,58] The reactor chamber consists of a main quartz tube supported in place by two water cooled stainless steel end plates. The main growth components used during the deposition process are then loaded into this quartz tube. The gas line supply connects

to the stainless steel plate located at the reactor inlet. The gases then exit the other side of the plate through a gas diffuser. The diffuser's function is to provide uniform flow in which laminar flow conditions along the gas path prevail. The gas path is composed of an inner quartz liner that connects the diffuser with the reactor deposition area (i.e., hot zone) via graphite adaptors. The adaptors provide the necessary connections between the quartz liner and the hot zone; in addition they help to avoid overheating of the quartz liner. The hot zone is composed of an angled ceiling designed SiC coated graphite susceptor in which the sample is loaded using a polycrystalline plate. The hot zone is surrounded by a graphite foam insulating material to help maintain a fairly uniform temperature during the deposition process by minimizing heat losses to due radiation. Figure 2.2 illustrates a cross-section view of the USF CVD reactor's inlet quartz liner and hot-zone areas for visualization purposes.

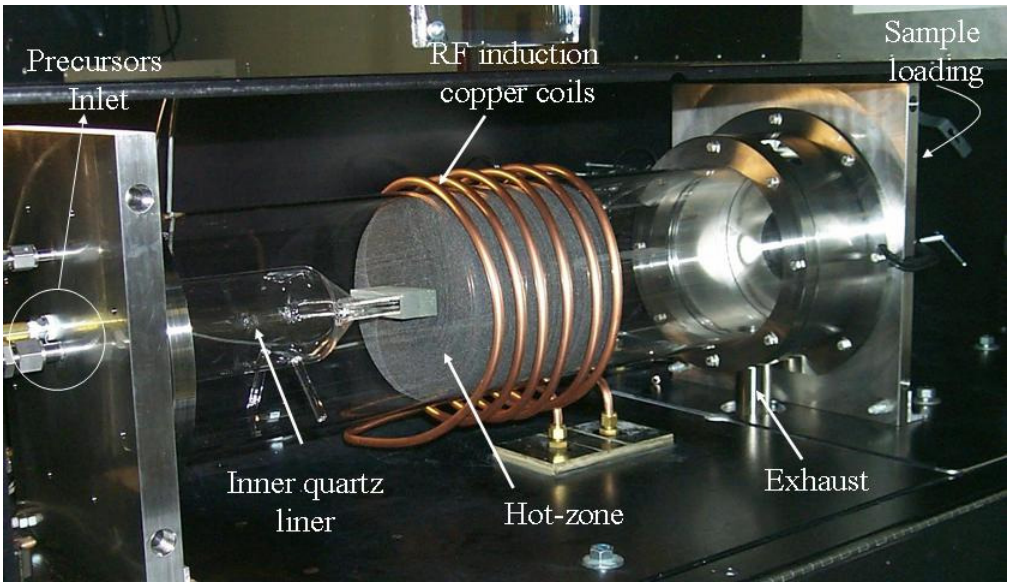

Figure 2.1 USF horizontal hot-wall CVD reactor.

The necessary heating to achieve the desired deposition temperatures is provided by an RF generator which produces radial heating via RF induction copper coils wrapped around the hot zone. An infrared pyrometer, which is connected to a computer interface, is used to monitor and control the temperature. The same computer interface is used to control mass flow controllers (MFCs) that regulate the gas flows introduced into the

reactor. Finally after deposition the effluent is transported out the chamber via negative pressure at the exhaust line via a vacuum pump which also is used to control the deposition pressure.

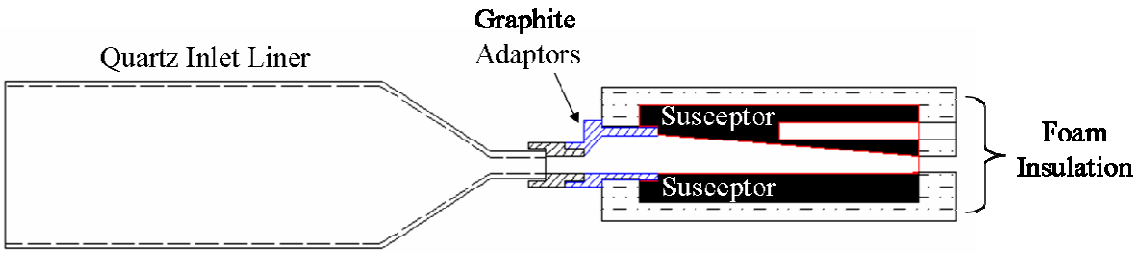

Figure 2.2 Cross-section view sketch of the USF CVD reactor. Sketch provided by I. Hasselbarth, University of South Florida.

At the time this work was conducted the reactor used in this research, named MF1, supported processes such as the epitaxial growth of 3C-SiC and 4H-SiC, H_2 etching, implant annealing and epi doping with nitrogen (N_2) gas. A second reactor named MF2 solely dedicated for 3C-SiC processing was also available. The standard dual precursor chemistry (C_3H_8-SiH_4) with H_2 as the primary carrier gas was available; in addition Ar was also accessible as a secondary carrier gas option or cooling gas. The system also supported halocarbon chemistry including HCl and CH_3Cl. The reactor is capable of process temperatures up to 1800ºC and pressures from 75 Torr to 760 Torr.

Two different reactor geometries were used to conduct the deposition experiments in this work using reactor MF1; for simplicity they will be referred as Geometry I and Geometry II. Geometry I included the use of three adaptors, a 140 mm long graphite susceptor and a hexagonal shape insulating foam. A 3C-SiC growth process on 8 mm x 10 mm Si die samples was developed using Geometry I (refer to Chapter 3). However, initial experimentation indicated that large temperature gradients were being formed at the susceptor causing film quality degradation and, on occasions, substrate melting when the process was transferred for growth on 50 mm substrates.[59] In order to solve this problem a study was performed by S. Harvey and Dr. Y. Shishkin of our group in which it was concluded that a reactor geometry change was necessary to minimize/solve the temperature gradient problem in the reactor.[59] As a result Geometry II was applied.

Geometry II consisted of a round shape insulating foam with an elongated graphite susceptor (210 mm). In addition, Geometry II used two adaptors instead of three. In both geometries an angled ceiling susceptor design was used. Table 2.1 summarizes the properties of the two different reactor geometries used during this work.

Table 2.1 Description of the reactors geometries considered in this study.

Reactor Component	Geometry I	Geometry II
Insulating foam shape	hexagonal	round
Susceptor design	angled ceiling	angled ceiling
Susceptor length	140 mm	210 mm
Number of adaptors	3	2

2.2.2 CVD thermodynamics

The main objective of this study was to investigate the introduction of chloride species into the growth chemistry; the hypothesis being to increase the epitaxial layers deposition growth rate and to improve the resulting material quality via reduced defects. In order to determine the chloride specie to be selected for the experiments, a theoretical study was performed first to establish a criterion for gas source selection. As such, a thermodynamic equilibrium study of the CVD product mixture composition was performed to monitor the effect of the chloride specie on the major effluent species composition.

2.2.2.1 Thermodynamic equilibrium

Thermodynamic equilibrium calculations applicable to CVD systems are based on the fact that the total Gibbs free energy (G) of a closed system should decrease during an irreversible process when the system is operating at constant temperature (T) and pressure (P). Therefore, at equilibrium conditions, the change in Gibbs free energy of reaction (ΔG_{rxn}) attains a minimum or the differential change in Gibbs free energy approaches zero ($(dG)_{T,P} \rightarrow 0$). As a reference, the Gibbs free energy is defined as the

thermodynamic potential which measures the "useful" or process-initiating work obtainable from an isothermal, isobaric thermodynamic system.[60]

The CVD reactor can be described as an open system which typically involves rapid changes. But when long reaction times are considered the expressions developed for closed systems can also be applied to open systems given the assumption that once equilibrium is reached, no further changes occur and the system still continues to operate at the same constant T and P. Two different approaches are often used to perform the Gibbs free energy minimization analysis: (1) the non linear method and (2) the more generalized method based on the fact that at equilibrium the total Gibbs free energy has a minimum value.

The non linear method utilizes equilibrium constants to obtain the partial pressure of the species; this method is useful for less complex systems where there are a small number of known significant species and when information of the reaction pathways, as well as what phases are formed, is known. However, the generalized method is independent of the reaction pathways and is more applicable to computer routine solution techniques. Hence the latter method is generally more suitable especially for complex chemical systems like CVD. Therefore calculations in this work will be performed by using the generalized method.

2.2.2.2 Gibbs free energy minimization

The minimization routine assumes that the Gibbs free energy for a single phase system is defined as in Equation 2.1:

$$(G)_{T,P} = g(n_1,n_2,\ldots,n_N) \qquad \text{Equation 2.1}$$

where T is temperature, P is pressure and n represents the number of moles. The solution approach involves finding the set n_i at constant T and P such that $(dG)_{T,P} \rightarrow 0$. The minimization procedure is subject to the conservation of mass. That is, the number of atoms of a specific element must be conserved. For example, a gas mixture containing one mole of SiH_4 and one mole of H_2 will contain one mole of Si atoms and six moles of

H atoms. The total number of atomic masses of the k^{th} element in the system can be defined as A_k. Then the number of atoms of the k^{th} element present in each molecule of chemical specie *i* is a_{ik}. As a result, the material balance can be expressed as:

$$\sum_i n_i a_{ik} - A_k = 0 \qquad (k = 1,2,...,w) \qquad \text{Equation 2.2}$$

where w is the total number of elements comprising the system. Upon applying the method of Lagrange's undetermined multipliers to the materials balance constraint, a new function (F) is formed by adding to G the materials balance sum over the k^{th} element. Then,

$$F = G + \sum_k \lambda_k \left(\sum_i n_i a_{ik} - A_k \right) \qquad \text{Equation 2.3}$$

This equation is identical to Equation 2.2 since the summation term is equal to zero. However, the partial derivatives of G and F are different due to the second term in the right hand side of Equation 2.3 The minimum of the functions G and F occurs when $(\partial F/\partial n_i)_{T,P,nj} \rightarrow 0$. Then

$$\left(\frac{\partial F}{\partial n_i} \right)_{T,P,nj} = \left(\frac{\partial G}{\partial n_i} \right)_{T,P,nj} + \sum \lambda_k a_{ik} \rightarrow 0 \qquad (i = 1, 2,..., N) \qquad \text{Equation 2.4}$$

The first term in the right hand side of Equation 2.4 is known to be the chemical potential, which for gas phase reactions and standard states as pure ideal gases can be expressed as:

$$\mu i = G_i^o + RT \ln \left(\frac{\hat{f}}{P^o} \right) \qquad \text{Equation 2.5}$$

where R is the ideal gas constant and P° is the pressure for the standard state. G_i^o can be set equal to zero for all elements in their standard states and $G_i^o = \Delta G_{f_i}^o$ for compounds. Finally, $\hat{f}$ is the fugacity, which when expressed in terms of the fugacity coefficient leads to $\hat{f} = y_i \hat{\phi}_i P$, then Equation 2.5 becomes:

$$\Delta G_{f_i}^o + RT \ln\left(\frac{y_i \hat{\phi}_i P}{P^o}\right) + \sum_k n_i a_{ik} = 0 \qquad (i = 1,2,...,N) \qquad \text{Equation 2.6}$$

Equation 2.6 represents N equilibrium equations and Equation 2.2 represents w material balances for a total of N + *w* equations (unknowns are n_i and λ_k). The values of $\hat{\phi}_i$ can be estimated depending if the phase can be considered ideal or real.[60-62]

2.2.2.3 Thermodynamic equilibrium simulations results

In this study NASA Glenn's Chemical Equilibrium with Application (CEA) computer program was used to perform the minimization routine.[61-63] The program allows the equilibrium composition calculation of complex mixtures through the minimization of Gibbs free energy by using the method described in section 2.2.2.2. The specific computer program used allows for the simulation of 90 chemical species if SiH_4-C_3H_8-H_2 gas system is used and 120 chemical species for the SiH_4-C_3H_8-H_2-HCl gas system. It also allows for the addition of 5 condensed species in both cases.

In order to determine the effect of the addition of chloride species into the SiH_4-C_3H_8-H_2 equilibrium mixture composition; simulations were performed including the following groups: chlorocarbons, chlorosilanes and hydrogen chloride (HCl). Table 2.2 lists all the species considered within these groups. In the following discussion thermodynamic simulation results will be presented using the process parameters of two 3C-SiC deposition processes, namely with and without chloride additive, developed as part of this work.

Table 2.3 summarizes the process parameters of these two processes which were used as input parameters to obtain the thermodynamic equilibrium results. The process parameters for the gaseous species represent the respective gas mole fraction.

Table 2.2 Summary of chloride species considered in the thermodynamic simulations.

Species		
Chlorocarbons	Chlorosilanes	Other
CCl_4	$SiCl_4$	HCl
$CHCl_3$	SiHCl	
CH_2Cl_2	SiH_2Cl_2	
CH_3Cl	SiH_3Cl	
C_2HCl		
C_2Cl_2		
C_2Cl_4		
C_2Cl_6		

Table 2.3 Process parameters for 3C-SiC deposition process with and without HCl addition.

Temperature (ºC)	Pressure (Torr)	y_{H2}	y_{C3H8}	y_{SiH4}	y_{HCl}	Si/C	Si/Cl
1385	100	0.99	2.0×10^{-4}	5.3×10^{-4}	--	0.9	--
1385	100	0.99	2.0×10^{-4}	5.3×10^{-4}	0.97×10^{-4}	0.9	6.5

Figure 2.3 (a) illustrates the predicted equilibrium composition as a function of temperature for the SiH_4-C_3H_8-H_2 precursor chemistry. The formation of solid beta-SiC over the entire temperature range considered for a total molar composition of one in the solid phase was predicted in the calculations. The gas phase composition in both cases evidenced that the most dominant species were H_2 (not shown) and H^-. The presence of H_2 is expected since it is the process carrier gas which is present in the inlet mixture in a much higher concentration than the precursors. The presence of atomic hydrogen may be

attributed to disassociation of H_2 due to reaction with the precursor molecules. It could also be the product of the propane and silane decomposition reactions.

CH_4, CH_3^-, C_2H_2, and C_2H_4 are predicted to be the major carbon species. CH_4 being the most dominant at temperatures below 1400ºC for which deposition process temperatures are typically carried out for 3C-SiC heteroepitaxy. Since C_3H_8 is not present as a thermodynamically possible chemical specie in the equilibrium gas phase mixture; it can be suggested that most of the molecular C_3H_8 will mainly crack to CH_3^-, CH_4, C_2H_2, and C_2H_4. However, the assumption that C_3H_8 will fully crack or that these are the only carbon species will be misleading since other carbon containing species, as well as the presence of C_3H_8 itself, might be favorable at molar fractions below 10^{-10}.

The most dominant silicon species were SiH^-, Si, and SiH_2. Note that SiH_4 cracked to some extent and then its concentration remained fairly constant over the entire temperature range. This may indicate that the thermal decomposition of SiH_4 may restrict the silicon content in the system thus limiting the growth rate. In addition, the presence of the Si_3 and Si_2 species can be noted at much lower mole fractions. The presence of these species may indicate the evolution of solid or liquid clusters of homogeneous nucleation which are a known cause of problems during growth. However, the simulation did not predict that they condensed either as a solid or a liquid. Finally, Si_2C and SiC_2 are present at low temperatures and their concentration increases with increasing temperature. These are recognized as a primary species for growth.

The study of chloride addition to the SiH_4-C_3H_8-H_2 precursor chemistry started with HCl addition since it is the simplest specie, containing only hydrogen and chlorine. The equilibrium composition mixture for the SiH_4-C_3H_8-HCl-H_2 precursor chemistry (Figure 2.3(b)) is not much different than that without HCl. The formation of solid silicon carbide as the only condensed specie over the temperature range studied was also predicted. In addition, the presence of H_2 (not shown) and H^- as major species in the gas mixture was noted, but in this case HCl and Cl^- were also present at high mole fractions.

The simulation predicted that the presence of HCl in the gas mixture does not have a dramatic effect on the carbon containing species. As can be seen in Figure 2.3(b), the same carbon containing species as in the process without HCl were observed and their

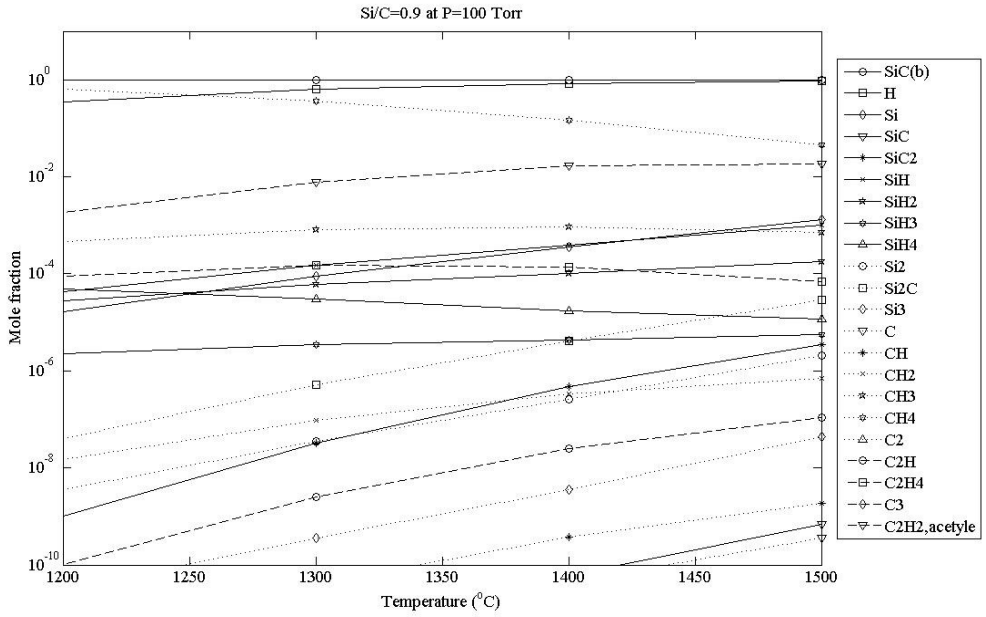

(a)

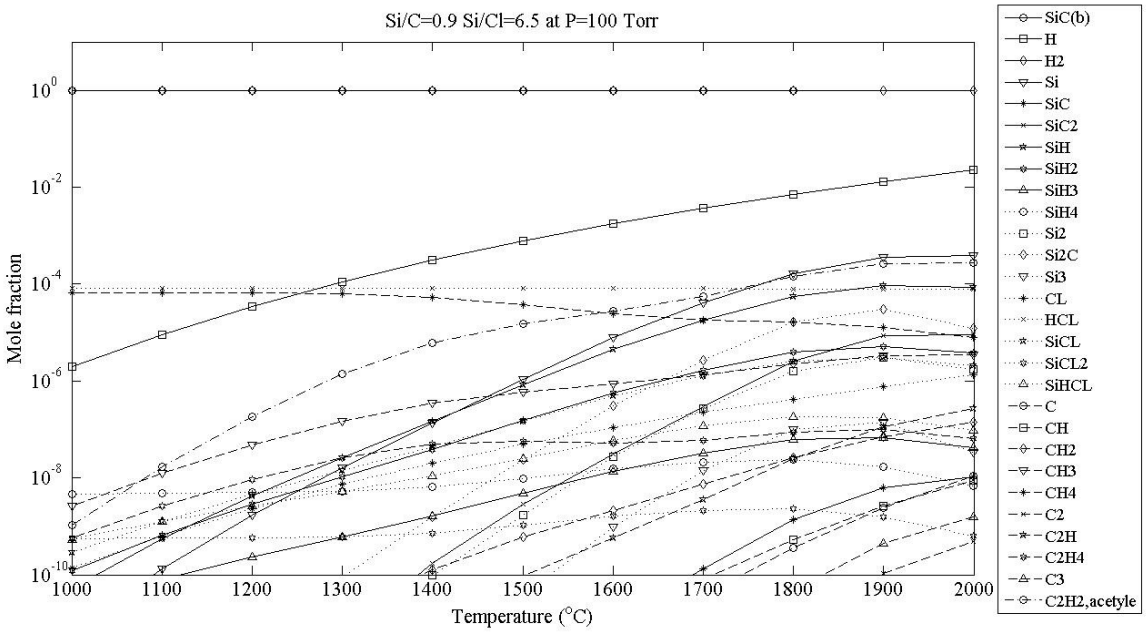

(b)

Figure 2.3 Predicted product equilibrium mixture composition for (a) SiH_4-C_3H_8-H_2 and (b). SiH_4-C_3H_8-HCl-H_2 precursor systems. Simulation performed using the NASA Glenn's CEA code.[61-63]

molar composition did not vary dramatically. However, it can be seen that chlorine preferentially bonds to silicon. This can be observed by the formation of species containing silicon and chlorine (SiHCl, SiCl, and $SiCl_2$) and suggests that HCl provides a different mechanistic reaction path that is going to affect mainly the Si containing reactions. As a result, the HCl addition is hypothesized to make Si species more available to react in the deposition mixture, resulting in a growth rate increase. This result is in agreement with other studies reported in literature.[40,41]

Adding HCl to the SiH_4-C_3H_8-H_2 precursor chemistry has been attributed to the suppress of homogeneous nucleation in SiC CVD epitaxial growth.[64] Therefore a reduction in the Si_3 and Si_2 species mole fraction is expected. The simulation results indicated that the Si_3 and Si_2 species are still present in the equilibrium mixture composition. However they only started to form at slightly higher temperatures compared to the no HCl process. This suggests that the introduction of chloride species suppressed homogeneous nucleation for a larger temperature range compared to that of the SiH_4-C_3H_8-H_2 precursor chemistry. Finally, no chlorocarbon species were observed via the simulation.

Because the minimization procedure is subject to the constraints of the mass balance; simulations using any of the chlorocarbon, chlorosilane or HCl species at the same process conditions, i.e. same process Si/C and Si/Cl, will lead to the same equilibrium mixture composition. Therefore, the simulation results are not shown to avoid redundancy.

In summary for the chlorocarbon system the following trends were observed. When higher C/Si ratios were explored the chlorine mole fraction increased and the Si_3 and Si_2 species mole fractions decreased dramatically. It was noted that chloride is not attached to any of the carbon containing species but only bound to Si or hydrogen once the precursor has cracked. It is not until higher C/Si ratios are simulated, i.e. using CH_2Cl_2 or chloroform, that some amounts of CH_3Cl can be seen. A final observation on the higher chlorinated chlorocarbons such as $CHCl_3$ is that at higher C/Si ratios carbon clusters such as C_3 begin to be seen in very low concentrations.

When the precursor system was studied using the chlorosilane species as an additive, similar trends were obtained. This is due to the mass balance constraint or conservation of mass that is identical to the previous cases. In conclusion, the thermodynamic equilibrium simulations indicated no significant difference in the equilibrium composition mixture between adding HCl or using chlorocarbons or chlorosilane species as the growth precursors. Therefore, this work will focus on HCl which is the simplest chloride studied. In addition the literature suggests that HCl promotes the enhancement of SiC growth in the 4H-SiC homoepitaxy so this work was focused on the 3C-SiC on Si heteroepitaxy system.[41,42,64]

2.2.3 CVD kinetics

A typical CVD process follows the generalized reaction path involving the steps depicted in Figure 2.4. (1) The reactant gases are transported to the deposition chamber. (2) After the gas enters the chamber in bulk flow, thermal dissociation, or cracking, forms the intermediate reacting gaseous species. (2a) Powders can be formed as a result of homogeneous gas phase reactions at temperatures higher than the decomposition temperature of the intermediate species. These powders may precipitate to the substrate surface and function as 3-D nucleation centers. As a result, defects are created in the film leading to lower quality material. This is typically the case when the precursor mole fractions reach the saturation point. (2b) Diffusion/convection of the intermediate species then occurs across the boundary layer at temperatures below the dissociation temperature of the intermediate species. The species eventually undergo steps 3-6. (3) Absorption of the reacting species occurs on the substrate surface so that surface reactions can take place. (4) The reacting species diffuse through the sample surface creating crystallization centers and eventually film growth. (5) The gaseous by-products desorb from the surface and travel across the boundary layer by diffusion/convection. (6) the unreacted species and gaseous by-products are transported from the deposition chamber via bulk flow.[42,55,56,65,66]

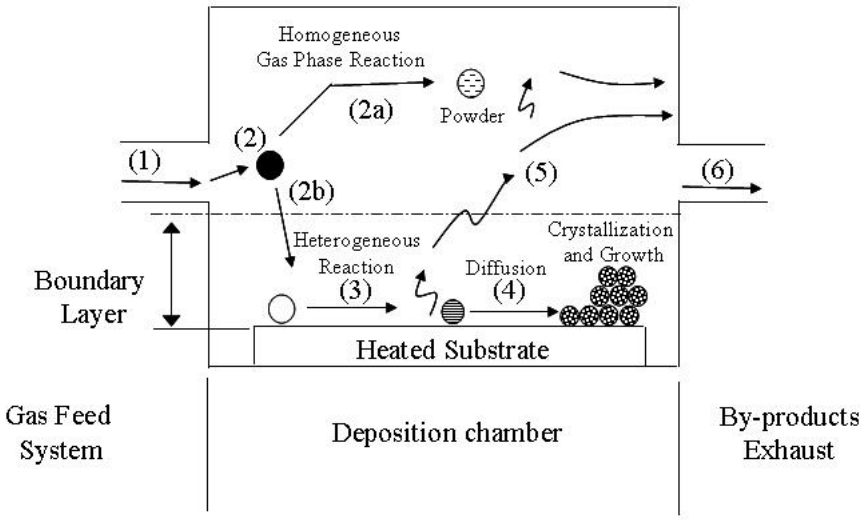

Figure 2.4 Schematic of CVD steps. Adapted from K.L. Choy.[65]

As explained above, the kinetics of a CVD process involves chemical reactions in the gas phase, on the substrate surface, chemisorption and desorption. However, a definite mechanism for SiC growth has not yet been determined. Ideally, the chemical kinetics of a CVD process could be derived from the analysis of all possible reaction pathways. As a consequence, a multi-step chemical reaction pathway is normally implemented when modeling deposition kinetics, as is the case in this work. This multi-step reaction pathway mainly includes the decomposition of the different precursors into numerous elementary reactions leading to a combined homogenous and heterogeneous reaction model. The reactions are described by their formula and rate equations.

2.2.3.1 Gas phase model

In the present study, C_3H_8, SiH_4 and HCl, with H_2 as a carrier gas have been used as the growth chemistry for all experiments and simulations. Therefore the complete reaction model will consist only on the decomposition of C_3H_8, SiH_4, and HCl and the set of reactions between the products of all decomposition reactions. Since incorporating all possible species resulting from this growth chemistry is outside the scope of this work; a selection of species was made where molecules with four carbon or silicon atoms were

excluded from the model. In addition, all reactions considered contribute to the model; therefore all considered species are either present or being produced during the reactions.

Appendix A lists the complete gas phase reactions considered in this work. Decomposition of propane was taken from the work of Petrov et al. and Danielsson et al.[67,68] The decomposition of silane and the formation of organosilicons was taken from the work of Danielsson which mainly combined the models from Coltrin et. al and Ho as well as other relevant publications.[67,69-71]. Finally, the chlorinated species reactions were taken from the work of several authors.[72-79]

The reaction rates for the gas phase reactions are described by the law of mass action (Equation 2.7) which states that the rate of any given chemical reaction is proportional to the product of the reactant concentrations.[80]

$$r_j = k_j^f \prod_{i \in react} c_i^{-\upsilon_{ij}} - k_j^r \prod_{i \in prod} c_i^{-\upsilon_{ij}} \qquad \text{Equation 2.7}$$

Where k_j^f and k_j^r denote the forward and reverse rate constants respectively. The concentration of species i is denoted c_i and ν_{ij} is the stoichiometric coefficients which are defined as negative for reactants and positive for products. The reaction rate constant is strongly dependent on temperature and will be modeled by means of the Arrhenius expression as given by Equation 2.8:

$$k = AT^n \exp\left(-\frac{E_A}{RT}\right) \qquad \text{Equation 2.8}$$

2.2.3.2 Surface reaction model

Surface reactions are characterized by reaction mechanisms such as chemiadsorption, dissociation, diffusion and desorption. A definite description of the surface process is not available, however studies of possible mechanisms have been reported.[70,73,74,81,82] In this work, the surface reaction model was taken from Veneroni *et al.* which provided a well documented complete set of reactions including those with

Cl^- containing species which are applicable to this work.[82] Appendix B lists the surface model considered.

For the surface reactions, the rate expression will be described by the Langmuir rate law which states that chemisorption will occur when a gas phase molecule reacts with an empty active site at the surface. Consequently, the adsorption/desorption rate will be proportional to the number of empty active sites at the surface as given by Equation 2.9.[80]

$$r_s = k_s \theta C_s \qquad \text{Equation 2.9}$$

where C_s is total number of active surface sites available, k_s is the temperature dependent rate constant for the surface reaction and θ is the surface coverage defined as the number of adsorbed molecules on a surface divided by the number of molecules in a filled monolayer on that surface.[80]

2.2.4 CVD transport and fluid dynamics

In addition to reaction mechanisms, a thorough understanding of mass and heat transport is critical in the design and modeling of CVD processes. The transport of mass determines the species concentration at the substrate surface; the transport of heat determines both the gas and substrate temperatures. Both transport mechanisms are obviously critical for film deposition rate, composition and uniformity.

During a CVD process it is desired to deliver the gas uniformly to the substrate in order to obtain uniform films and avoid intermixing of gas concentrations[56] Therefore it is crucial to determine in what flow regime the system is operating; laminar or turbulent. This type of flow is also known as streamline, which occurs when a fluid flows in parallel layers with no disruption between the layers. [83]

The dimensionless Reynolds (Re) number is used to determine whether flow conditions lead to laminar or turbulent flow regimes. This dimensionless number is described as the ratio of inertial forces to viscous forces.[83] In the case of a circular pipe the Re number can be calculated by using Equation 2.10.

$$\mathrm{Re} = \frac{\rho u D}{\mu}$$ Equation 2.10

where ρ is the mass density, u the velocity, D the characteristic diameter and μ the viscosity. For a flow to be considered laminar a Re number of less than 2100 must be obtained.[83]

In the case of laminar flow in circular pipe, in theory the velocity of the gas changes from zero at the walls to that of the bulk gas. This region of velocity change is called the "boundary layer". Figure 2.5 shows a sketch of the boundary layer. As can be seen, the fluid approaches the substrate surface at a uniform velocity and once in contact with the substrate, a velocity gradient is formed.

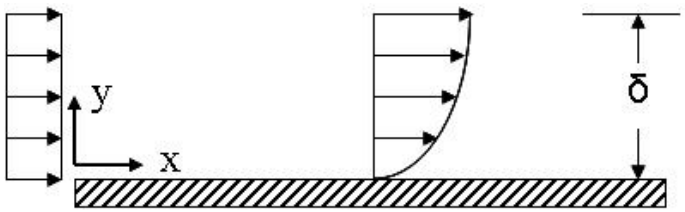

Figure 2.5 Boundary layer development near a flat surface. A velocity gradient is formed once the fluid contacts the surface. Adapted from A. Sherman.[56]

At high gas velocities the thickness of the boundary layer can be estimated using Equation 2.11, where D is the tube diameter for the case of a circular pipe. According to this equation the thickness of the boundary layer increases with reduced gas velocities and increased distance from the tube inlet.

$$\delta = \sqrt{\frac{D}{\mathrm{Re}}}$$ Equation 2.11

2.2.4.1 Rate limiting steps

In the generalized reaction path illustrated in Figure 2.4 the steps can be classified into two categories, namely mass transport and surface reaction steps. The slowest of

these steps determines if the process is mass transport or surface reaction limited as the surface reaction is considered the rate limiting step in the reaction mechanism.[66]

The surface reaction limited regime is dominated by the surface temperature rather than by what is occurring in the bulk gas. At low pressures and low surface temperatures, a large flux of reactants to the surface exists. Because of the low pressure and the small thickness of the boundary layer, the diffusion coefficients are large (diffusivity inversely proportional to pressure). Therefore the reactants reach the surface rapidly. The reactants react slowly due to the lower temperature so that there is an oversupply of reactants waiting to be consumed as seen in Figure 2.6(a).

In the mass transfer limited regime, the controlling factors are the reactants diffusion rate through the boundary layer and the by-product diffusion out through this layer. This situation typically occurs at high pressures (smaller diffusion rate) and high temperatures. Figure 2.6(b) provides a sketch of this situation. As a result of the high temperature, any molecule arriving at the surface will react quickly. In addition, the gas velocity is lowered and the boundary layer thickens making the diffusion of reactants more difficult.

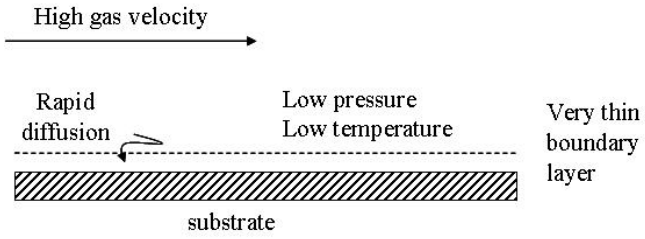

(a)

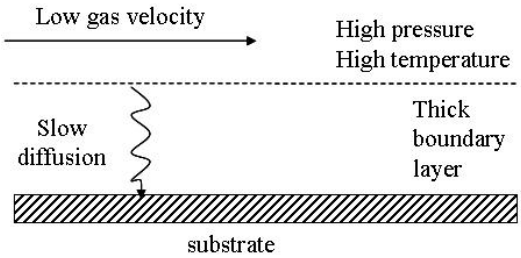

(b)

Figure 2.6 Representation of the rate limiting steps in a CVD reaction (a) surface reactionlimited and (b) mass transport limited.[66]

2.2.5 Computerized Fluid Dynamic (CFD) simulations

COMSOL Multiphysics and COMSOL Reaction Engineering Lab computer software were used to develop the CFD simulations in this work.[84] COMSOL Multiphysics is designed to couple transport phenomena, CFD or mass and energy transport to chemical reaction kinetics. While COMSOL Reaction Engineering Lab, solves the reaction kinetics material and energy balances. In addition, provides ready made expressions to calculate thermodynamic and transport properties.

2.2.5.1 Modeling domain

The simulation domain takes into account the gas path along the reactor. Since the depth of the flow domain is large, a 2D approximation is valid. This approximation takes advantage of the system's symmetry and assumes that variation with temperature and flow along the depth of the domain are small or negligible. Figure 2.7 illustrates the simulation domain.

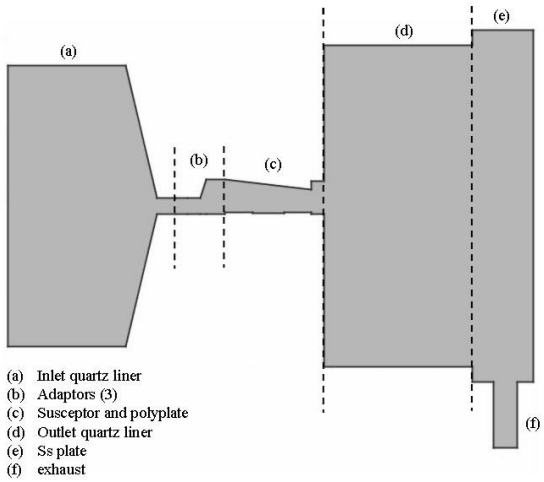

Figure 2.7 Reactor 2D modeling domain.

2.2.5.2 Governing equations

The Navier-Stokes equations for non-isothermal flow and the energy and mass balance equations describe the basis of the model. Equation 2.12 and Equation 2.13 represent the momentum balance and the continuity equations, which provide information regarding flow velocity. Equation 2.14 is the energy balance which provides information of the gas temperature distribution across the CVD reactor. Finally, Equation 2.15 represents the mass balance equation which will provide information of the species distribution along the reactor hot-zone.

$$\rho\frac{\partial u}{\partial t}-\nabla\cdot\eta\left(\nabla u+(\nabla u)^{T}\right)+\rho(u\cdot\nabla)u+\nabla p=F \qquad \text{Equation 2.12}$$

$$\frac{\partial\rho}{\partial t}+\nabla\cdot(\rho u)=0 \qquad \text{Equation 2.13}$$

$$\rho C_{p}\frac{\partial T}{\partial t}+\nabla\cdot\left(-kT+\rho C_{p}Tu\right)=Q \qquad \text{Equation 2.14}$$

$$\frac{\partial c_{i}}{\partial t}+\nabla\cdot\left(-D_{i}\nabla c_{i}+c_{i}u\right)=R_{i} \qquad \text{Equation 2.15}$$

In these equations; ρ denotes the gas density, u the gas velocity, p pressure, η the viscosity, κ the thermal conductivity, T temperature, C_p is the heat capacity and F is a volume force field.

2.2.5.3 Boundary conditions

The boundary conditions for the momentum balance impose a velocity at the reactor inlet. This velocity value refers to the maximum velocity which can be calculated from Equation 2.16 and Equation 2.17. u_{ave} is the average velocity, Q volumetric flow rate and A_c the cross section area. The volumetric flow rate was set to be the same as the carrier gas flow rate and the cross sectional area was that corresponding to the inlet.

$$u_{\max} = 2(u_{ave}) \quad \text{Equation 2.16}$$

$$u_{ave} = \frac{Q}{A_c} \quad \text{Equation 2.17}$$

The flow in our CVD reactor is mostly dictated by the H_2 carrier gas which will dominate the flow calculations performed. The input flow considered was 30,000 sccm which is the carrier gas flow used during the growth step for the 3C-SiC deposition process with and without the HCl additive (refer to Chapter 3). The properties of H_2 were obtained from the COMSOL Muliphysics software built in materials properties library.[85]

The no-slip condition was applied at the reactor walls; this condition sets all components of the velocity vector to zero. The boundary condition pressure with no viscous stress was imposed at the outlet. The pressure value for this calculation was 13.3 kPa (100 Torr) which is the pressure physically measured downstream in the reactor. Finally, the substrate will be treated as an interior boundary. These conditions are summarized by Equation 2.18 to Equation 2.20.

$$u = u_o \quad inlet \quad \text{Equation 2.18}$$

$$p = p_o \quad outlet \quad \text{Equation 2.19}$$

$$\left[\eta\left(\nabla u + (\nabla u)^T - \frac{2\eta}{3}(\nabla \cdot u)I\right)n = 0\right] \quad outlet \quad \text{Equation 2.20}$$

The boundary conditions for the energy balance required the inlet temperature, and the process temperature in the susceptor area as seen in Equation 2.21 and Equation 2.22. Equation 2.23 describes the convective flux boundary condition implemented at the reactor's outlet. Finally, a temperature gradient was considered at the substrate as summarized in Equation 2.24.

$$T = T_o \quad inlet \quad \text{Equation 2.21}$$

$$T = T_o \quad walls \quad \text{Equation 2.22}$$

$$n \cdot (-k\nabla T) = 0 \qquad \text{Equation 2.23}$$

$$T = T_{suf} \quad substrate \qquad \text{Equation 2.24}$$

The boundary conditions required for the mass balance are the species concentrations and the inlet, substrate and outlet of the system as summarized by Equation 2.25 to Equation 2.28. Convective flux was implemented at the outlet and insulation at the walls. For the adsorption and reaction at the surface the flux discontinuity boundary condition was imposed. Therefore;

$$c_i = c_{o,i} \quad inlet \qquad \text{Equation 2.25}$$

$$n \cdot (-D_i \nabla c_i) = 0 \quad outlet \qquad \text{Equation 2.26}$$

$$-n \cdot (N_1 - N_2) = N_i \quad substrate \qquad \text{Equation 2.27}$$

$$N_j = -D_i \nabla c_i + c_i u \quad substrate \qquad \text{Equation 2.28}$$

2.2.5.4 CFD simulations results

In order to perform the CFD calculations, COMSOL Multiphysics and the Reaction Engineering Lab module have to be used iteractively.[84] Appendix C explains the procedure followed to perform the CFD simulations.[84]

The gas temperature distribution across the CVD reactor for both susceptor geometries is depicted in Figure 2.8. It can be seen that in both cases the higher temperature region is located at the susceptor area where the deposition process takes place. Figure 2.9 shows the gas temperature profile along the susceptor area and the temperature at the susceptor area remained constant. A constant temperature is desired to avoid variations in the reaction kinetics that may lead to inferior material morphology or quality. Although large temperature gradients were observed experimentally via Si melt

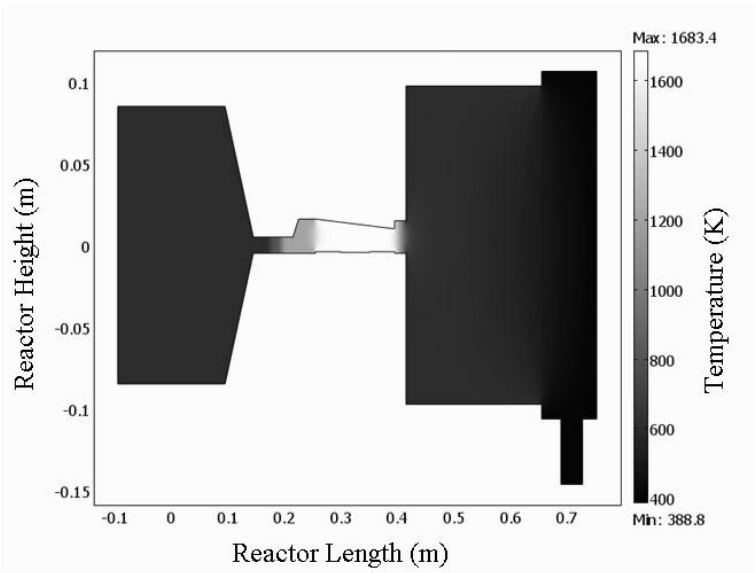

(a)

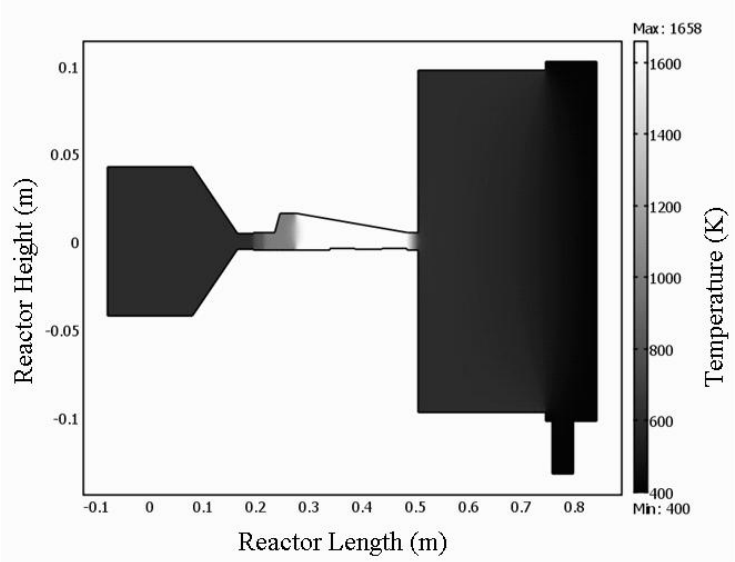

(b)

Figure 2.8 Gas temperature profile across the CVD reactor configured for (a) Geometry I and (b) Geometry II. H_2 flow = 30,000 sccm, v_{ave}=0.0173m/s and P=13.3 kPa (100 Torr).

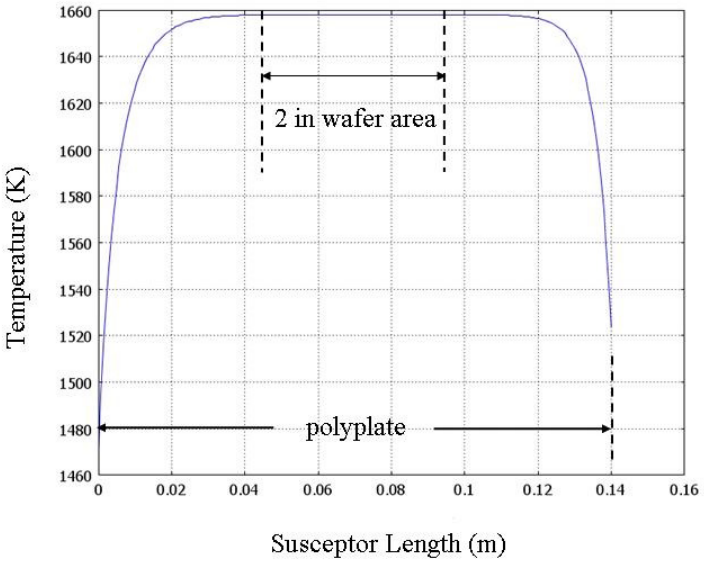

(a)

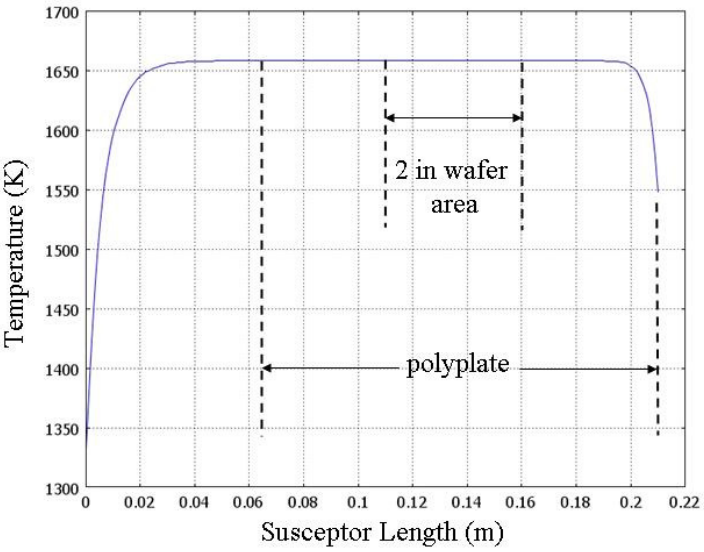

(b)

Figure 2.9 Gas temperature variation along the CVD reactor for (a) Geometry I (b) Geometry II. Note that the gas temperature remained constant at the 50 mm wafer area.

tests on the polyplate, it can be observed that for both geometries the simulation predicted that the gas surrounding the sample, if placed in the 50 mm diameter wafer area, will be at the constant temperature of 1659K (1386°C). This temperature is only one unit higher than the experimentally measured temperature of 1658K (1385°C) for the no HCl and HCl growth processes process (see Chapter 3).

The simulation is not in accordance with the obtained experimental results that a temperature gradient was observed to be present along the 50 mm wafer area. Therefore, a more detailed simulation in which radio frequency induction, material properties, and heat losses by radiation are taken in to consideration may offer a better prediction of the temperature profile in the system (see Chapter 5).

Similarly, the gas velocity profile was computed for both reactor geometries as shown in Figure 2.10. The velocity increased at the adaptor and susceptor area due to the compression of the gas as a result of the narrowing susceptor since the susceptor ceiling is angled. Because not all species travel at the same velocity, the shape of the velocity profile at a given cross section depends on the type of flow under consideration. It can be seen that the velocity at the susceptor area remained constant indicating that the precursor species should diffuse to the substrate surface at similar rates. For Geometry I the maximum velocity along the susceptor was predicted to increase from 0.29 m/s to 0.39 m/s (Figure 2.10(a)). For Geometry II the maximum velocity increased from approximately 0.14 m/s to 0.32 m/s (Figure 2.10 (b)). Note that the velocities between Geometry I and Geometry II were significantly different at the inlet; this is as a result of the elongation of the susceptor which changes the angle of inclination at the top portion of the susceptor and thus the cross-sectional area throught its length.

At these particular velocities the Re number is less than 2100, therefore the flow can be considered to be laminar. As a consequence the velocity profile along the reactor's cross-section should be parabolic in shape as shown in Figure 2.11.

Finally, since the flow at the susceptor was determined to be laminar it is assumed that the fluid will flow in parallel lines. This was verified by constructing streamline plots of the velocity profile as shown in Figure 2.12a-b. It could be observed that this was indeed the case along the entire flow path for both configurations. However minor

disruptions to the pattern are present for Geometry I possibly due to the higher velocity compared to Geometry II. These disruptions may cause some back stream issues possibly leading to the introduction of particulates into the epitaxial layer.

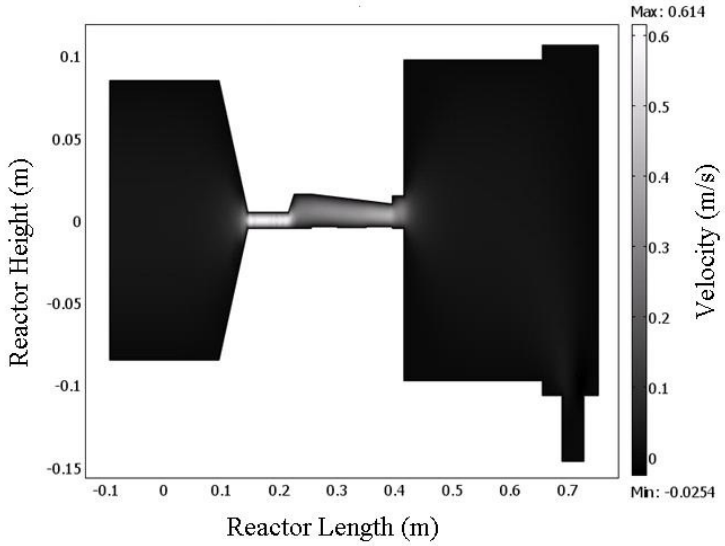

(a)

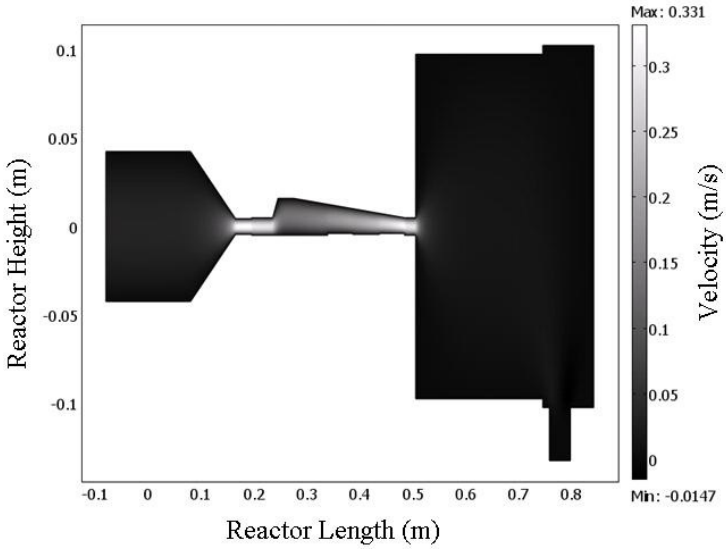

(b)

Figure 2.10 Gas velocity profile across the CVD reactor configured for (a) Geometry I and (b) Geometry II. H_2 flow of 30,000 sccm., v_{ave}=0.0173m/s and P=13.3 kPa (100 Torr).

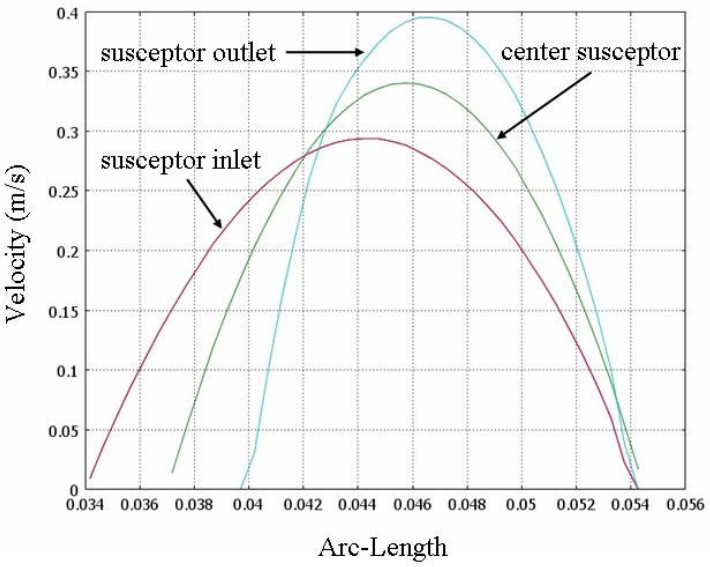

(a)

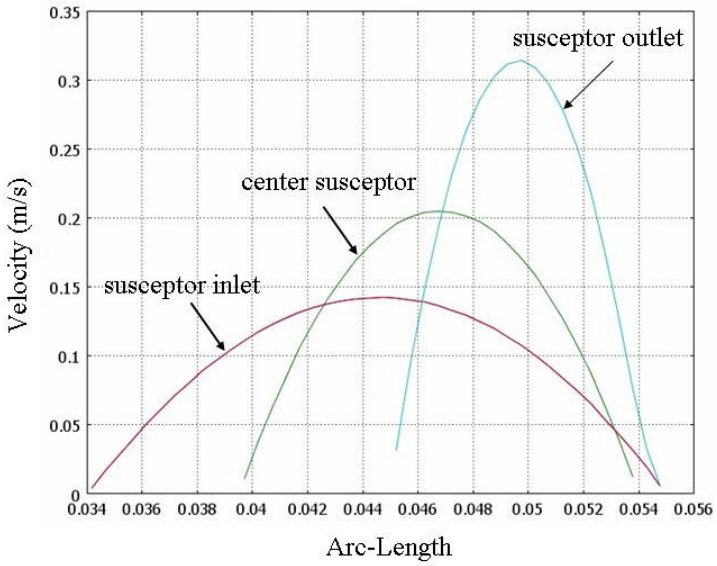

(b)

Figure 2.11 Parabolic velocity fields for (a) Geometry I and (b) Geometry II at susceptor's inlet, center and outlet.

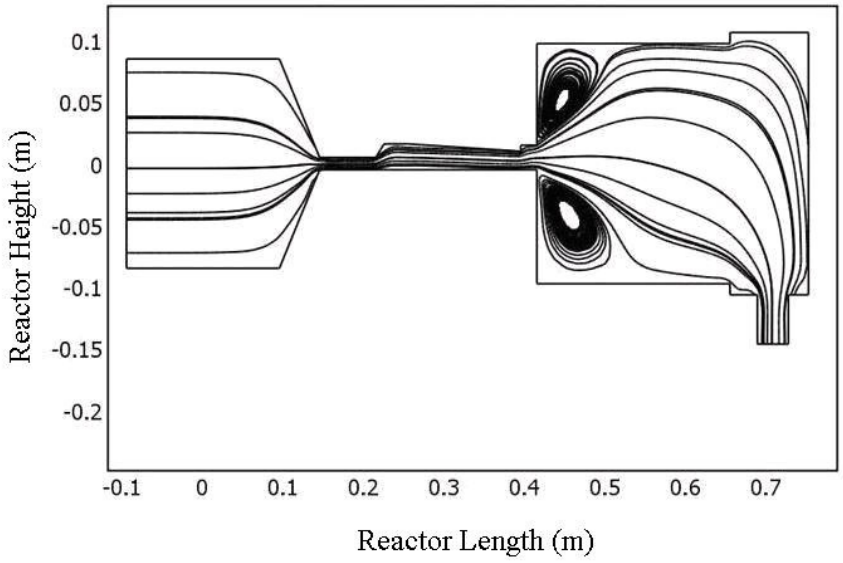

(a)

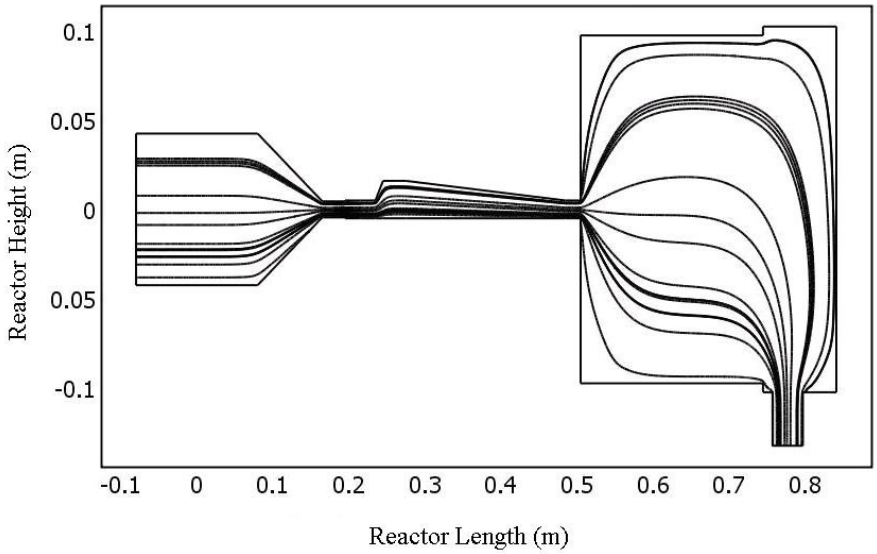

(b)

Figure 2.12 Streamline plot of the velocity profile illustrating fluid is flowing in parallel lines, thus confirming the flow is of laminar nature (a) Geometry I and (b) Geometry II.

Unfortunately, a final numerical solution for the species concentration profile along the reactor has not been established in this work due to problems with the COMSOL platform (see Chapter 5).

2.3 Summary

As a result of the work performed in this study the following simulations are now possible: (1) a thermodynamic analysis of the product composition under equilibrium conditions, and (2) computerized fluid dynamic (CFD) calculations which provide information regarding the velocity and temperature profiles along the CVD reator. It was first determined in this work that thermodynamically there appears not to be any difference in the equilibrium composition mixture between adding HCl or using chlorocarbons or chlorosilane species as the growth precursors. Simulation results were presented for the SiH_4-C_3H_8-HCl-H_2 precursor system. The major species present in the equilibrium composition mixture were CH_4, CH_3^-, C_2H_2, and C_2H_4 as carbon-containing species and SiH, Si, and SiH_2 as silicon-containing species. It was noted that the presence of HCl in the gas mixture does not significantly affect the carbon containing species. However, it was observed that chloride species preferentially bond to silicon suggesting that HCl exhibits a different reaction mechanism mainly affecting the Si containing reactions.

The predicted reactor temperature profile showed that the area where deposition occurs was within the experimentally measured temperature of 1385ºC for both reactor geometries used in this work. However, the simulation failed to show temperature gradients at the susceptor area as observed experimentally. The velocity profile obtained for both reactor geometries showed that the reactor was operating under desired laminar flow. However, the streamline plot for Geometry I showed flow disruptions at the susceptor outlet that may lead to species back stream thus possibly affecting the deposited film properties and growth rate.

Chapter 3: High Temperature 3C-SiC Heteroepitaxial Growth

3.1 Overview

The objective of this research was to increase 3C-SiC deposition rates by adding a chloride additive to the C_3H_8-SiH_4-H_2 precursor chemistry. A thermodynamic equilibrium study performed on this system (section 2.2.2.3) revealed, for the first time, that there appears not to be any significant difference on the most dominant species present in the equilibrium composition mixture between adding HCl or using chlorocarbons or chlorosilane species as growth precursors. It was predicted that HCl promotes the enhancement of 3C-SiC growth by allowing higher Si mole fractions via homogeneous nucleation reduction and formation of additional Si-containing species. Therefore, the main focus of this work will be on the addition of HCl to the CVD precursor system. Indeed, other approaches to increase deposition rates can be achieved by manipulating the CVD process parameters, i.e. temperature, pressure, and input gas composition. This approach was also explored and results are presented.

As such, the development of a 3C-SiC process via HCl additive to the C_3H_8-SiH_4-H_2 chemistry is described in this chapter. This deposition process was developed in several stages. First, a repeatable 3C-SiC process without HCl additive (i.e. baseline process) was established. Second, once this process was found to be repeatable, it was then used as the starting point for HCl additive process development. During these experiments HCl was added to the standard chemistry at the growth stage. Third, the HCl additive process was optimized to yield the optimum deposition rate and film quality. Finally, the optimized 3C-SiC deposition process was applied on 50 mm diameter Si (001) substrates. Higher area substrates allowed for the assessment of epitaxial layer uniformity and film properties.

The deposition experiments were carried out using the USF hot-wall CVD reactor MF1 described in section 2.2.1. The process schedules developed in this work consisted of a two stage carbonization and growth process as described in section 1.4. Two different reactor geometries were used to conduct the deposition experiments in this work and for simplicity they will be referred as Geometry I and Geometry II as explained in section 2.2.1. Therefore, distinction among them will be made when describing the different processes developed.

Ultra high purity hydrogen, purified via a palladium diffusion cell, served as the carrier gas during the deposition process. The carbon and silicon precursors were provided by C_3H_8 (100%) and SiH_4 (100%), respectively. Finally, 100 % HCl was used in the HCl additive experiments. Planar n-type Si (001) samples diced into 8 mm x 10 mm die were used in this study. The substrates were cleaned using an RCA cleaning procedure preceding deposition. A 30 second immersion into a buffered hydrogen fluoride etch (HF, 50:1) was performed before loading the sample to the reactor.

The resulting epitaxial layers were characterized to monitor the deposition process and results will be presented. Nomarski optical microscopy and secondary electron microscopy (SEM) were used to qualitatively analyze the film surface morphology after growth. SEM and Fourier transform infrared (FTIR) Reflectance were used for film thickness determination. Atomic force microscopy (AFM) was used to qualitatively assess surface morphology. X-ray diffraction (XRD) provided information of the crystal quality and X-ray photoelectron spectroscopy (XPS) was used to evaluate the chemical composition of the surface and near surface regions.

3.2 3C-SiC without HCl additive process development using Geometry I

3.2.1 Carbonization stage

The carbonization stage is crucial during the 3C-SiC hetero-epitaxy since it is believed that the formation of this initial buffer layer influences the crystallinity of the SiC crystal grown due to a reduced effect in the large lattice mismatch at the SiC/Si interface.[23,24] During the carbonization process, carbon originating from the thermal

cracking of C_3H_8 reacts with the silicon surface; as a result SiC nucleates on the substrate forming a film that is a few nanometers thick. The main problems to be avoided during the buffer layer deposition are the formation of voids, etch pits and hillocks. These defects are, for the most part, the result of insufficient carbon flux in the gas stream. At low C_3H_8 mole fractions there is not enough carbon to react with the silicon surface; as a result , the vertical diffusion of silicon is favored as the temperature is increased creating voids at the buffer layer/substrate interface.[86] In addition, low C_3H_8 mole fractions may also promote the formation of etch pits at the substrate due to a preferential etching rate process rather than the desired deposition. Finally, protrusions that are formed due to hillock defects or surface particles may also be present in the carbonized layers. The presence of these defects in the carbonized layers has been attributed to the agglomeration of silicon at the surface due to vertical diffusion. [86]

A 3C-SiC growth process developed by Dr. R. L. Myers in a cold-wall reactor as part as her thesis work performed in our laboratory was used as the starting point for the process development in this study.[57] Although this process provided a starting point, successive study of the process parameters was carried out to obtain the optimum conditions for the hot-wall system. The process temperature, pressure, H_2 and C_3H_8 flows and time were selected as the main controllable parameters influencing the carbonization stage. C/H_2 ratios from 1.5×10^{-4} to 48.0×10^{-4} were explored by varying the process parameters within the ranges listed in Table 3.1. Each parameter was varied one at a time to study its effect on the overall growth process.

The optimum carbonization process developed in this work is shown in Figure 3.1. A thermal ramp was performed to raise the sample temperature from approximately 300°C to 1170°C in the presence of a gas stream composed of H_2 and C_3H_8. The gas stream total flow was 10,006 sccm which had a C_3H_8 molar fraction of 6.0×10^{-4}. Finally the sample temperature was held at 1170°C for two minutes. After this procedure was completed, the sample was cooled under Ar flow.

Compositional surface characterization of a carbonized layer was determined though peak area analysis using XPS. Prior to the measurements the samples were submerged for 30 seconds in an HF solution (50:1) for native oxide removal. XPS

Table 3.1 Summary of parameter ranges considered during the carbonization stage development.

Process Parameter	Range	Units	Molar Fraction
Temperature	1050-1200	ºC	---
Pressure	150-760	Torr	---
H_2 flow	5-20	sLm*	0.99
C_3H_8 flow	1-8	sccm**	0.49×10^{-4} - 16×10^{-4}
time	2-5	minutes	---

* standard liters per minute
** standard centimeter cube per minute

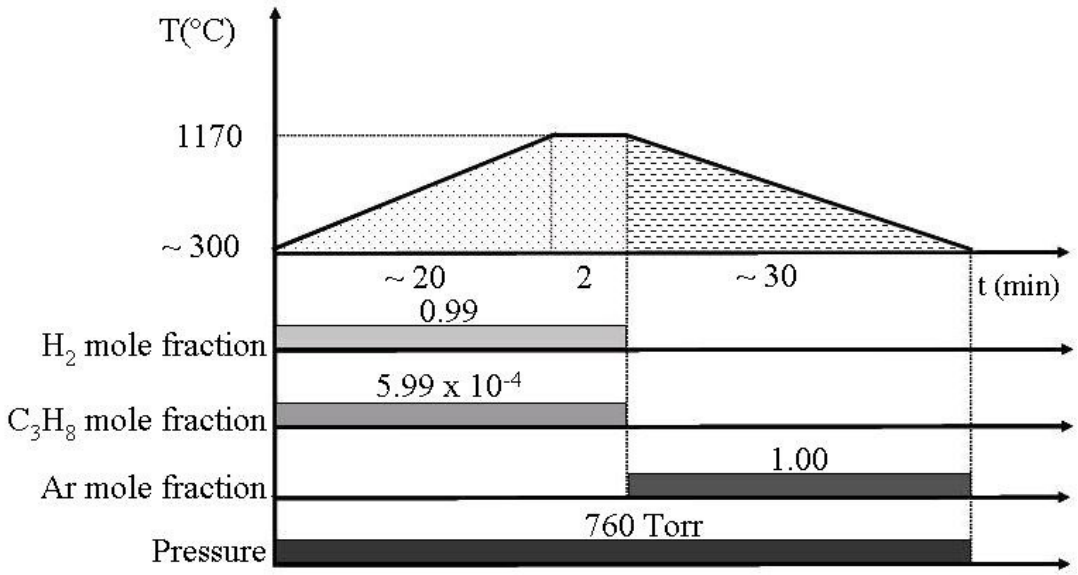

Figure 3.1 Carbonization process schedule developed for Geometry I. T=1170ºC, P=760 Torr and a total gas flow (H_2 and C_3H_8) of 10,006 sccm. A C_3H_8 molar fraction of 6.0×10^{-4} yielded the optimum buffer layer morphology.

measurements revealed that carbon, silicon and oxygen (O), were the elements present at the buffer layer surface at atomic concentrations of 42.1%, 35.0% and 22.8%, respectively.

The high resolution XPS spectra of the C1s and Si2p are shown in Figure 3.2(a) and Figure 3.2(b), respectively. Each high resolution spectra was deconvoluted by fitting

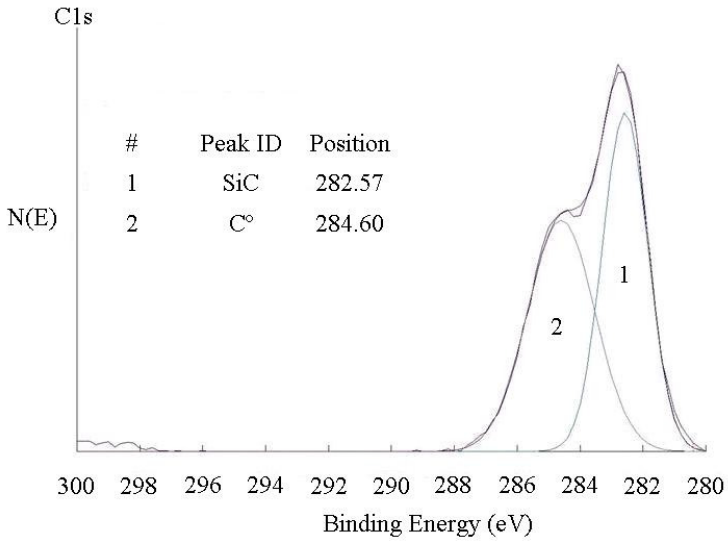

(a)

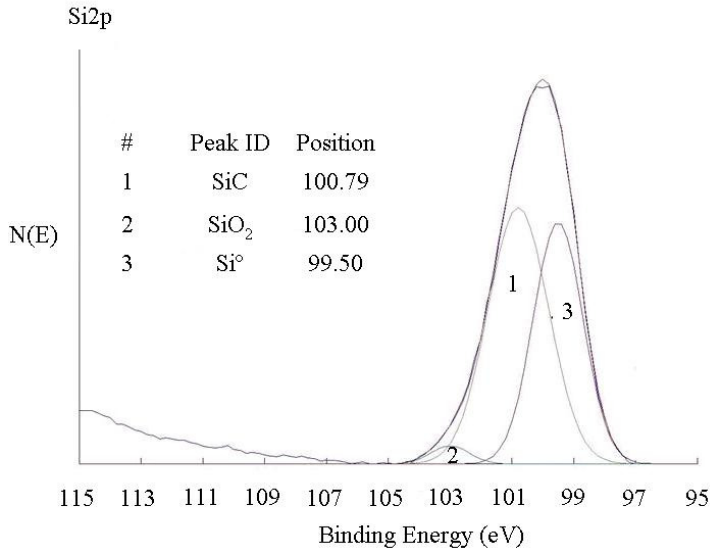

(b)

Figure 3.2 XPS high resolution spectra of (a) C1S and (b) Si2p peaks for a representative carbonized layer. Each high resolution spectra was deconvoluted by fitting Gaussian curves.

theoretical Gaussian curves. The C1s spectra displayed carbidic- (49.7%) and graphitic-bound (50.3%) carbon at the surface and near surface regions. Graphitization of SiC surfaces is known to occur due to exposure with air or due to a preferential evaporation of silicon at elevated temperatures.[87] The Si2p spectra suggested the presence of metallic silicon (42.5%), carbidic-bound silicon (55.0%) and silicon bound to oxygen as silicon dioxide SiO_2 (2.5%). The metallic silicon observed could be coming from the silicon substrate. Finally the O1s (not shown) revealed that the oxygen present was bound to silicon as SiO_2.

3.2.2 Second thermal ramp

Since 3C-SiC growth is typically performed at temperatures higher than 1300ºC, a second thermal ramp was conducted to transition from the carbonization stage to the growth stage. The second thermal ramp is crucial since the resulting layer will provide the final surface template used during the growth step. Initial experimentation was performed by ramping to growth temperature (10ºC/min) using a gas mixture composed of H_2 and C_3H_8 at C/H_2 ratios from 6.0×10^{-4} to 10.0×10^{-4}. However pits and rough surfaces where observed via AFM in the resulting layers. The presence of these defects may be due to insufficient silicon to react with the carbon precursor resulting in preferential etching process. Therefore SiH_4 was introduced during this process. Other challenges presented were the formation of hillock defects and the sporadic observations of particles. In this case hillocks and/or particles at the surface could be the result of carbon or silicon precipitates due to elevated C_3H_8 or SiH_4 mole fractions. To evaluate this, a study of the process parameters was carried out to determine optimal conditions. The process parameters and ranges considered are listed Table 3.2. This study was also performed by varying one factor at a time.

Figure 3.3 displays the process schedule developed for the second thermal ramp including the carbonization step. SiH_4 was introduced into the gas stream and the temperature was increased from 1170ºC to 1385ºC after performing the carbonization stage. The total gas flow (H_2, C_3H_8 and SiH_4) was 10,010 sccm. The C_3H_8 and SiH_4 molar fractions were 6.0×10^{-4} and 4.0×10^{-4}, respectively. Once the temperature reached

1385ºC the process was stopped, the sample was cooled under Ar flow and the thin layers were analyzed.

Table 3.2 Summary of parameters ranges considered during the second thermal ramp development.

Process Parameter	Range	Units	Molar Fraction
Temperature	1170-1350	ºC	---
Pressure	150-760	Torr	---
H_2 flow	10-20	sLm	.99
C_3H_8 flow	1-8	sccm	0.5×10^{-4} -8×10^{-4}
SiH_4 flow	0-10	sccm	0- 10×10^{-4}

* standard liters per minute
** standard centimeter cube per minute

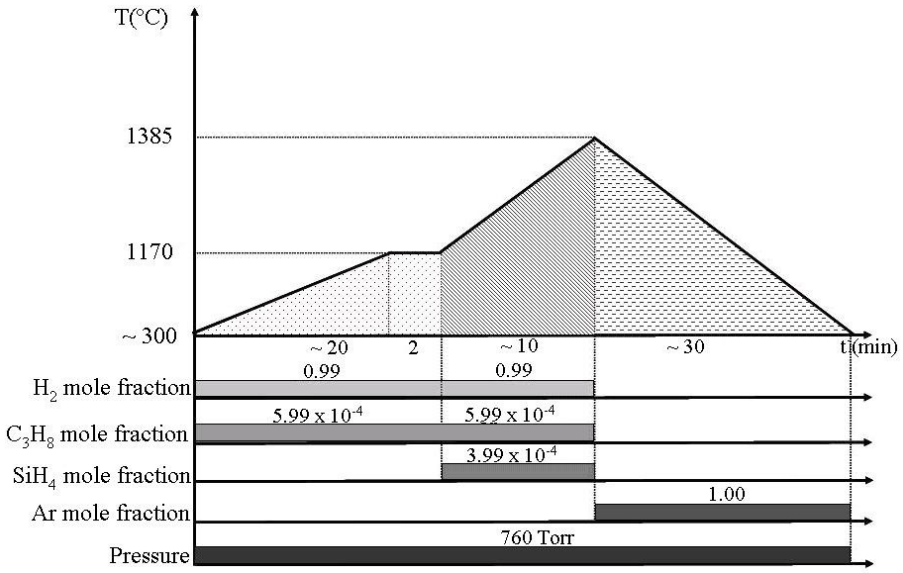

Figure 3.3 Second thermal ramp process schedule developed for Geometry I, including the carbonization stage. Total gas flow (H_2, C_3H_8 and SiH_4) was 10,010 sccm. C_3H_8 and SiH_4 molar fractions were 6.0×10^{-4} and 4.0×10^{-4}, respectively.

A plan-view SEM image of a representative layer grown following the process schedule is illustrated in Figure 3.4. The surface lacked hillock defects indicating the

process parameters were indeed approaching optimum ranges (Figure 3.4(a)). A cross-sectional view of the same layer is shown in Figure 3.4(b). No voids were observed at the interface. The estimated layer thickness via SEM was approximately 147 nm.

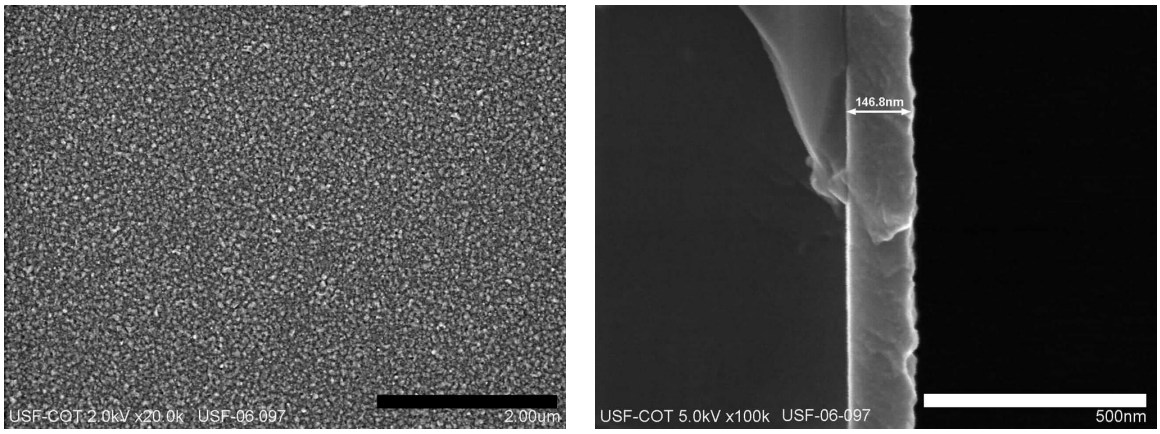

(a) (b)

Figure 3.4 (a) Plan view SEM image of a representative layer after carbonization and second thermal ramp at best process conditions (no etch pits or hillock defects). (b) Cross-section view of the same layer indicated no voids at the interface. The estimated layer thickness was 147 nm. Image courtesy of D. Edwards, USF COT.

The film topology was analyzed via AFM. Figure 3.5(a-b) shows the growth progression of the already coalesced islands formed in the carbonization process due to the low growth rate deposition process performed in the second ramp. As can be seen, the layer is characterized by large features which were homogenously oriented (Figure 3.1). This is expected since the carbonized layer previously formed provided a better template for the second thermal ramp. The features were observed to be triangular in shape with a measured surface roughness of 3.9 nm RMS.

Surface chemical composition analysis by XPS of a resulting layer after carbonization and the second thermal ramp was performed. The samples were also cleaned prior to the analysis with an HF solution as explained earlier. As with the carbonized layer, C, Si and O were determined to be the species present at the surface and near surface regions. The atomic concentrations were measured to be 52.0%, 31.5% and 16.5%, respectively.

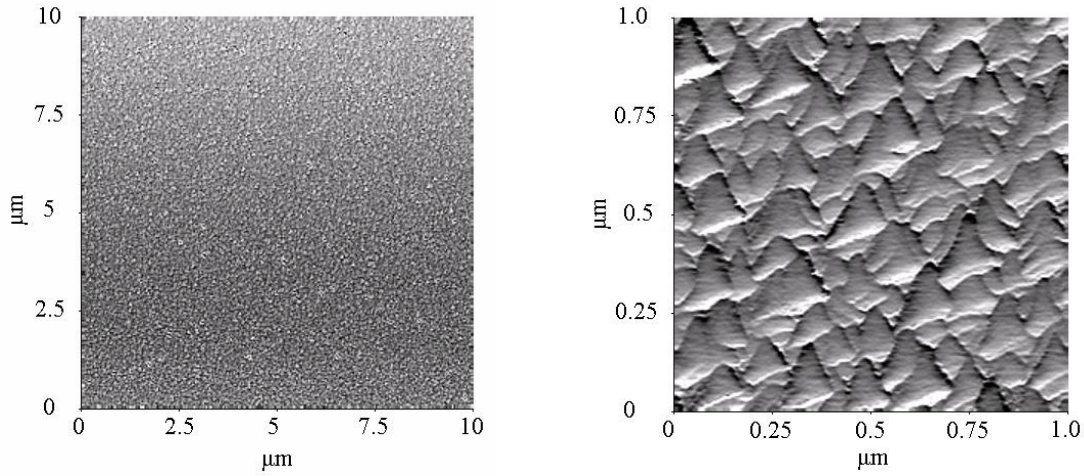

(a) (b)

Figure 3.5 AFM micrographs of a representative layer after the carbonization and second thermal ramp processes. (a) Note homogeneously oriented features. (b) Closer inspection revealed features were triangular shaped. Measured surface roughness was 3.9 nm RMS. Sample ID USF-06-097.

The high resolution spectra for the C1s peak shown in Figure 3.6(a) revealed that 55% of the carbon present at the surface was due to C bound as SiC and the remaining 45% was due to adventitious carbon. Similarly the high resolution Si2p peak showed that only silicon bound as SiC (96.9%) and SiO_2 (3.1%) were present (Figure 3.6(b)). Each high resolution spectra was also deconvoluted by fitting theoretical Gaussian curves. Note that contrary to the XPS analysis performed for the carbonized layer (section 3.2.1) metallic silicon was not found to be present at the surface. This was due to an increased layer thickness as a result of the low-rate deposition carried out during the second thermal ramp which yielded a layer approximately 147 nm thick. Therefore X-ray penetration to the substrate was not an issue.

3.2.3 Growth stage

With the carbonization and second thermal ramp process developed and optimized, the 3C-SiC growth step could proceed. Initial growth step conditions were also based on the initial 3C-SiC growth process developed by Dr. R. Myers.[57] However, polycrystalline films were obtained when similar process conditions were implemented.

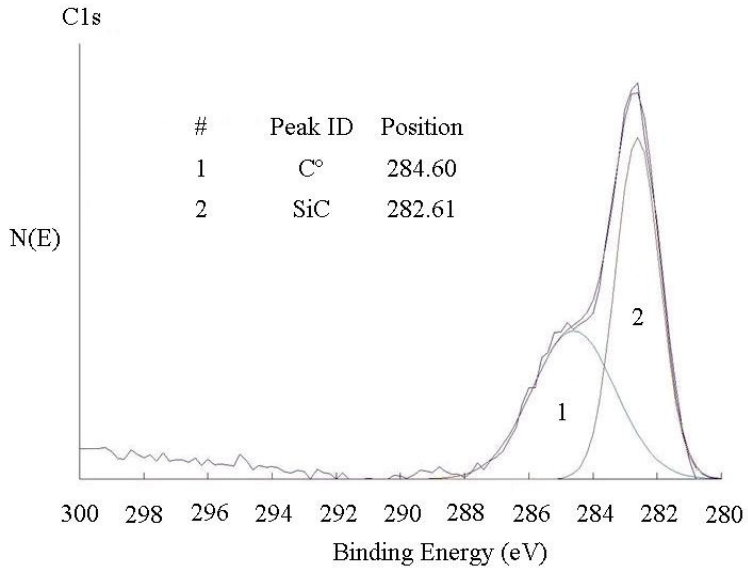

(a)

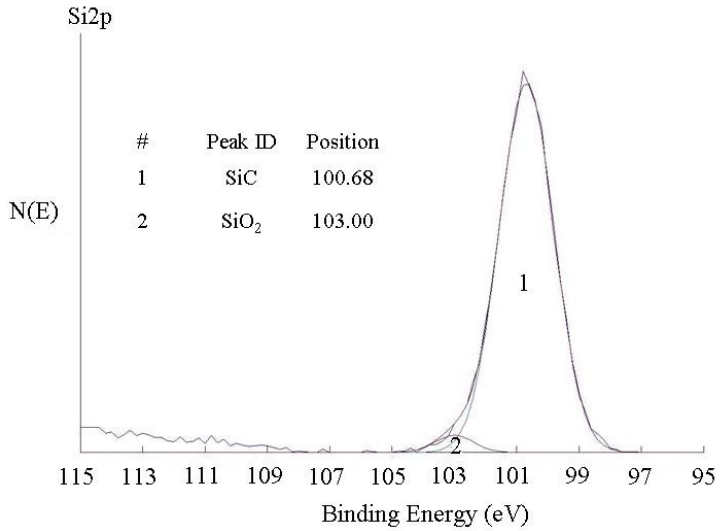

(b)

Figure 3.6 XPS high resolution spectra of (a) C1S and (b) Si2p peaks of a representative layer after the carbonization and second thermal ramp processes. Each high resolution spectra was deconvoluted by fitting Gaussian curves.

Therefore multiple experiments were conducted in which the process parameters of temperature, pressure and precursor mole fractions were varied one at a time. As a result, a preliminary growth step process which yielded single crystalline 3C-SiC films grown at a rate of 4 μm/h was obtained. The preliminary growth step was conducted at a process

temperature and pressure of 1375ºC and 200 Torr. The total input flow was set to 30,014 sccm which had C_3H_8 and SiH_4 mole fractions of 2.0 x 10^{-4} and 2.6 x 10^{-4}, respectively.

Once this preliminary process was obtained, optimization of the process parameters was performed. First the process temperature was varied within the temperature range of 1330ºC – 1395ºC. It was observed that at temperatures lower than and equal to 1350ºC, non-specular layers were obtained suggesting that the saturation point had been reached. The best surface morphology as assessed by AFM and SEM techniques was found to occur within the temperature window of 1375ºC-1385ºC; the temperature of 1385ºC was chosen to be kept constant for the continued experiments. Pressure variation experiments over the range of 75 Torr – 400 Torr revealed an improvement in surface morphology at decreased pressures. Despite that better surfaces were obtained at decreased pressures, 100 Torr was chosen as the most favorable pressure since that was the lowest value that the CVD system could sustain efficiently.

Having established that the most favorable surface morphology for our process had been obtained at 1385ºC and 100 Torr, the focus was shifted to determine the optimum process Si/C ratio at these conditions. This was accomplished by varying the SiH_4 mole fraction keeping the process temperature, pressure and H_2 and C_3H_8 mole fractions constant during the epitaxial deposition process. From these experiments it was found that a SiH_4 mole fraction of 4.3 x 10^{-4} provided the best surface morphology as assessed by SEM and AFM.

Details of the final growth process schedule for the 3C-SiC process without HCl additive are illustrated in Figure 3.7. The carbonization and second ramp process described in Figure 3.3 were performed prior to conduct the growth stage. Once the growth temperature of 1385ºC was reached the process pressure was lowered to 100 Torr and the total gas flow (H_2, C_3H_8 and SiH_4) was set to 30,019 sccm. The C_3H_8 and SiH_4 molar fractions at the growth stage were 2.0 x 10^{-4} and 4.3 x 10^{-4}, respectively. At these process conditions the process Si/C ratio was 0.72 and the process growth rate increased to 8.6 μm/h.

Once the optimum process conditions were determined experiments were conducted in order to obtain the maximum process growth rate. This was accomplished

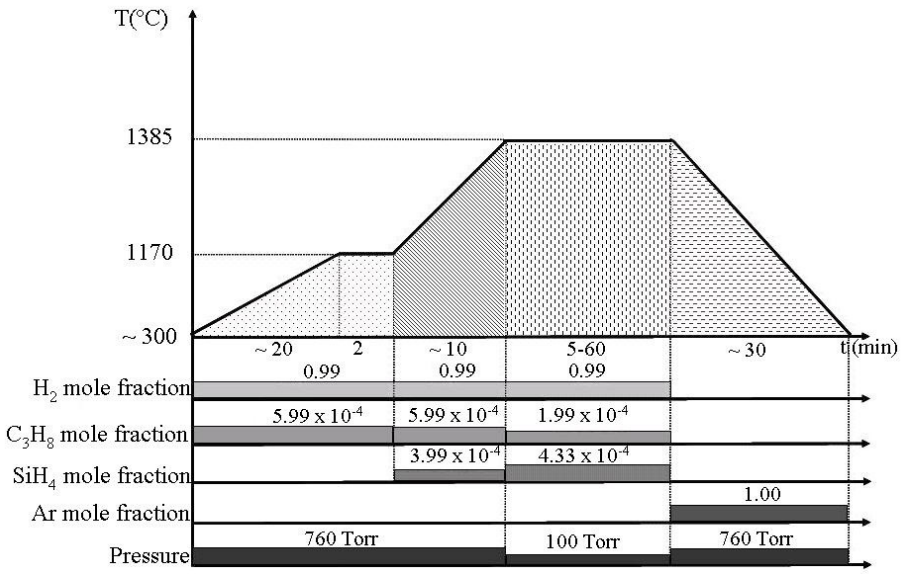

Figure 3.7 3C-SiC growth process schedule using C_3H_8-SiH_4-H_2 chemistry developed for Geometry I. Mole fractions presented for 8.6 µm/h process. At the growth stage the total input gas flow (H_2, C_3H_8 and SiH_4) was set to 30,019 sccm with C_3H_8 and SiH_4 molar fractions of 2.0 x 10^{-4} and 4.3 x 10^{-4}, respectively. Process Si/C=0.72

by setting the process temperature, pressure and Si/C constant while increasing the precursor mole fraction by approximately 20% after each run using the parameters shown in the process schedule illustrated in Figure 3.7. From this study it was determined that the maximum process growth rate that could be obtained leading to specular surfaces was approximately 12 µm/h; this was achieved at a total input flow of 30,022 sccm. The propane and silane mole fractions were 2.0 x 10^{-4} and 5.3 x 10^{-4}, respectively. At higher precursor mole fractions the deposited layers obtained were polycrystalline.

In conclusion, the optimization of the 3C-SiC process without HCl additive not only allowed for good film morphology but the growth rate was increased by 3 times that of the preliminary growth process. In addition, since this process was desired to be used as the starting point for the HCl additive experiments it was imperative to ensure that the process growth rate was repeatable. Therefore, the growth rate variation was studied using the ~8.6 µm/h process described above. Table 3.3 lists growth rate measurements taken for 6 different samples grown using the process schedule as explained in Figure 3.7.

Table 3.3 Summary of growth rate data for the calculation of baseline process repeatability using ~8.6 µm/h process.

Run	Growth Rate (µm/h)	Average (µm/h)	Standard Deviation (µm/h)
1	9.0	8.8	± 0.2
2	8.9		
3	8.6		
4	8.6		
5	8.4		
6	9.0		

It was determined that the average process growth rate was 8.8 µm/h. For this particular data set the standard deviation was determined to be ± 0.2 µm/h. The average ($\bar{x}$) and standard deviation (σ) values were calculated using their respective definitions from statistics.

Once the process growth rate was found to be repeatable the epitaxial layers grown using the optimized process were characterized further. Figure 3.8 shows a plan-view SEM image of a representative 3C-SiC film after performing the growth schedule depicted in Figure 3.7. The surface was specular, and clean of protrusion type defects.

Figure 3.8 Plan-view SEM image shown at a magnification of 5.0k for a representative 3C-SiC layer grown with the no HCl process at a rate of ~8.6 µm/h grown. Image courtesy of D. Edwards, USF COT.

Figure 3.9 shows a 10 µm x 10 µm AFM micrograph taken in contact mode for the same epitaxial layer. The surface topography was observed to have a more crystal-like surface due to the coalescence of the different nucleation islands. The typical anti-phase domain boundaries characteristic of 3C-SiC films are also observed. As a reference, the measured surface roughness was 1.6 nm RMS.

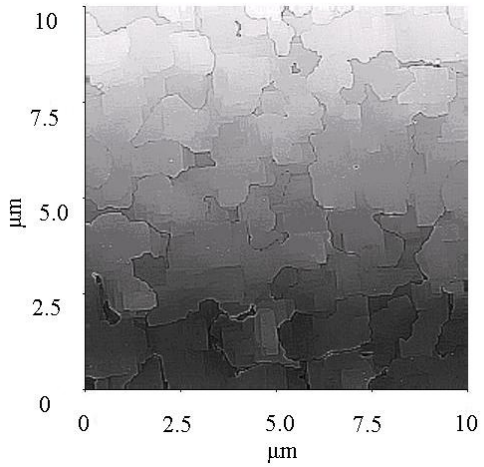

Figure 3.9 AFM micrograph (10 µm x 10 µm) taken in contact mode of a representative 3C-SiC layer grown at a rate of 8.6 µm/h. The surface roughness was measured to be 1.6nm RMS.

The quality of the epitaxial layer was also assessed via XRD. The powder diffraction technique was applied first in order to observe which reflections were detected in the crystal under study (Figure 3.10). The data revealed that the most intense peak was from the 3C-SiC (002). The presence of the Si (002) and 3C-SiC (004) diffraction peaks were also noted, however at much lower intensities.

A XRD rocking curve was generated for the 3C-SiC (002) diffraction peak which revealed a full width at half maximum (FWHM) of 500 arcsec as seen in Figure 3.11. This value was found to be better and/or comparable to values reported elsewhere and is indicative of a single crystal quality material.[45] It should be noted that the (004) plane reflection indicates epitaxial film growth since this is part of the (002) family of crystal planes.

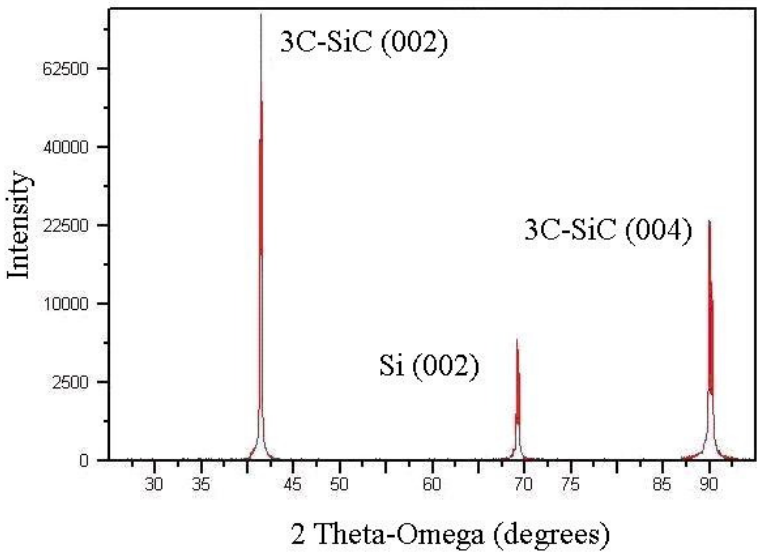

Figure 3.10 XRD powder diffraction of a 3.3 μm thick 3C-SiC epitaxial layer. The diffraction peaks for Si <002>, 3C-SiC <004> and 3C-SiC <002> were observed. XRD performed by Dr. Y. Shishkin, USF SiC group.

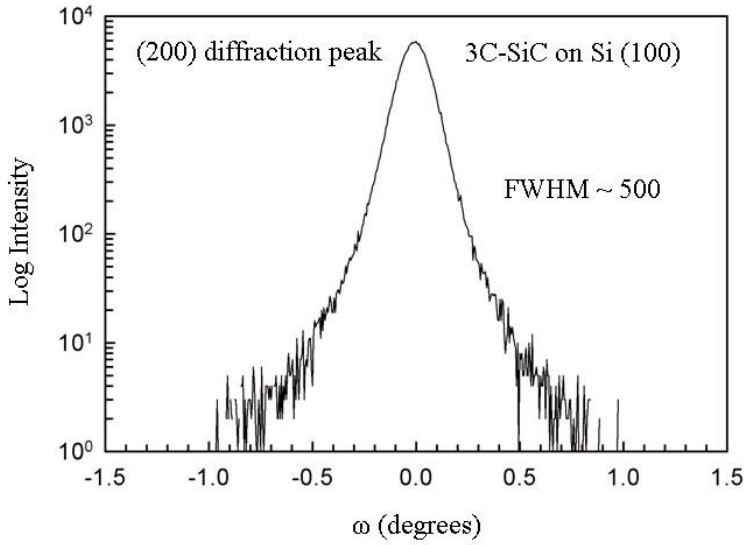

Figure 3.11 XRD rocking curve of a 3.3 μm thick 3C-SiC epitaxial layer performed at the 3C-SiC (002) diffraction peak. The measured FWHM was 500 arcsec which is indicative of a high quality single crystal layer.[45] XRD performed by Dr. Y. Shishkin, USF SiC group.

3.3 HCl additive process development using Geometry I

The 3C-SiC without HCl process development was crucial for the HCl additive experiments as it provided an optimized, repeatable and well documented baseline process. Since good quality single crystal 3C-SiC layers were obtained by performing the no HCl additive process, the addition of HCl was applied next to this process to determine if the process growth rate could be increased further and/or the epitaxial layer quality could be improved. In this section the results of the HCl additive study are presented. The HCl addition was applied first to the second thermal ramp and finally to the growth stage.

3.3.1 HCl addition to second thermal ramp

The HCl additive experiments first focused on the second thermal ramp process illustrated in Figure 3.3 with the objective being to improve the surface morphology of the layer grown, thus providing a better surface template. In this work HCl was added at mole fractions ranging from 0.5 x 10^{-4} to 2.0 x 10^{-4} after the carbonization process was completed. The epitaxial layers were analyzed via optical microscopy, SEM and AFM where the formation of etch pits and rough surfaces were noted. The presence of these defects was mainly attributed to HCl etching at the surface. Therefore the experimental results supported that the addition of HCl to the second thermal ramp was not beneficial for the process. As a result no changes were made to the second thermal ramp process developed during the 3C-SiC process without HCl.

3.3.2 HCl addition to the growth stage

HCl additive experiments performed next focused on the growth stage. During this series of experiments, HCl at mole fractions ranging from 0.2 x 10^{-4} to 2.7 x 10^{-4} were added to the 3C-SiC without HCl process resulting in deposition rates of ~8.6 μm/h (Figure 3.3). It was observed that the epitaxial growth rate and surface morphology remained unchanged for HCl mole fractions up to 1.0 x 10^{-4} after which the surface morphology became rough and non-specular due to excessive HCl in the gas stream

causing surface etching. It was concluded from these experiments that the maximum HCl mole fraction that the process could withstand without compromising growth rate or surface morphology was 0.7 x 10^{-4}. At these conditions the process Si/Cl ratio was determined to be 6.5. Similarly, experiments were conducted by varying the SiH_4 mole fraction while keeping the other process parameters constant to verify that the Si/C ratio used was the most beneficial for the HCl process. Finally, AFM measurements supported that a Si/C ratio of 0.9 provided a slight improvement in the surface morphology compared to that of the no HCl additive process.

The final process schedule developed for the HCl additive experiments is illustrated in Figure 3.12. When comparing the no HCl additive process schedule to the HCl additive process schedule it can be noted that the only differences among them are the addition of HCl (Si/Cl=6.5) into the gas chemistry at the growth stage as well as an increased Si/C ratio from 0.7 to 0.9 for the HCl additive process.

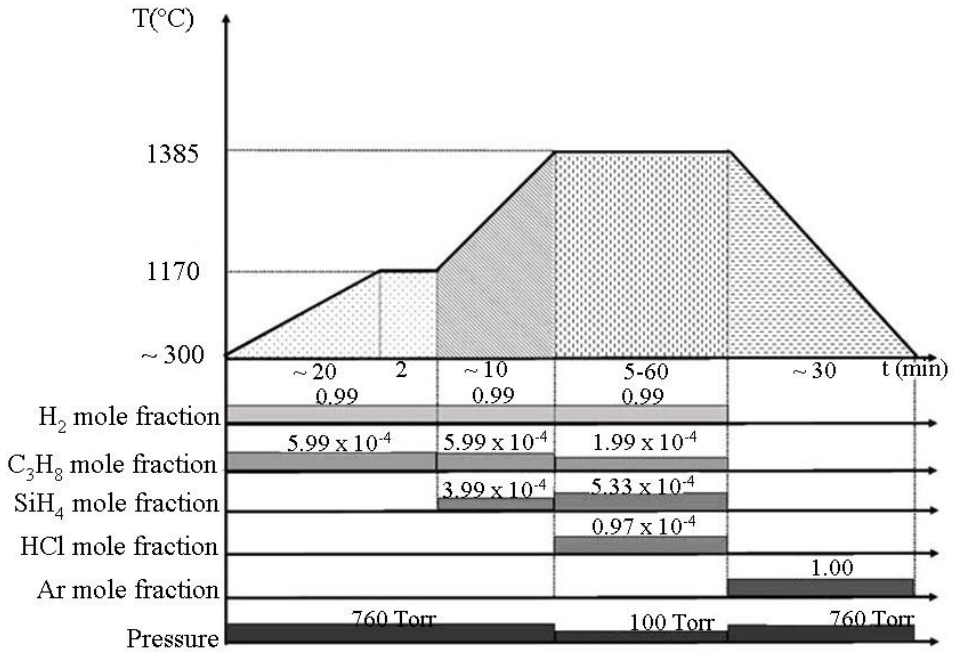

Figure 3.12 3C-SiC HCl additive growth process schedule developed for Geometry I. Mole fractions presented for ~12 μm/h process. At the growth stage the total input gas flow (H_2, C_3H_8 and SiH_4) was set to 30,025 sccm. Process Si/C=0.9 and Si/Cl=6.5. flow (H_2, C_3H_8 and SiH_4) was set to 30,025 sccm. Process Si/C=0.9 and Si/Cl=6.5.

3.3.3 CVD reactor characterization

From the work previously discussed it was discovered that just adding HCl to the process did not result in a growth rate increase or a dramatical improvement of the epitaxial layer surface morphology or quality. Therefore, continued study was conducted in order to determine which advantages to the process the HCl addition will provide. This was accomplished by performing reactor characterization via process parameters dependences as discussed next.

3.3.3.1 Growth rate as a function of silane mole fraction

In section 3.2.3 it was discussed that increased precursor mole fractions were not possible, thus the growth rate for the no HCl additive process was limited to 12 μm/h. Therefore a similar experimental series was implemented for the HCl additive process in order to determine if HCl would allow for increased precursor mole fractions resulting in increased growth rate while maintaining crystal morphology/quality. As a reference, the process pressure and temperature used in this study were 1385ºC and 100 Torr, respectively. In addition, the process Si/C and Si/Cl ratios were kept constant at 0.9 and 6.5, respectively; which were identified to be the optimum in section 3.3.2.

Figure 3.13 illustrates the experimental growth rate dependence on SiH_4 mole fraction. The total input flow varied from 30,025 sccm to 30,069 sccm. The SiH_4 mole fractions ranged from 0.53 $x10^{-3}$ to 1.49 $x10^{-3}$ whereas C_3H_8 mole fractions varied from 0.19 x 10^{-3} to 0.55 x 10^{-4}. Finally the HCl mole fraction on the gas stream fluctuated within the 0.09 x 10^{-3} to 0.29 x 10^{-3} range. As can be observed, the growth rate followed a linear relationship increasing from ~8.6 μm/h to 38 μm/h. These values are the highest growth rates reported in the literature for the 3C-SiC heteroepitaxy via horizontal, hot-wall CVD to date.

Specular surface morphology was obtained for every film grown in this set of experiments. Inspection of the 3C-SiC epitaxial layers suggested no void formation at the layer/substrate interface. Further inspection via SEM showed the sporadic growth of protrusions defect clusters as shown in Figure 3.14. It was observed that the size of these defects was more prominent at higher silane mole fractions and as the epitaxial layer

thickness increased. They may occur as a result of homogeneous nucleation in the gas phase, which is known to occur at high Si mole fractions when the precursor mixture is approaching the saturation limit at the given process conditions.

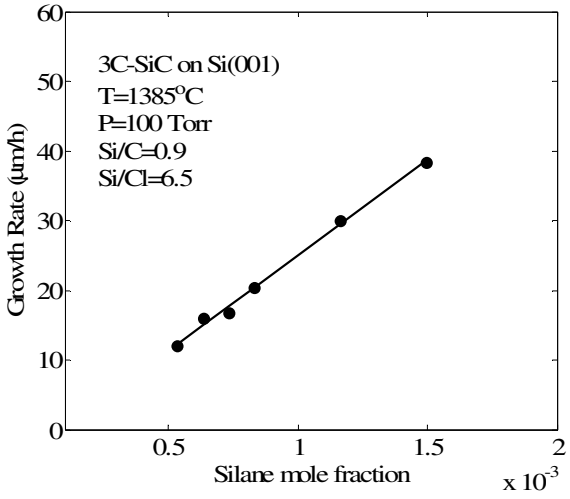

Figure 3.13 3C-SiC film growth rate vs. SiH_4 mole fraction. Growth rates from 8.6 μm/h to 38 μm/h were obtained. Experiments conducted at precursor Si/C=0.9 and Si/Cl=6.5. C/H_2 varied from 6.0 x 10^{-4} to 16.7 x 10^{-4}. Trend line to aid the eye only.

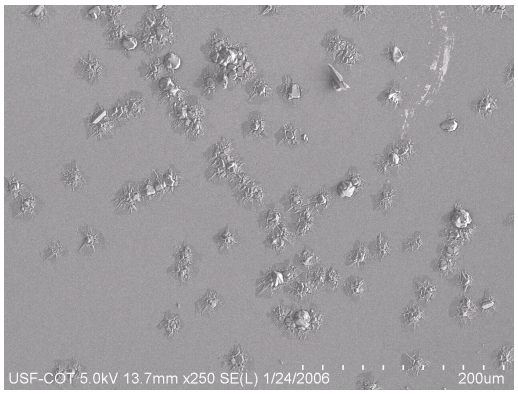

Figure 3.14 Plan-view SEM image showing protrusion defects which were observed to increase in density and size as the SiH_4 mole fraction and the epitaxial layer thickness increased. The epitaxial layer thickness is ~ 23 μm grown at a speed of 20 μm/h. Image courtesy of D. Edwards, USF COT.

3.3.3.2 Growth rate as a function of process pressure

The process pressure effect on the deposition rate and film surface morphology was also studied. Experiments were carried out using a 12 μm/h growth process. The process Si/C, Si/Cl and C/H_2 ratios were 0.9, 9.6 and 6.0 x 10^{-4}, respectively. The process pressure was varied from 75 Torr to 760 Torr, whereas the process temperature was fixed at 1385ºC. The experimental results are summarized in Figure 3.15. The deposition rate remained constant for process pressures from 75 Torr to 250 Torr, after which the rate started to decrease. Although all the films presented specular surface morphology, AFM measurements revealed the film surface roughness increased from 3.7 nm RMS to 12.0 nm RMS over the pressure range studied (75 Torr to 450 Torr) which indicated film degradation with process pressure. This behavior is in accordance to theory which establishes that as the process pressure is decreased the deposition growth rate decreases due to lower absolute precursor concentrations and due to increased gas velocity. Similarly improved deposition uniformity is expected as the pressure is decreased due to an increased value in the diffusion length of the adsorbed species on the growth surface. Based on the findings discussed above the optimum process pressure for the deposition experiments was selected to be 100 Torr. Lower pressures were not selected due to the inability of the vacuum system to maintain them.

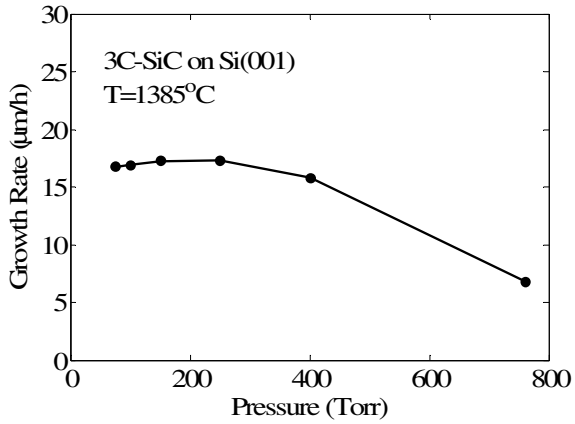

Figure 3.15 3C-SiC film growth rate vs. process pressure. Films grown at a speed of 12 μm/h with HCl additive at Si/C=0.9 and Si/Cl=6.5. Optimum film quality achieved at 100 Torr. Trend to aid eye only.

3.3.3.3 Process stability and reliability

An important aspect during CVD reactor characterization is to study if epitaxial layers grown at different deposition times lead to the same growth rate. If this could be attained then it can be ensured that the process is stable and reliable. In this study, deposition experiments were conducted using a 20 μm/h deposition process. The process pressure and temperature were set to 100 Torr and 1385ºC, respectively, and a total input gas flow of 30,038 sccm was maintained during the growth step. The C_3H_8, SiH_4 and HCl mole fractions were 8.32 x 10^{-4}, 3.10 x 10^{-4} and 1.33 x 10^{-4}, respectively. Finally growth times from 5 minutes to 60 minutes were examined. Figure 3.16 illustrates the experimental dependence of growth rate with deposition time. As can be seen, the growth rate remained fairly constant suggesting that the process will be able to sustain this growth rate at extended deposition times.

Although the growth rate could be maintained and specular films were obtained in this study, the experimental data indicated degradation of the epitaxial layer due to an increased size of protrusion type cluster defects at the surface as can be seen in the optical microscope images illustrated in Figure 3.17. Due to this behavior, additional experimentation was performed at deposition times of 75 minutes and 90 minutes to determine to what extent specular films could be obtained. It was found that the maximum growth time that could be employed in this study was 60 minutes for films grown with the HCl additive process at a rate of 20 μm/h. The deposited layers grown for 60 minutes (~ 20 μm thick) were specular. At growth times greater than 60 minutes, film defect propagation was prominent and rough (non-specular) surfaces were often obtained.

The film quality was also assessed via XRD. Figure 3.18 shows the XRD rocking curve collected on a 12 μm thick 3C-SiC film grown on the control Si (100) surface at a rate of 20 μm/h under conditions described above. The full width at half maximum (FWHM) of the (200) diffraction peak was ~360 arcseconds. This value is comparable to the that reported in literature confirming the structural integrity of the 3C-SiC films grown with this process.[45]

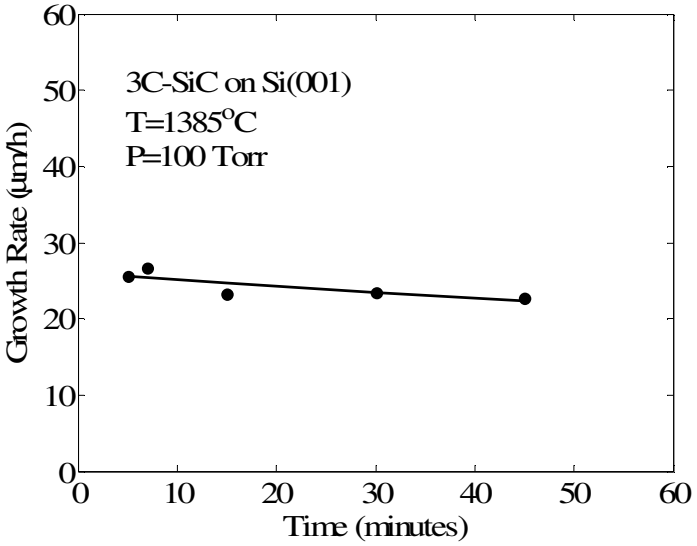

Figure 3.16 3C-SiC film growth rate vs. growth time. The films were grown at a rate of 20 μm/h. The growth times were 5, 7, 15, 30 and 45 min. Trend line drawn to aid the eye only.

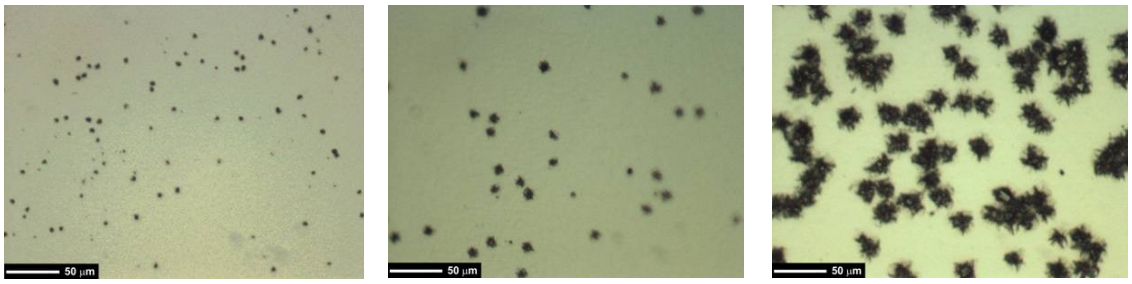

Figure 3.17 Optical microscope images at a magnification of 20X of (a) 5.8 μm, (b) 11.7 μm and (c) 23.3 μm 3C-SiC epitaxial layers showing increased size of protrusion defects at the surface as the epitaxial thickness increases.

3.4 HCl additive process optimization using Geometry I

Since growth at extended times (> 60 min. @ 20μm/h) was not possible due to surface morphology degradation, studies were conducted to investigate the growth of thicker films. The initial focus was directed toward the carbonization and second thermal ramp process. It was hypothesized that providing a higher quality buffer layer before growth would decrease the propagation of defects from the buffer layer to the epitaxial

layer thus decreasing film degradation with growth time. To this end, optimization was carried out in the actual growth step where the film degradation with time was first noticed.

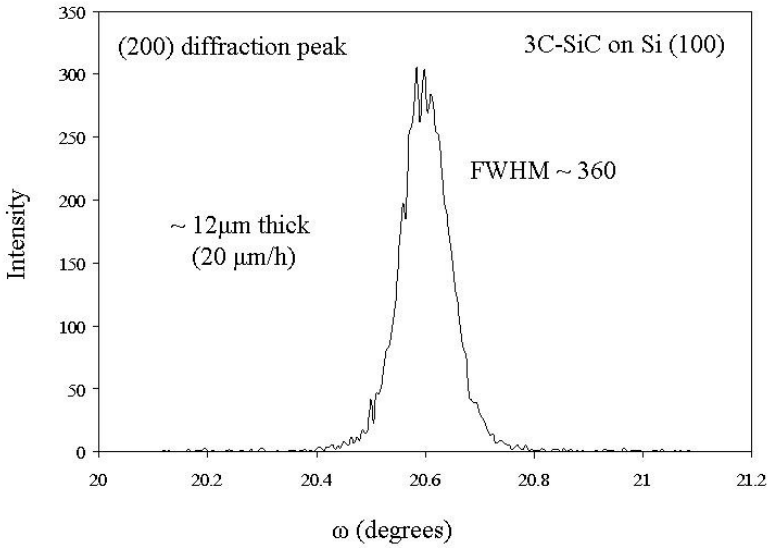

Figure 3.18 XRD rocking curve of a 3.3 µm thick 3C-SiC epitaxial layer performed at the 3C-SiC (002) diffraction peak. The measured FWHM was 500 arcsec which is indicative of a high quality single crystal layer.[45]

Before conducting the optimization procedure, samples in which the process was stopped right after the second thermal ramp were re-examined. From this analysis it was confirmed that no voids were present at the 3C-SiC/Si interface. However, more characterization of the films surfaces by AFM revealed the sporadic formation of protrusion defects several nanometers in size after the second thermal ramp was performed.

3.4.1 Optimization of the carbonization step

This optimization focused on obtaining the optimum C_3H_8 mole fraction for the carbonization process and also explored the addition of an H_2 etch step after the 2 minute carbonization stage in order to solve the protrusion defect problem. Table 3.4 summarizes

three of the numerous experiments conducted for this process optimization. Figure 3.19 (a) shows an AFM micrograph of the carbonized surface when the amount of C_3H_8 in the gas stream during the second thermal ramp was reduced from that shown in Figure 3.12. As can be seen, the surface contains numerous grains which are round in shape. Figure 3.19(b) illustrates the AFM film surface micrograph of a sample in which the same process described for Figure 3.19(a) was done after an H_2 etch step of 1 minute at 1170ºC. It can be observed that by adding the etch step, the anti-phase domains at the surface are still rounded in shape but somewhat larger than those observed without the H_2 etch step. Finally, Figure 3.19(c) shows the carbonized surface using a process including the H_2 etch step but with the same C_3H_8 mole fraction shown in Figure 3.12. Enlarged, more oriented and homogeneous cubic grains were observed.

Table 3.4 Summary of process parameters during second thermal optimization

Run #	C_3H_8 mole fraction	H_2 etch	Surface Roughness (nm RMS)	Notes
1	4.5×10^{-4}	No	12.1	Figure 3.19(a)
2	4.5×10^{-4}	Yes	5.5	Figure 3.19(b)
3	6.0×10^{-4}	Yes	6.2	Figure 3.19(c)

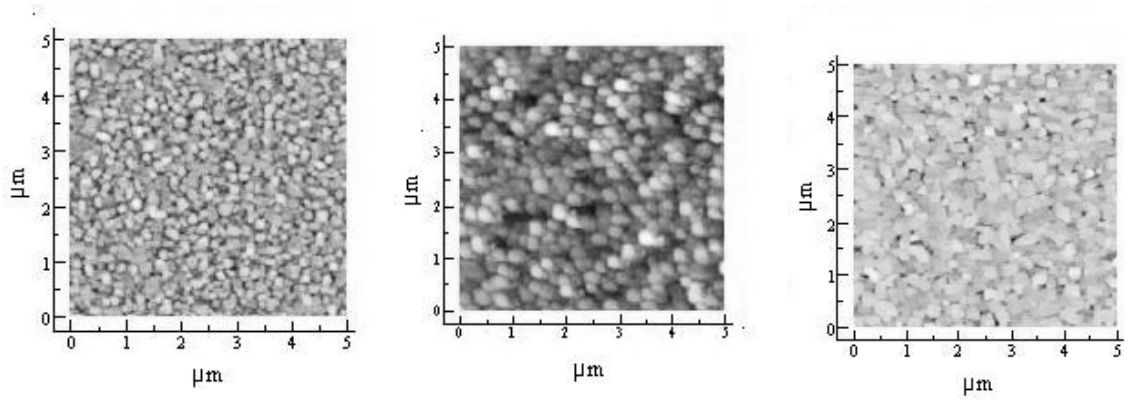

Figure 3.19 Surface AFM micrographs taken on tapping mode of the carbonized surface during the initial stages of growth for (a) decreased C_3H_8 compared to process in Figure 3.12, (b) decreased C_3H_8 and 1 min H_2 etch step compared to process in Fig.1, and (c) process in Fig.1 followed by 1 min H_2 etch step. AFM courtesy of Dr. C. Colletti.

Comparing the initial surfaces after the carbonization process with the surfaces in Figure 3.19 it was determined that the process of Figure 3.19(c) resulted in an improved surface morphology. The latter process provided a surface with cubic-shaped mesas properties which are more in accordance with the cubic properties of 3C-SiC.

3.4.2 Optimization of second thermal ramp

Since the addition of HCl at the second thermal ramp had been demonstrated to lead to surface morphology degradation, optimization was performed by varying the Si/C ratio on the gas stream as well as adding or eliminating steps to the process schedule. From this work it was found that the protrusion defect formation (assessed via AFM) was reduced when the SiH_4 mole fraction was ramped from 1×10^{-4} to 4×10^{-4} during the second thermal ramp.

The optimum carbonization process described in section 3.4.1 followed by the SiH_4 ramp at the second thermal ramp were therefore applied for subsequent deposition experiments which were carried out for extended growth times. A reduction in hillock defects was observed on thinner films with specular morphology. However, surface degradation resulted in non-specular films grown for times in excess of 60-70 minutes. These results suggest that the main problem with defect generation may emanate from the growth step.

3.4.3 Optimization of growth stage

The surface morphology optimization at the growth step was followed by performing Si/C and Si/Cl ratio studies. However the protrusion defect problem persisted. Therefore changes were implemented to the growth step in order to improve the film morphology. It was discovered that when repeated 30 second H_2 etch steps were added during growth after every 10 minutes during growth, the density of the protrusion defects was decreased.

Figure 3.20 shows the growth process schedule including the optimized carbonization followed by the grow/etch step for the 3C-SiC HCl additive process. This

grow/etch step combination was repeated over the desired growth time. Epitaxial films grown using the optimized growth process displayed specular surface morphology with comparable quality to films grown with the process described in Figure 3.12.

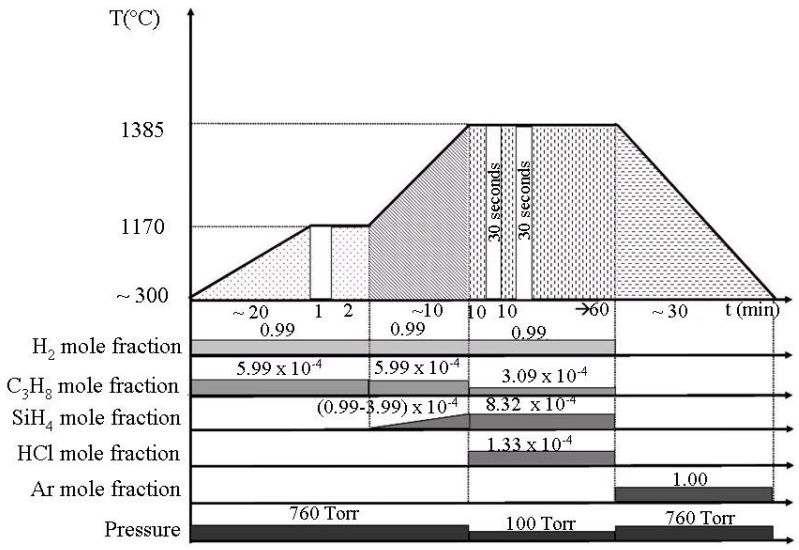

Figure 3.20 Optimized 3C-SiC HCl additive process developed for Geometry I. Mole fraction shown for the 20 µm/h process. A total input flow of 30,038 sccm was used.

Plan view SEM images showed a reduced density of hillock defects that were very similar to films grown with the non-optimized HCl additive processes. Cross-section SEM showed no visible interface problems that may have emanated due to the H_2 etch steps. Although this approach seemed to allow for the growth of thicker films, 30 µm compared to 20 µm, clearly it did not eliminate the protrusion defect problem.

Since it was determined that the growth/etch approach did not provide a solution for the protrusion defect problem, subsequent experimentation was performed using the optimized carbonization and second thermal ramp with the original growth step as shown in Figure 3.12. This approach also yielded epitaxial layers of similar properties to films reported in previous sections and at the same time provided a process with fewer disruptions of the precursor ratios during the growth process. The latter are known to promote the formation of interfaces which could be detrimental for future device applications.

3.5 Process transfer to Geometry II using DOE

Once the 3C-SiC HCl additive process had been developed, characterized and optimized the next step was to apply it to larger area substrates, specifically to 50 mm wafers which is the largest area substrate for which the CVD reactor is currently configured (4" growth possible with a hot-zone change). However, as mentioned before, initial application of the growth process schedule revealed that specular morphology was not achieved over the entire substrate area and on occasion, melting of the silicon substrate occurred. As stated, S. Harvey and Y. Shishkin of our group suggested that the reason for this behavior was the formation of a large temperature gradient of approximately 35ºC along the 50 mm substrate area.[59] As a result of this study it was suggested that a change in the reactor geometry was needed in order to solve the temperature gradient problem. Therefore, Geometry II was implemented (Refer to section 2.2.1 for a more detailed description of the reactor geometries used in this work). These changes produced a more uniform substrate temperature across the 50 mm substrate area. As a result, the experimentally measured temperature variation along the susceptor area was decreased to ±5 ºC.

In addition to the reactor geometry change, the concentration of the silane precursor and the HCl additive gas were changed from 100 % each to more diluted mixtures of 10% SiH_4 in H_2 and 10% HCl in Ar. These changes were performed mainly to gain more control of the mass flow controllers when lower flows were needed. In addition, a lower concentration of HCl was desired for safety considerations due to problems with corrosion of the gas lines.

Because a CVD process is very sensitive to system changes it was imperative to prove that the already developed and optimized process using Geometry I could be applied to Geometry II. Since a change in geometry may cause changes in the system fluid dynamics thus affecting the process growth rate and surface morphology, CFD simulations were initially performed and these CFD simulation results were reported in section 2.2.5.4.

After it was theoretically determined that process transfer from Geometry I to Geometry II may be viable due to the similar fluid dynamics, the focus was shifted to

designing a more efficient experimental design approach to corroborate the process growth rate and process morphology for Geometry II with a minimum number of runs.

Thus far, the "one point at a time" experimental approach had been the main experimental approach followed. This method results in numerous experimental runs and the data obtained is difficult to analyze systematically. Therefore the method of statistical design of experiments (DOE) was implemented. DOE is an experimental strategy for setting up a set of experiments in which all variables are varied in a systematic manner in order to determine correlation between variables and to predict results.[88] Specifically, the fractional factorial experimental design method was employed in this work. The fractional factorial DOE is a variation of the factorial design in which factors are varied together instead of one at a time but only a subset of the experimental matrix is performed.[88] This experimental design enables the experimenter to investigate the individual effects of each parameter and determine whether the parameters interact by performing a limited number of experimental runs. A brief explanation of the DOE construction is provided in Appendix D. Further DOE construction and data analysis details can be found elsewhere.[88]

3.5.1 DOE results

Five factors were taken into consideration for the DOE experiments. These were: temperature, pressure, C_3H_8, SiH_4, and HCl mole fraction. If a full factorial (2^5) design of experiment is considered, then the experiment will require 64 runs if the data is replicated once. Since CVD is a very expensive and time consuming process then a method that decreases the number of runs is very desirable. A one quarter fraction 2^{5-2} of the 2^5 design was chosen since it decreased the number of runs to 8. In addition, a center point design was implemented in order to have an improved estimate of experimental error. The proposed parameter ranges considered are listed in Table 3.5; these were chosen based on the knowledge acquired during the process development using Geometry I. In order to prevent or minimize the effects of nuisance variables from contaminating the results, a completely randomized experimental design was used. The random numbers were generated and sorted using the computer software MATLAB.[89] Finally, the experimental

growth rate was chosen as the response variable to be studied. A summary of the experiments performed with its respective measured response values is presented in Table 3.6 and Table 3.7, respectively.

Table 3.5 Summary of factors range considered to perform 2^{5-2} fractional factorial DOE.

Factor	Range	Units	Mole fraction
Temperature (A)	1300-1380	ºC	---
Pressure (B)	100-400	Torr	---
C_3H_8 flow (C)	6-10	sccm	$2.0 \times 10^{-4} - 3.3 \times 10^{-4}$
SiH_4 flow (D)	11-18	sccm	$3.7 \times 10^{-4} - 6.0 \times 10^{-4}$
HCl flow (E)	1-4	sccm	$0.33 \times 10^{-4} - 1.3 \times 10^{-4}$

Table 3.6 Runs and experimental results for 2^{5-2} DOE

Run	T	P	$y_{C3H8}/10^4$	$y_{SiH4}/10^4$	$y_{HCl}/10^4$	Growth Rate (μm/h)
1	1300	100	2	6	1.3	8.4
2	1380	100	2	3.7	0.3	6.0
3	1300	400	2	3.7	1.3	5.1
4	1300	100	3.3	6	0.3	8.7
5	1380	400	2	6	0.3	6.9
6	1380	100	3.3	3.7	1.3	6.3
7	1300	400	3.3	3.7	0.3	5.4
8	1380	400	3.3	6	1.3	4.8

Table 3.7 Center point runs and experimental results for the 2^{5-2} DOE

Run	T	P	$y_{C3H8}/10^4$	$y_{SiH4}/10^4$	$y_{HCl}/10^4$	Growth Rate (μm/h)
1	1340	250	2.6	4.8	0.83	7.2
2						7.2
3						7.4

After the screening procedure was performed and the response variable was measured, the data was then analyzed by performing an analysis of variance (ANOVA).[88]. The ANOVA results indicated that the main factors affecting the CVD process growth rate were the process temperature, pressure, the SiH_4 and HCl mole fractions as well as the interaction between the process pressure with the C_3H_8 fraction and the interaction between the SiH_4 mole fraction and that of HCl. It is interesting to note that despite that the C_3H_8 fraction by itself does not have a significant effect on growth rate; its interaction with the process pressure provides an effect on growth rate.

Based on the ANOVA analysis, an empirical model that describes the process growth rate within the parameter ranges considered was determined as illustrated in Equation 3.1. In this equation T is temperature, P is pressure, and C_3H_8, SiH_4 and HCl stand for the flow of the respective specie. The model was determined in terms of flows instead of molar fractions in order to facilitate its use during experimentation since these are the typical parameters used during experimentation.

$$GR = 14.1 - 0.01T + 0.002P + 0.80F_{C_3H_8} + 0.557F_{SiH_4} - 0.2HCl$$
$$- 0.001(P)(F_{C_3H_8}) - 0.04(F_{C_3H_8})(F_{SiH_4}) \qquad \text{Equation 3.1}$$

Now that the DOE model was developed, focus was shifted on model validation. The experimental growth rate values for 3 representative runs performed in Geometry II compared to the model predicted growth rates are listed in Table 3.8. As can be seen, the model underestimated the growth rate by approximately 25%.

Table 3.8 DOE model results comparison with experimental values for processes performed using Geometry I.

Run	$y_{C3H8}/10^4$	$y_{SiH4}/10^4$	$y_{HCl}/10^4$	Experimental growth rate Geometry I (μm/h)	DOE predicted growth rate (μm/h)
1	2.0	5.3	.57	10.5	8.0
2	2.0	5.3	0.8	12.0	9.0
3	2.6	5.3	1.0	9.5	7.4

Despite that the model underestimated the process growth rate, it was desired to corroborate if the deposition rate will follow the same experimental trends when compared to the dependences obtained for Geometry I as shown in section 3.3.3. This dependence was selected since most of the experiments had process parameters that fall within the model ranges. In order to accomplish this, the pressure dependence experiments performed on Geometry I were compared to the predicted values from the DOE model for Geometry II. It was not expected that the epitaxial growth rates predicted by the DOE model were accurate since the model was developed in Geometry II which exhibits a different hydrodynamic flow than that of Geometry I. However, a similar pressure effect on deposition growth rate was desired in order to verify that the 3C-SiC process developed for Geometry II will provide similar dependences. As can be seen in Figure 3.21, this indeed was the case. It can be clearly seen that process pressure is inversely proportional to the film growth rate. This result not only agrees with the results obtained for Geometry I but also agrees with CVD theory.[42]

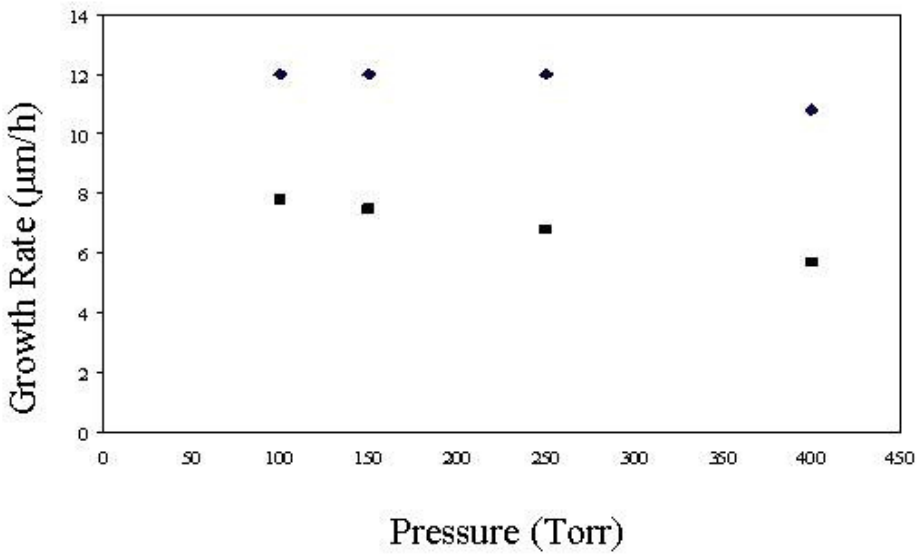

Figure 3.21 Pressure dependence experiments performed on Geometry I (■) compared to the predicted values from the DOE model for Geometry II (▲).

In order to verify if comparatively similar deposition rates could be attained for both reactor geometries; experiments were carried out for the 20, 30 and 38 µm/h

processes using Geometry II and were compared to those obtained in Geometry I. As can be seen in Figure 3.22 Geometry II yielded growth rates values approximately 15% lower than those obtained in Geometry I. Despite the reduction in the deposition rate the data followed the same behavior; the growth rate increased as the silane mole fraction increased.

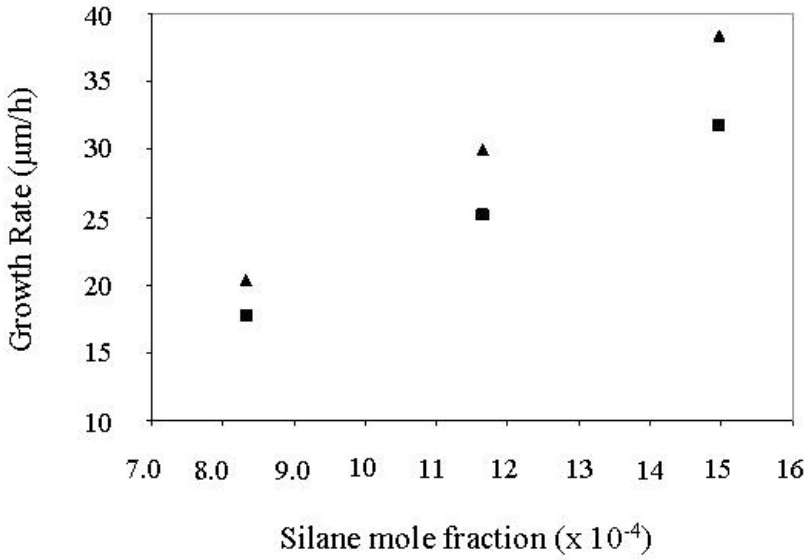

Figure 3.22 Growth rate dependence on SiH_4 mole fraction comparison for the 20, 30 and 38 µm/h grown using Geometry I (▲) and Geometry II (■).

3.6 Growth on 50 mm substrates using Geometry II

After transferring the process to Geometry II, growth was performed on 50 mm silicon substrates to verify if films could be deposited uniformly on the larger substrate. Film thickness measurements were taken via FTIR at 5 different points on the 50 mm substrate as shown in Figure 3.23. Results are summarized in Table 3.9. The epitaxial layers were deposited at the growth speeds of 20, 30 and 38 µm/h. As a reference this process uses Si/C and Si/Cl ratios of 0.9 and 6.5, respectively. Variations in thickness across all measured points were found to be less than 15 %. A slight decrease in growth rate was observed to occur along the gas path. This could be attributed to reactant depletion as species flow across the susceptor. It was also noted that thickness uniformity improved as the growth speed increased.

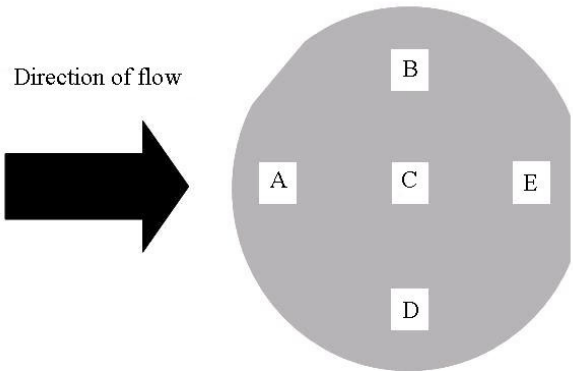

Figure 3.23 Position of the 5 different measurement points considered for film properties evaluation.

Table 3.9 Thickness measurements taken on 3 representative samples grown at a speed of 20, 30 and 38 µm/h. Measurements taken via FTIR.

Growth Rate (µm/h)	Thickness (µm)				
	A	B	C	D	E
20	10.6	10.0	10.3	10.0	9.9
30	10.8	10.4	10.5	10.0	10.3
38	10.8	10.5	10.7	10.5	10.5

Deposition experiments were carried out to evaluate the quality of the epitaxial layers as a function of film thickness and as a function of growth rate. XRD was used to asses the film quality. Powder diffraction was performed first to determine the orientation of the deposited layers. This measurement revealed that the most dominant peaks were located at $\theta = 41°$ which corresponds to the 3C-SiC (200) plane confirming that the films were 3C-SiC (100).Other peaks were observed at the 69 ° and 90 ° positions at much lower intensities. This peaks correspond to (400) 3C-SiC and (200) Si planes, respectively. Table 3.10 provides a summary of the X-ray rocking curve data collected for films grown at 20, 30 and 38 µm/h. The measurements indicated that the film quality degraded as the growth rate and epitaxial thickness increased.

Table 3.10 XRD FWHM summary for films grown at 20, 30 and 38 µm/h.

Growth Rate (µm/h)	Thickness (µm)	FWHM (arcsec)
20	10.2	360
20	20.5	1157
30	10.4	733
38	10.4	854

3.7 Summary

The development of a novel 3C-SiC HCl additive process has been completed on a hot-wall CVD reactor. The growth rate was shown to increase from 12 µm/h for the C_3H_8-SiH_4-H_2 precursor chemistry to 38 µm/h for the HCl additive experiments. The later is the highest reported value in the literature to date.

HCl proved to be highly beneficial to the process growth rate. However, the quality of the epitaxial layers did not significantly improve via the HCl process. Film degradation was observed to occur at increased film thickness and at increased deposition rates for films of the same thickness.

Chapter 4: Low Temperature 3C-SiC Heteroepitaxial Growth

4.1 Overview

In Chapter 3, a 3C-SiC heteroepitaxial growth process via the C_3H_8-SiH_4-HCl-H_2 precursor chemistry was reported. During this work epitaxial growth rates were increased up to 38 μm/h leading to the highest reported value in literature to date for a hot-wall CVD system.[44] Since the later chloride based chemistry demonstrated to be highly beneficial to the process growth rate it was desired to apply this chemistry for the low temperature regime of 1000ºC – 1250ºC (1273K – 1523K). The hypothesis being that the implementation of this precursor chemistry will result in useful epitaxial growth rates and good film quality at the lower deposition temperatures.

Typically, high deposition temperatures (≥ 1350ºC) are required to ensure high quality films and high deposition rates. However, the implementation of low deposition temperatures would be beneficial for device process fabrication. Lower process temperatures will eliminate or decrease problems due to interdependencies with other process steps during device fabrication processes. This will help to avoid problems related to auto-doping, solid state diffusion and alleviate stresses in the epitaxial layers.[3] In addition, lower deposition temperatures are attractive for selective epitaxial growth (SEG) applications where lower deposition temperatures are needed to avoid damage to the required silicon dioxide (SiO_2) mask.[3]

The experiments described in this chapter were performed using the USF CVD reactor configured with Geometry II as described in section 2.2.1. A two-step carbonization and growth process was also applied. Ultra high purity hydrogen, purified via a palladium cell, served as the carrier gas during the deposition process. The carbon and silicon precursors were provided by C_3H_8 (100%) and a mixture of 10% SiH_4 in H_2, respectively. Finally, the mixture of 10% HCl in Ar was used as the chloride growth

additive. Planar n-type Si (001) samples diced into 8 mm x 10 mm die were used in this study. The substrates were cleaned using an RCA cleaning procedure preceding deposition. A 30 second immersion into a hydrogen fluoride (HF, 50:1) was performed before loading the sample to the reactor. Unfortunately, at the moment this study was being performed several malfunctions on the HCl manifold occurred until it was completely disabled. Therefore, this study is somewhat limited because all experimentation including HCl additive had to be discontinued for safety considerations.

Nomarski optical microscopy and secondary electron microscopy (SEM) were used to qualitatively analyze film surface morphology after growth. SEM and Fourier transform infrared (FTIR) reflectance were used for film thickness determination. Atomic force microscopy (AFM) qualitatively assessed the surface morphology. X-ray diffraction (XRD) provided information on the crystal quality.

4.2 Low-temperature 3C-SiC growth process development

4.2.1 Carbonization

Before conducting the growth experiments, the silicon substrates were carbonized using the already developed process described in section 3.2.1. As a reminder, during this process a thermal ramp was conducted to raise the sample temperature from approximately 300°C to 1170°C in the presence of a gas stream composed of H_2 and C_3H_8. The gas stream total flow was 10,006 sccm which had a C_3H_8 molar fraction of 6.0 $x10^{-4}$. Finally the sample temperature was held at 1170°C for two minutes.

4.2.2 Growth stage

In order to determine the most favorable conditions for the growth stage, a resolution IV screening design of experiments (DOE) was implemented. For this, a two-level one quarter (2^{6-2}) fractional factorial design which included 16 runs and four center points was carried out to investigate the process parameter space. The center point design was applied in order to have an improved estimate of experimental error since the data was not replicated. No main effects are aliased with any other main effect or with any other two-factor interaction. The variables include the process temperature, pressure and

the hydrogen, propane, silane and hydrogen chloride mole fractions. A constant growth time of 40 minutes was targeted for all runs. A completely randomized design was implemented to avoid or minimize the effects of nuisance variables. The random numbers were generated by using the computer software MATLAB.[89] The response variable considered was the process deposition rate. A summary of the factor parameters and the experimental matrix with its respective measured response are provided in Table 4.1 and Table 4.2, respectively. The center point data is provided on Table 4.3

Table 4.1 Summary of factors range considered to perform 2^{6-2} fractional factorial DOE

Factors	Range	Units	Mole fraction
Temperature	1150-1250	ºC	---
Pressure	100-400	Torr	---
H_2	10-20	sLm	0.99
C_3H_8	3-5	sccm	$1.5 \times 10^{-4} - 5.0 \times 10^{-4}$
10% SiH_4 in H_2	40-90	sccm	$2.0 \times 10^{-4} - 9.0 \times 10^{-4}$
10% HCl in Ar	0-20	sccm	$0 - 2.0 \times 10^{-4}$

Table 4.2 Experimental matrix and response values for 2^{6-2} DOE

Run	Temperature	Pressure	H_2	C_3H_8	SiH_4	HCl	Growth Rate (µm/h)
1	1250	400	20	3	40	0	0.2
2	1150	400	20	5	90	0	1.5
3	1150	100	20	3	90	20	0.8
4	1250	100	10	5	90	20	0.4
5	1150	400	10	5	40	20	0.1
6	1250	400	10	3	40	20	0.1
7	1250	100	20	5	40	20	0.8
8	1150	100	10	3	90	20	0.6
9	1150	400	10	3	40	0	0.1
10	1250	400	10	5	90	0	0.1
11	1250	100	20	3	90	0	2.2
12	1150	100	10	5	90	0	0.6
13	1250	400	20	5	40	0	0.8
14	1150	100	20	5	40	0	0.6
15	1150	100	20	3	40	20	0.7
16	1250	400	10	3	90	20	0.1

Table 4.3 Center point runs and response values for 2^{6-2} DOE

Run	Temperature	Pressure	H2	C3H8	SiH4	HCl	Sample ID
17	1200	250	15	4	65	10	0.9
18							0.7
19							0.8
20							0.8

An analysis of variance (ANOVA) was performed after the experimental matrix was completed and the response variable was measured. The ANOVA results indicated the process pressure and the molar fractions of hydrogen and propane were among the most significant factors affecting the epitaxial growth rate. In addition, the interaction between the process pressure and the propane mole fraction as well as the process pressure interaction with the hydrogen and propane molar fractions played major roles. The ANOVA analysis elucidated the empirical model that describes the process growth rate as shown in Equation 4.1. In this equation P stands for pressure, and F_{C3H8}, F_{H2} stands for the flow of the respective specie. The model was determined in terms of flows instead of molar fractions in order to facilitate its use during experimentation since this are the typical parameters used.

$$GR = 0.61 - 0.23P + 0.31PF_{H2}F_{C3H8} + 0.25PF_{C3H8} + 0.34F_{H2} \qquad \text{Equation 4.1}$$

After the empirical model from the ANOVA analysis was obtained, it was then used to manipulate the process parameters with the aim to obtain the combination of variables that resulted in the highest deposition rate and a specular surface morphology. It was determined that the maximum predicted growth rate that could be attained for the process parameter space considered was 2 μm/h. Figure 4.1 describes the growth process conducted to achieve that deposition rate target value. Once the carbonization process was performed the sample temperature was raised from 1170 ºC to the growth temperature of 1250ºC at a rate of 15 ºC per minute. After the growth temperature was attained the process pressure was lowered to 100 Torr and the total gas flow (H_2, C_3H_8, SiH_4 and Ar) was set to 20,093 sccm. The C_3H_8 and SiH_4 molar fractions at the growth stage were 1.5 x 10^{-4} and 4.5 x 10^{-4}, respectively. At these process conditions the process Si/C ratio was 1.0. It should be noted that the model predicted the highest deposition rate

occurred when HCl was not present in the precursor chemistry, confirming that HCl would not have a significant impact on the deposition rate.

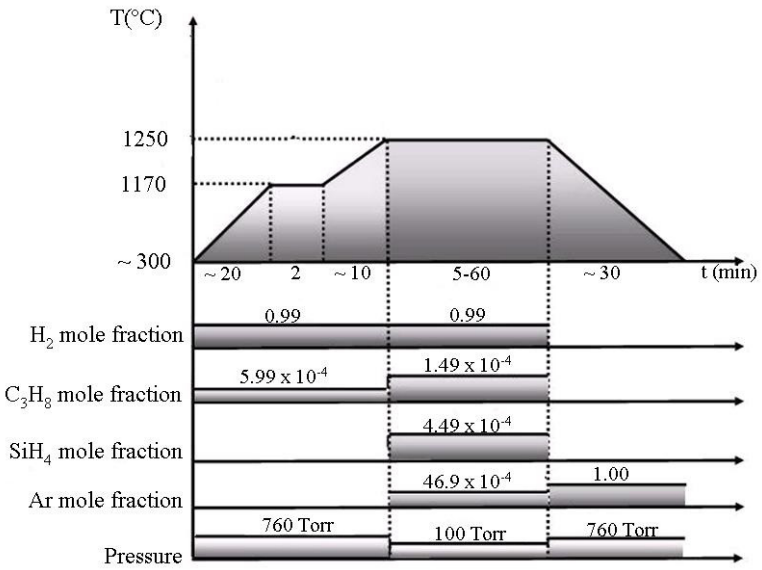

Figure 4.1 3C-SiC growth process schedule for optimum process predicted by ANOVA analysis. Mole fractions presented for 2 μm/h process. At the growth stage the total input gas flow (H_2, C_3H_8, SiH_4 and Ar) was set to 20,093 sccm. Process Si/C=1.0.

4.2.3 Growth rate dependence on HCl mole fraction

The ANOVA findings suggested that no significant increase in deposition rates will be obtained at the low temperature regime due to HCl not having a significant effect on this response variable. However, it was decided to perform a study on the growth rate dependence on HCl mole fractions. This was in order to investigate the effect of HCl on the film quality and surface morphology which in this study was hypothesized to be enhanced by the presence of HCl.

It was determined to utilize the growth process described in section 4.2.2 as the starting point for the HCl additive experiments as this process was well documented. Figure 4.2 illustrates the growth rate dependence on HCl mole fraction. For these experiments the HCl mole fraction was increased from 0 to 1 x 10^{-4}, while the process temperature, pressure and Si/C ratio were kept constant at 1250ºC, 100 Torr and 1.0, respectively. As can be observed, the deposition rate remained fairly constant up to mole

fractions of approximately 0.5 x 10^{-4} after which the rate began to decrease. The study was concluded at the HCl mole fraction of 1 x 10^{-4} where the epitaxial surface morphology became rough and non specular. This was attributed to preferential surface etching as a consequence of the high HCl mole fractions.

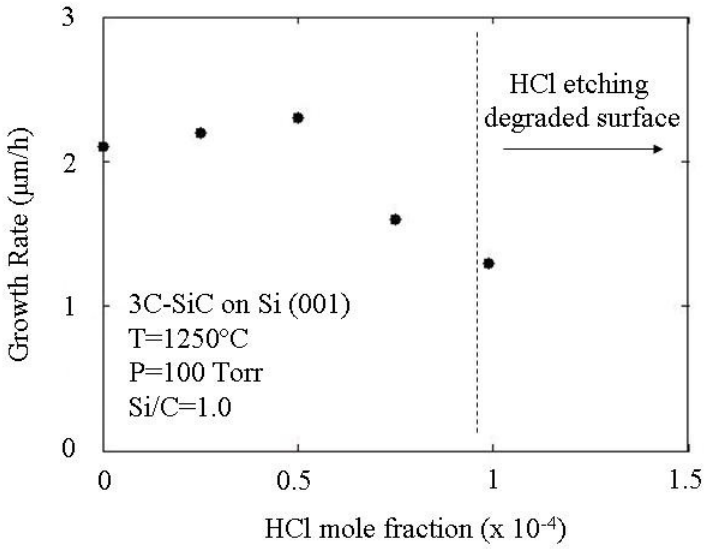

Figure 4.2 Growth rate dependence on HCl mole fraction. The process temperature, pressure and Si/C ratio were kept constant at 1250ºC, 100 Torr and 1.0; respectively.

The epitaxial layers were characterized via SEM. Plan view images of representative films grown using 0, 0.25 x 10^{-4} and 0.75 x 10^{-4} HCl mole fractions to the process described in section 4.2.2 are shown in Figure 4.3. As can be observed, the process with no HCl additive yielded a more mosaic like structure typically observed for 3C-SiC layers due to the presence of antiphase domain boundaries. However, as the HCl mole fraction was increased, the surface morphology became smoother.

This result was confirmed when the same samples were inspected via AFM as shown in Figure 4.4. The surface roughness of the films decreased from 23.9 to 2.3 nm RMS with increased HCl mole fraction. It could also be observed that the HCl additive lead to larger and better oriented antiphase domain boundaries. In addition, the epitaxial layer thickness decreased with increased HCl mole fraction, further confirming that surface etching was possibly the predominant mechanism that leads to improved surface

morphology. Finally, the experimental data suggested that adding HCl to the growth process shown in Figure 4.1 at a mole fraction of 0.75 x 10^{-4} will result in the optimum surface morphology. At these conditions the process Si/Cl ratio was determined to be 6.0 and the epitaxial growth rate was calculated to be ~ 1.7 μm/h.

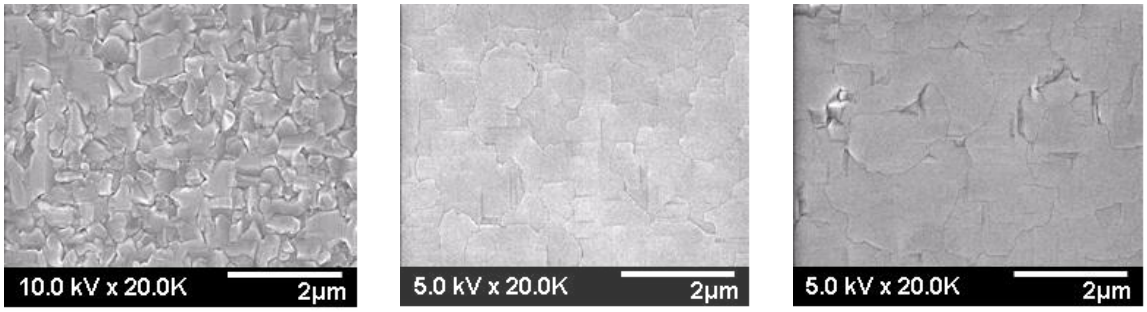

(a) (b) (c)

Figure 4.3 Plan view SEM images for representative films grown with HCl addition at mole fractions (a) 0, (b) 0.25 x 10^{-4} and (c) 0.75 x 10^{-4}. Note the surface morphology improvement as the HCl mole fractions are increased.

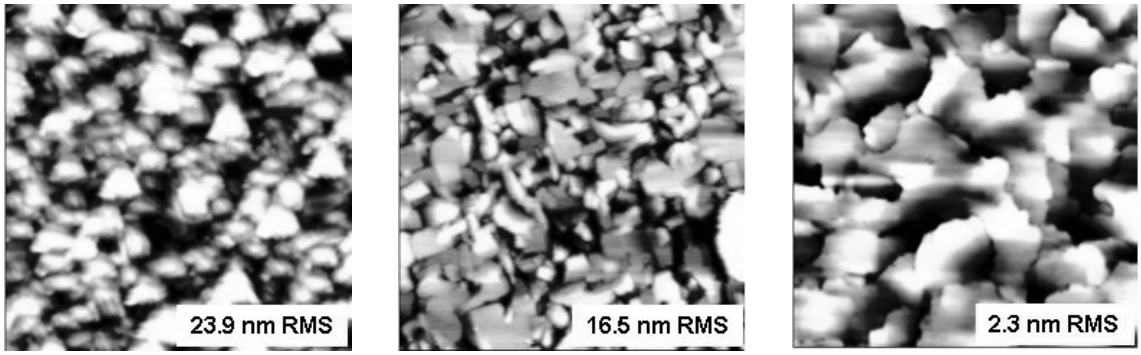

(a) (b) (c)

Figure 4.4 AFM micrographs taken in contact mode for representative films grown with HCl addition at mole fractions of (a) 0, (b) 0.25 x 10^{-4} and (c) 0.75 x 10^{-4}. Note the surface morphology improvement as the HCl mole fractions are increased

4.2.4 Growth rate as a function of temperature

After determining the optimum HCl additive process, a study of growth rate dependence on temperature was conducted since lower temperatures were desired as explained earlier. The growth parameters for the temperature study were maintained at

P=100 Torr, Si/C=1.0 and Si/Cl=6.0 while the process temperature was varied from 1000ºC to 1250ºC as illustrated in Figure 4.5. In this temperature range process growth rates from 0.5 to 1.7 μm/h respectively were obtained. At temperatures lower than 1150ºC polycrystalline films were obtained. Specular surface morphology was obtained for all films grown at temperatures of 1150ºC and above.

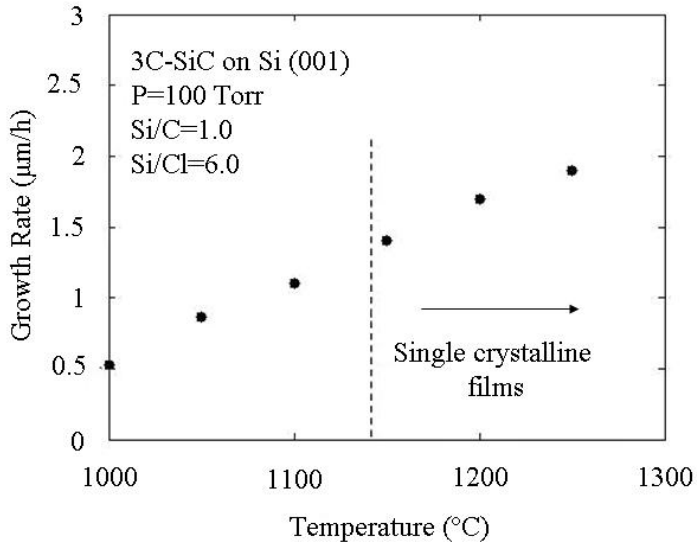

Figure 4.5 Growth rate dependence on temperature. Single crystalline films obtained from temperatures of 1150ºC.

4.2.5 Growth rate as a function of silane mole fraction

In an effort to increase the deposition growth rate over the lower temperature regime, experiments were conducted where the silane mole fraction was increased while keeping a constant temperature and pressure of 1250ºC. This temperature was chosen to perform this study since at lower temperatures polycrystalline films were obtained at increased mole fractions. The process Si/C and Si/Cl ratios were also kept constant at 1.0 and 6.0, respectively. The silane mole fraction was varied from 4.3×10^{-4} to 7.8×10^{-4} as shown in Figure 4.6. Polycrystalline films were obtained for silane mole fractions from 6.7×10^{-4} and above indicating that the silane saturation point had been reached at this process temperature. Films with specular surface morphology were obtained at silane mole fractions lower than 6.7×10^{-4}. The highest growth rate achieved in this study was

2.5 μm/h. This was achieved for a SiH_4 mole fraction of 5.3 x 10^{-4}. This study is in agreement with the ANOVA results which indicated that the deposition rate would not be significantly improved by the presence of HCl.

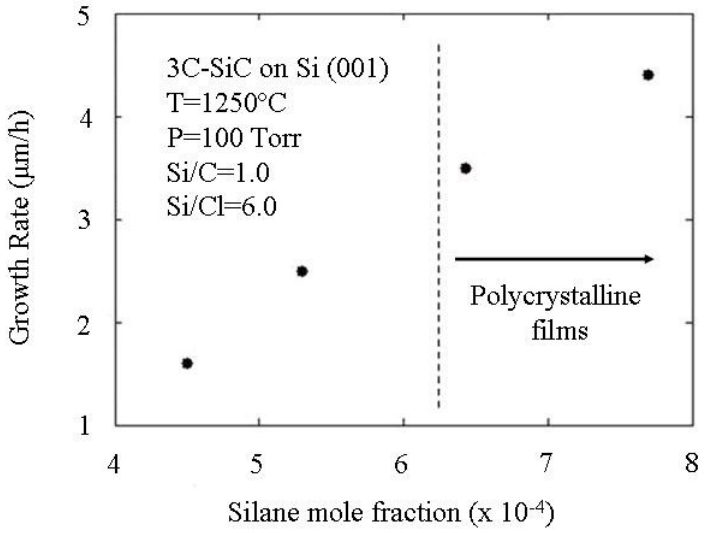

Figure 4.6 Growth rate dependence in SiH_4 mole fraction. Pollycristalline films obtained at mole fractions from 6.7 x 10^{-4}.

In order to evaluate the quality of the films grown at the highest deposition rate achieved for the low temperature growth, a 2 μm thick film grown at a rate of 2.5 μm/h was deposited and analyzed via XRD. Unfortunately, thicker films could not be grown due to malfunctions of the HCl manifold mentioned earlier. Figure 4.7 shows the XRD rocking curve of the (200) 3C-SiC diffraction peak. The FWHM was determined to be ~ 278 nm arcsec. This value compares to values reported in literature and it is also comparable with films grown in this study at elevated temperatures which indicates good quality film.

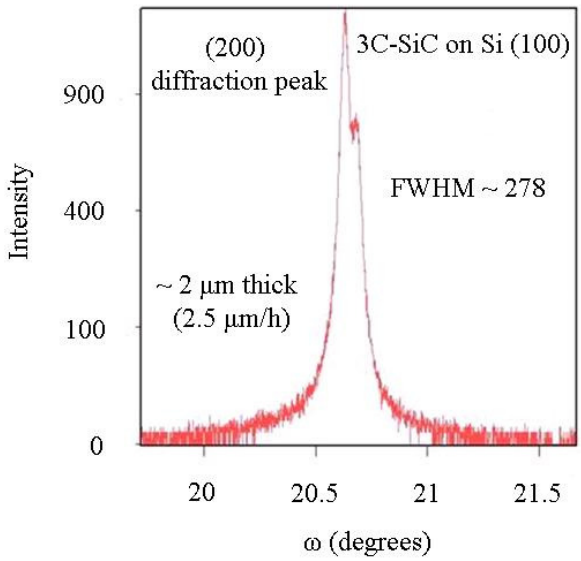

Figure 4.7 XRD rocking curve of a 2 µm thick epitaxial layer grown at a rate of 2.5 µm/h The FWHM was ~278 arcsec and compares with values reported elsewhere.[44]

4.3 Summary

The development of a 3C-SiC growth process at low deposition temperatures has been completed. The highest growth rate achieved was 2.5 µm/h which was obtained at a temperature of 1250ºC.

HCl proved to be highly beneficial to the process surface morphology. However, the epitaxial layer growth rate did not significantly improve via the HCl process suggesting that etching of the film surface dominates in the lower temperature regime.

Chapter 5: Summary and Future Work

5.1 Dissertation summary

This dissertation research focused on the heteroepitaxial growth of 3C-SiC layers by CVD at two deposition temperature regimes using a chloride additive to the SiH_4-C_3H_8-H_2 precursor chemistry system. The hypothesis under investigation was to determine if chloride based chemistry will aid to increase the epitaxial layers growth rate and material quality via reduced defects. Characterization of the films was carried out via Nomarski interference optical microscopy, FTIR, SEM, AFM, XRD and XPS.

Thermodynamic equilibrium calculations were performed to obtain a criterion as to which chloride specie should be used during growth experimentation. During this study the following chloride containing groups of species were considered: chlorocarbons, chlorosilanes, and hydrogen chloride. It was concluded from this work that no differences in most dominant species present on the equilibrium composition mixture were observed between adding HCl or using chlorocarbons or chlorosilane as the chloride additive source. Therefore, HCl was chosen since it has been suggested that the addition of HCl allows for the enhancement of both the growth rate and surface morphology. This is believed to be accomplished by the creation of intermediate species such as Si_xCl_y, which increases the silicon atomic content in the gas mixture. Work performed, particularly on the homo-epitaxial growth of 4H-SiC, revealed that HCl addition to the standard chemistry increased the film growth rate by allowing higher silane process mole fractions otherwise not possible with the standard chemistry.[66]

CVD CFD simulations were also performed to determine the gas velocity and temperature profiles along the reactor. In addition they aid in the study of the changes in flow and temperature profiles due to reactor geometry changes. The simulation predicted that gas surrounding the susceptor area was at a constant temperature. However, the

temperature profile did not agree with the experimentally measure temperature profile along the susceptor which showed a 35ºC difference along the flow direction for Geometry I and 5ºC for Geometry II. This is mainly attributed to the fact that the simulation does not account for heat losses by radiation. The velocity profile revealed that the reactor is operating at the desired laminar flow conditions. Laminar flow is desired in order to deliver the gas uniformly to the substrate in order to obtain uniform films and avoid intermixing of gas concentrations[56]

Once it was decided which chloride specie was to be used to test the hypothesis, then experiments were performed. A 3C-SiC growth process was developed on Si (001) substrates at high temperatures (1385ºC). The process development was performed in two stages. First, a "baseline" process without HCl additive was developed. Second, the baseline process was used as the starting process to develop the HCl additive experiments. The growth process was achieved by performing a two-step growth consisting of carbonization of the silicon substrate and growth of the epitaxial layer.

The baseline process was developed at a temperature of 1385ºC and a pressure of 100 Torr. The process Si/C was set to be 0.72. At this process conditions a maximum growth rate of 12 μm/h was achieved. Surface roughness values of 1.6 nm RMS were obtained in films the grown. The resulting layers presented specular surface morphology and SEM analysis revealed that no voids were present at the 3C-SiC/Si interface. The XRD rocking curve of the 3C-SiC (002) peak revealed a FWHM of 500 arcsec which compares to values reported elsewhere.[45]

After corroborating that the baseline process was repeatable, the process was then used as the starting point for the HCl additive experiments. The HCl addition to the baseline process allowed growth rates up to ~38 μm/h to be achieved. This is the highest reported value reported in the literature to date for 3C-SiC heteroepitaxy. During the development of this process film degradation was noted at increased film thickness and at increased growth speeds for samples of the same thickness. The film degradation was attributed to the formation of protrusion or hillocks at the film surface. Despite much effort to optimize the growth process the surface degradation could not be solved. The higher film thickness obtained in this work was 30 μm. XDR characterization performed

showed FWHM values from 220 to 1160 arcsec depending on the process growth speed or film thickness. These values are better or comparable to those reported in literature and to those obtained for the baseline process.[45] Finally, it was concluded from this study that at high deposition temperatures the addition of HCl to the precursor chemistry impacted more significantly the epitaxial layer's growth rate.

After finishing the high temperature experiments focus was shifted to test the hypothesis for the low-temperature (1000-1250ºC) growth of 3C-SiC. In addition a low temperature process could potentially be beneficial for device process applications. The growth process was also performed using a two step growth: carbonization of the silicon substrate followed by the deposition of the epitaxial layer. To develop this process a 2^{6-2} fractional factorial DOE was carried out. The factors considered were the process temperature, pressure and the propane, silane, hydrogen and hydrogen chloride mole fractions. The response under consideration was the process growth rate. The experimental results were analyzed by performing and ANOVA analysis. The ANOVA analysis suggested that the main factors controlling the 3C-SiC growth at the lower temperature regime were the process pressure and the molar fractions of hydrogen and propane. In addition the interaction between the process pressure and the propane mole fraction as well as the process pressure interaction with the hydrogen and propane molar fractions. An empirical model was developed from the ANOVA analysis to predict the epitaxial growth rates. This empirical model predicted that the highest growth rate that could be obtained within the parameter space under consideration was 2 μm/h; this was confirmed experimentally. The process parameters to achieve this growth rate where T= 1250ºC, P=100 Torr and a Si/C=1.0. Although the analysis suggested that HCl would not impact significantly the process growth rate; HCl experiments were carried out using the process described as the starting point. With the HCl additive the epitaxial growth rate could only be increased to ~2.5 μm/h. The effect of HCl addition to the surface morphology was studied. It was observed that smoother and flatter surfaces were obtained at increased HCl mole fractions. AFM measurement revealed that the surface roughness was 10 times smaller for the optimum HCl additive process compared to the process without HCl additive predicted by the ANOVA model. An XRD FWHM of 278

arcsec was measured on a 2 μm thick representative layer. This value is comparable to the best values reported in the literature as well as to films grown at higher deposition temperatures in this study. It was concluded from this work that at lower deposition temperatures the HCl addition was more beneficial for the film quality by enhancing surface morphology via surface etching.

5.2 Future work and current work

5.2.1 Species concentration profile simulation

Unfortunately, a final numerical solution for the species concentration profile along the reactor has not been established in this work due to problems with the COMSOL platform. The work performed to date allows for the transient solution of the gas phase reaction kinetics considered in this work. The species concentrations as a function of time are presented in the next set of figures. The calculations are based on a perfectly mixed batch reactor kept at 1385ºC which is the process temperature of the 3C-SiC HCl additive growth process at high temperatures develop in Chapter 3. For visualization purposes the species have been graphed into four different sets: hydrocarbon species in Figure 5.1, silicon containing species in Figure 5.2, chlorocarbon species in Figure 5.3 and chlorosilane species in Figure 5.4.

After the COMSOL platform issues are resolved and a numerical solution for the species concentration profile and the process growth rate for CVD reactor could be obtained, the 3C-SiC growth processes developed in this work will be simulated. In addition, the 3C-SiC heteroepitaxial processes on Si (111) surfaces currently being developed by C. Locke and C. Frewin from our group will be simulated. Finally, additional experimentation has to be performed if needed to validate the model for the process growth rate prediction.

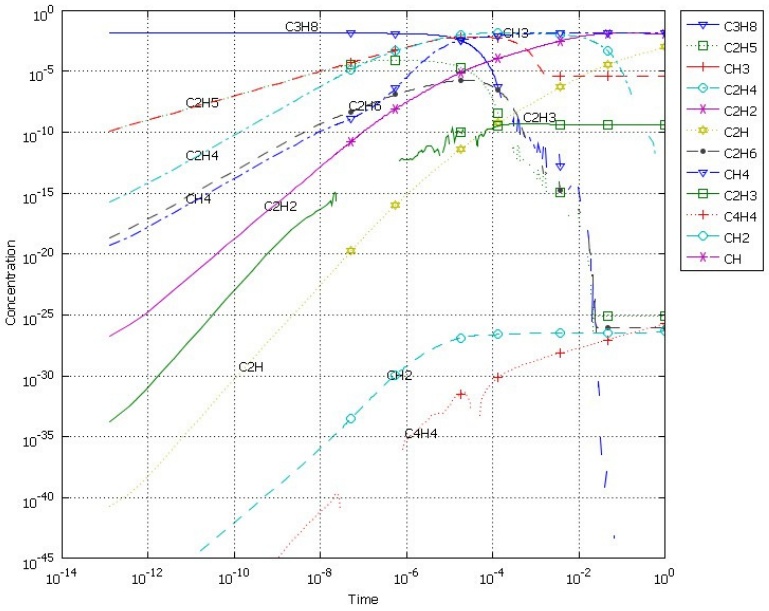

Figure 5.1 Calculated species concentration as a function of time for hydrocarbon species based on a perfectly mixed reactor kept at 1385ºC.

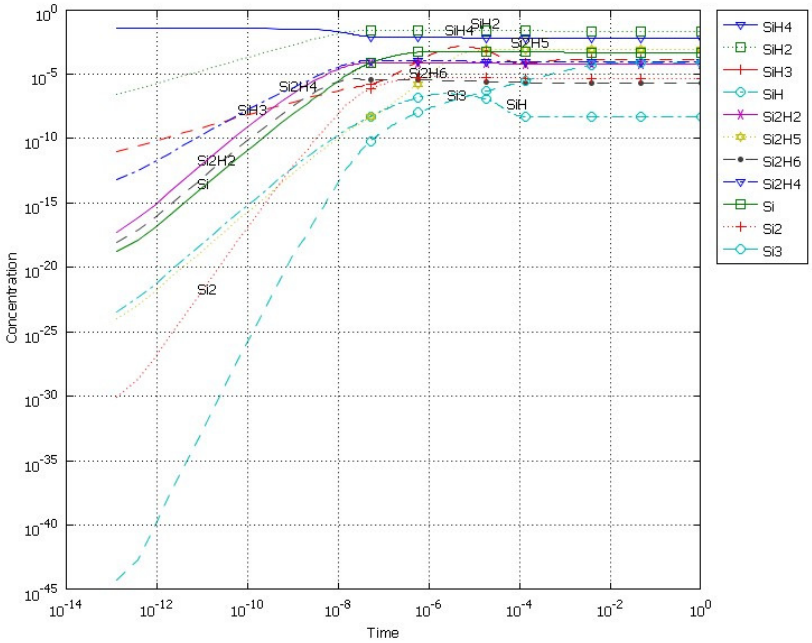

Figure 5.2 Calculated species concentration as a function of time for silicon containing species based on a perfectly mixed reactor kept at 1385ºC

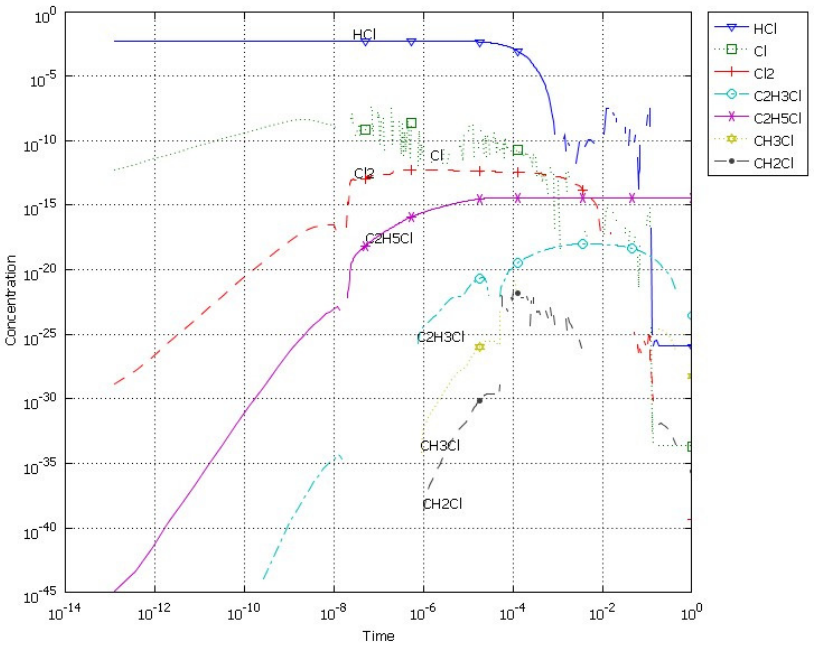

Figure 5.3 Calculated species concentration as a function of time for chlorocarbon species based on a perfectly mixed reactor kept at 1385ºC.

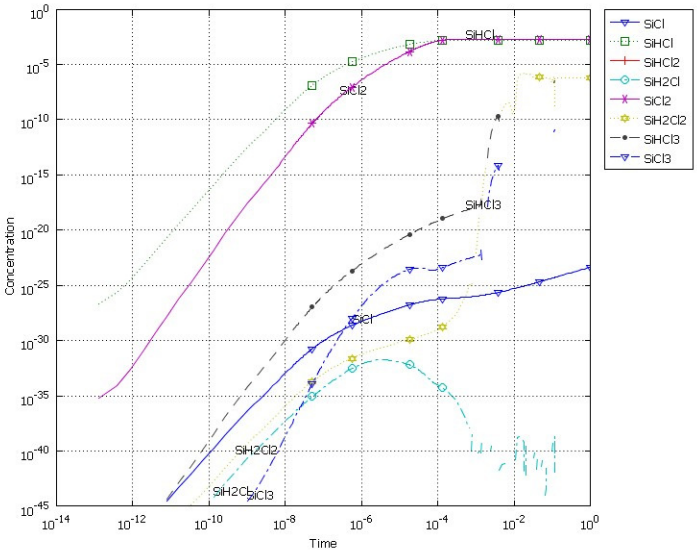

(b)

Figure 5.4 Calculated species concentration as a function of time for chlorosilane species based on a perfectly mixed reactor kept at 1385ºC.

5.2.2 Temperature profile simulation

The design of the reactor chamber is crucial for maintaining a uniform sample temperature profile and efficient heating. It is especially important that the quartz tube surrounding the susceptor remains at moderate temperatures. In this work a temperature profile of the gas system along the susceptor area failed to predict the temperature gradients observed experimentally. Therefore, a more in depth simulation that examines the RF inducted heating of the graphite susceptor and takes into account heat losses by radiation could provide a better estimate of the temperature distribution over the sample area.

References

[1] J. B. Casady and R. W. Johnson, Solid-State Electronics 39**,** 1409-142 (1996).

[2] M. Mehregany, C. A. Zorman, N. Rajan, and C. H. Wu, Proceedings of the IEEE 86**,** 1594-1610 (1998).

[3] A. Gupta and C. Jacob, Progress in Crystal Growth and Characterization of Materials 51**,** 43-69 (2005).

[4] Y. Goldberg, M. E. Levinshtein, and S. L. Rumbayantsev, in *Properties of Advance Semiconductor Materials*, edited by M. E. Levinshtein, S. L. Rumyantsev, and M. S. Shur (John Wiley & Sons, New York, NY, 2001), p. 93.

[5] ACD/ChemSketch; 10.0 ed. (1997-2006).

[6] S. E. Saddow and A. Agarwal, *Advances in Silicon carbide: Processing and Applications* (Artech House INC., Norwood, MA 2004).

[7] C.-M. Zetterling and M. Ostling, in *Process Technology for Silicon Carbide*, 2 ed., edited by C.-M. Zetterling (INSPEC, London, U.K., 2002).

[8] A. R. Powell and L. B. Rowland, Proceedings of the IEEE 90**,** 942-955 (2002).

[9] M. Abe, H. Nagasawa, P. Ericsson, H. Strömberg, M. Bakowski, and A. Schöner, Microelectronic Engineering 83**,** 24-26 (2006).

[10] H. Nagasawa, K. Yagi, T. Kawahara, N. Hatta, and M. Abe, Microelectronic Engineering 83**,** 185-188 (2006).

[11] J. Wan, M. A. Capano, M. R. Melloch, and J. A. Cooper, IEEE Electron Device Letters 23**,** 482-484 (2002).

[12] http://www.mdatechnology.net/techsearch.asp?articleid=174#sec6.

[13] O. Kordina and S. E. Saddow, in *Advances in Silicon Carbide Processing and Applications* edited by S. E. Saddow and A. Agarwal (Artech House, INC, Norwood, MA, 2004), p. 1-27.

[14] P. G. Neudeck, R. S. Okojie, and L.-Y. Chen, Proceedings of the IEEE 90**,** 1065-1076 (2002).

[15] SiC technology will meet the military's future need (2007).

[16] Silicon carbide set to reduce the size of hybrid electricengines (2005).

[17] http://www.semiconductorglossary.com.

[18] C. I. Harris, S. Savage, A. Konstantinov, M. Bakowski, and P. Ericson, Applied Surface Science 184**,** 393-398 (2001).

[19] J. Hornberger, A. B. Lostetter, K. J. Olejniczak, T. McNutt, S. M. Lal, and A. Mantooth, IEEE Aerospace Conference Proceedings 4**,** 2534-2555 (2004).

[20] Y. T. Yang, K. L. Ekinci, X. M. H. Huang, L. M. Schiavone, M. L. Roukes, C. A. Zorman, and M. Mehregany, Applied Physics Letters 78**,** 162-164 (2001).

[21] S. E. Saddow, M. E. Okhuysen, M. S. Mazzola, M. Dudley, X. R. Huang, W. Huang, and M. Shamsuzzoha, in *Characterization of Single-Crystal 3C-SiC on Si Epitaxial Layers*, Boston, MA, 1999, p. 107-112.

[22] N. Nordell, in *Process Technology for Silicon Carbide*, 2 ed., edited by C.-M. Zetterling (INSPEC, London, U.K., 2002), p. 13-50.

[23] S. Nishino, Y. Hazuki, H. Matsunami, and T. Tanaka, Journal of the Electrochemical Society 127**,** 2674-2680 (1980).

[24] J. A. Powell, L. G. Matus, and M. A. Kuczmarski, Journal of the Electrochemical Society 134**,** 1558-1565 (1987).

[25] K. Yagi and H. Nagasawa, Journal of Crystal Growth 174**,** 653-657 (1997).

[26] N. Nagasawa and Y.Yagi, Phys. Stat. Sol. B 202**,** 335-358 (1997).

[27] S. I. Molina, F. M. Morales, and D. Araújo, Materials Science and Engineering B80, 342-344 (2001).

[28] C.-F. Wang and D.-S. Tsai, Materials Chemistry and Physics 63, 196-2001 (2000).

[29] O. Kordina, L.-O. Björketun, A. Henry, C. Hallin, R. C. Glass, L. Hultman, J.-E. Sundgreen, and E. Janzén, J. Cryst. Growth 154, 303-314 (1995).

[30] M. Reyes, M. Waits, S. Harvey, Y. Shishkin, B. Geil, J. T. Wolan, and S. E. Saddow, Materials Science Forum 527-529, 307-310 (2006).

[31] G. Ferro, J. Camasel, S. Juillaguet, C. Ballaud, E. K. Polychroniadis, Y. Stoemenos, J. Dazord, H. Peyre, Y. Monteil, S. A. Rushworth, and L. M. Smith, Semiconductor Science Technology 18, 1015-1023 (2003).

[32] J.-H. Boo, K.-S. Yu, M. Lee, and Y. Kim, Applied Physics Letters 66, 3486-3488 (1995).

[33] H. Nakasawa and M. Suemitsu, Applied Physics Letters 79, 755-757 (2001).

[34] A. Figueras, S. Garelik, R. Rodríguez-Clemente, B. Armas, C. Combescure, and C. Dupuy, Journal of Crystal Growth 110, 528-542 (1991).

[35] J. Hofmann and S. Veprek, Thin Solid Films 318, 18-21 (1998).

[36] D. J. Larkin, P. G. Neudeck, J. A. Powell, and L. G. Matus, Applied Physics Letters 65 (1994).

[37] P. A. Coon, P. Gupta, M. L. Wise, and S. M. George, Journal of Vacuum Science Technology A 10, 324-333 (1992).

[38] V. S. Ban and S. L. Gilbert, Journal of the Electrochemical Society 122, 1382-1388 (1975).

[39] Private communication.

[40] R. L. Myers, O. Kordina, Z. Shishkin, S. Rao, R. Everly, and S. E. Saddow, Material Science Forum 483-485 73-76 (2005).

[41] F. L. Via, G. Galvagno, A. Firrincieli, F. Roccaforte, S. D. Franco, A. Ruggiero, M. Barbera, R. Reitano, P. Musumeci, L. Calcagno, G. Foti, M. Mauceri, S. Leone, G. Pistone, F. Portuese, G. Abbondanza, G. Abagnale, G. L. Valente, and D. Crippa, Material Science Forum 527-529 163-166 (2006).

[42] K. K. Schuegraf, *Hanbook of Thin Film Deposition Process and Techniques: Principles, Methods, Equipment and Applications* (Noyes Publications, Park Ride New Jersey, 1988).

[43] Y. Gao, J. H. Edgar, J. Chaudhuri, S. N. Cheema, M. V. Sidorov, and D. N. Braski, J. Cryst. Growth 191**,** 439-445 (1998).

[44] M. Reyes, Y. Shishkin, S. Harvey, and S. E. Saddow, Materials Research Society Spring Meeting Proceedings 911**,** 79 (2006).

[45] T. Chassagne, A. Leycuras, C. Balloud, P. Arcade, H. Peyre, and S. Juillaguet, Mat. Sci. Forum 457-460**,** 273 (2004).

[46] D. L. Smith, *Thin-film deposition: principles and practice* (McGraw Hill, Inc, 1995).

[47] http://composite.about.com/library/glossary/d/bldef-d1722.htm.

[48] http://www.sp.phy.cam.ac.uk/~SiGe/Misfit.html.

[49] S. Mahajan and K. S. S. Harsha, *Principles of growth and processing of semiconductors* (McGraw Hill, 1999).

[50] http://www.tf.uni-kiel.de/matwis/amat/def_en/index.html.

[51] J. Yun, T. Takahaski, T. Mitani, Y. Ishida, and H. Okumura, Journal of Crystal Growth 291**,** 148-153 (2006).

[52] J. Yun, T. Takahashi, Y. Ishida, and H. Okumura, Journal of Crystal Growth 291**,** 140-147 (2006).

[53] X. H. Zeng, B. Qu, Y. T. Wang, Z. Z. Dai, J. Y. Han, H. Yang, and J. W. Liang, Journal of Crystal Growth 233**,** 40-44 (2001).

[54] http://en.wikipedia.org/.

[55] K. Seshan, *Handbook of thin film deposition processes and techniques: Principles methods and Applications* (Noyes Publications, Norwich, New York, 2002).

[56] A. Sherman, *Chemical Vapor Deposition for Microelectronics: Principles Technology and Applications* (Noyes Publications, Westwood, N. J. USA, 1987).

[57] R. L. Myers, Thesis, University of South Florida, 2003.

[58] M. T. Smith, Thesis, University of South Florida, 2003.

[59] S. Harvey, Thesis, University of South Florida, 2006.

[60] J. M. Smith, H. C. Van Ness, and M. M. Abbott, *Introduction to Chemical Engineering Thermodynamics*, 6th ed. (McGraw Hill, New York, NY, 2001).

[61] S. Gordon and B. J. McBride, NASA Reference Publications 1311**,** 1-58 (1994).

[62] M. J. McBride and S. Gordon, Nasa Reference Publications 1311**,** 1-184 (1996).

[63] CEAgui; 2 ed. (1996).

[64] R. L. Myers, Y. Shishkin, O. Kordina, and S. E. Saddow, Journal of Crystal Growth 285**,** 486-490 (2005).

[65] K. L. Choy, Prog. in Mat. Sci. 48**,** 57-170 (2003).

[66] H. O. Pierson, *Handbook of Chemical Vapor Deposition: Principles, Technology and Applications* (Noyes Publications, Norwich, New York, U.S.A., 1999).

[67] Ö. Danielsson, A. Henry, and E. Janzén, Journal of Crystal Growth 243**,** 170-184 (2002).

[68] G. M. Petrov and J. L. Giuliani, Journal of Applied Physics 90**,** 619-636 (2001).

[69] M. E. Coltrin, R. J. Kee, and J. A. Miller, Journal of Electrochemical Society 133, 1206-1213 (1986).

[70] J. Meziere, M. Ucar, E. Blanket, M. Pons, P. Ferret, and L. D. Cioccio, J.Cryst. Growth 267, 436-451 (2004).

[71] S. P. Walch and C. E. Dateo, J. Phys.Chem A 105, 2015-2022 (2001).

[72] Y.-p. Wu, Combustion and Flame 122, 312-326 (2000).

[73] G. Valente, C. Cavallotti, M. Masi, and S. Carra, Journal of Crystal Growth 230, 247-257 (2001).

[74] A. Veneroni, F. Ormarini, and M. Masi, Cryst. Res. Technol. 40, 967-971 (2005).

[75] S. P. Walch and C. E. Dateo, J. Phys.Chem A 106, 2931-2934 (2002).

[76] J. M. Wittbrodt and H. B. Schlegel, Chemical Physics Letters 265, 527-531 (1997).

[77] J. M. Wittbrodt and H. B. Schlegel, Chemical Physics Letters 269, 391 (1997).

[78] S. F. Nitodas and S. V. Sotirchos, Journal of the Electrochemical Society 149, C112-C119 (2002).

[79] Y.-p. G. Wu, Fuel 83, 2237-2248 (2004).

[80] R. I. Masel, *Chemical Kinetics and Catalysis* (John Wiley and Sons, Inc, New York, NY, 2001).

[81] A. Veneroni, F. Ormarini, D. Moscatelli, M. Masi, S. Leone, M. Mauceri, G. Pistone, and G. Abbondanza, J.Cryst. Growth 275, e295-e300 (2005).

[82] A. Veneroni and M. Masi, Chemical Vapor Deposition 12, 562-568 (2006).

[83] R. B. Bird, W. E. Stuart, and E. N. Lightfoot, *Transport phenomena*, 2nd ed. (John Wiley and Sons, Inc., New York, NY, 2002).

[84] COMSOL AB, COMSOL Multiphysics Reference Manual; 3.4 ed. (2007).

[85] COMSOL AB, COMSOL Multiphysics Reference Manual; 3.4 ed. (2007).

[86] H. Nagasawa and Y.-I. Yamaguchi, Journal of Crystal Growth 115**,** 612-616 (1991).

[87] M. J. Bozack, Physica Status Solidi B 2002**,** 549-580 (1997).

[88] D. C. Montgomery, *Design and Analysis of Experiments*, 6 ed. (John Wiley & Sons, Inc, 2005).

[89] The MathWorks Inc., MATLAB; 7.2.0.232 (R2006a) ed. (2006).

Appendices

Appendix A Reactions for the gas phase model

The gas phase model used in this work utilized a set of elementary reactions describing the decomposition of the precursor gases (C_3H_8, SiH_4, HCl and H_2) and the reactions between the products of all decomposition reactions. The following sections list the reactions considered. The rate constants are written in the Arrhenius form, $k=AT^{\beta}e^{-Ea/RT}$. The units of A depend on the reaction order and are given in terms of cm^3, moles and seconds.

A.1 Hydrogen decomposition reactions

No.	Bimolecular Reactions	A	β	E (K)	Ref.
[68]	$H_2 + H_2 => 2\ H + H_2$	1.5e-9	0	48350	
[68]	$H_2 + H => 3\ H$	3.7e-10	0	48350	

Ref.	Trimolecular Reactions	A	β	E (K)	
[68]	$H + H + H_2 => H_2 + H_2$	2.7e-31	-0.6	0	
[68]	$H + H + H => H_2 + H$	2.7e-30	-1.0	0	

A.2 Propane decomposition reactions

No.	Unimolecular Reactions	A	β	E (K)	Ref.
1	$C_3H_8 => C_2H_5 + CH_3$	2.3e22	-1.8	44637	[68]
2	$C_2H_5 => C_2H_4 + H$	1.4e8	1.19	18722	[68]
3	$C_2H_4 => C_2H_2 + H_2$	1.4e12	0.44	44670	[68]
4	$C_2H_2 => C_2H + H$	1.8e15	0	62445	[68]

No.	Bimolecular Reactions	A	β	E (K)	Ref.
5	$C_2H_5 + H => 2\ CH_3$	6.1e-11	0	0	[68]
6	Reverse	1.3e-9	0	13375	[68]
7	$C_2H_5 + H => C_2H_4 + H_2$	3e-12	0	0	[68]
8	Reverse	1.1e-11	0	34300	[68]
9	$C_2H_5 + H => C_2H_6$	6e-11	0	0	[68]
10	$C_2H_5 + H_2 => C_2H_6 + H$	5.1e-24	3.6	4253	[68]
11	Reverse	2.4e-15	1.5	3730	[68]
12	$C_2H_5 + CH_3 => C_2H_4 + CH_4$	3.3e-11	0.5	0	[68]
13	$C_2H_5 + CH_3 => C_3H_8$ (Reverse R1)	7.4e-11	0	0	[68]
14	$C_2H_5 + CH_4 => C_2H_6 + CH_3$	1.4e-22	1.14	6322	[68]
15	Reverse	2.5e-31	6.0	3730	[68]
16	$C_2H_5 + C_2H => C_2H_2 + C_2H_4$	3e-12	0	0	[68]

Appendix A: (continued)

No.	Bimolecular Reactions	A	β	E (K)	Ref.
17	$C_2H_5 + C_2H_2 => C_2H + C_2H_6$	4.5e-13	0	11800	[68]
18	Reverse	6e-12	0	0	[68]
19	$C_2H_5 + C_2H_4 => C_2H_6 + C_2H_3$	1.1e-21	3.13	9063	[68]
20	Reverse	1.0e-21	3.3	5285	[68]
21	$C_2H_5 + C_2H_3 => C_2H_2 + C_2H_6$	8e-13	0	0	[68]
22	$C_2H_5 + C_2H_3 => 2C_2H_4$	8e-13	0	0	[68]
23	Reverse	8e-10	0	36000	[68]
24	$C_2H_5 + C_2H_5 => C_2H_6 + C_2H_4$	1.2e-11	0	540	[68]
25	$C_2H_4 + H => C_2H_5$ (Reverse R2)	1.4e-15	1.49	499	[68]
26	$C_2H_4 + H => C_2H_3 + H_2$	2.2e-18	2.53	6160	[68]
27	$C_2H_4 + CH_3 => C_2H_3 + CH_4$	1.1e-23	3.7	4780	[68]

No.	Bimolecular Reactions	A	β	E (K)	Ref.
28	Reverse	2.4e-24	4.02	2754	[68]
29	$C_2H_4 + C_2H_2 => 2C_2H_3$	4e-11	0	34400	[68]
30	$C_2H_3 + H => C_2H_2 + H_2$	1.6e-10	0	0	[68]
31	Reverse	4e-12	0	32700	[68]
32	$C_2H_3 + H_2 => C_4H_4 + H$	5e-20	2.63	4298	[68]
33	$C_2H_3 + CH_2 => C_2H_2 + CH_3$	3e-11	0	0	[68]
34	$C_2H_3 + CH_3 => C_2H_2 + CH_4$	6.5e-13	0	0	[68]
35	$C_2H_3 + C_2H => 2\ C_2H_2$	1.6e-12	0	0	[68]
36	Reverse	1.6e-11	0	42500	[68]
37	$C_2H_2 + H => C_2H + H_2$	1e-10	0	11200	[68]
38	Reverse	1.9e-11	0	1450	[68]
39	$C_2H_2 + H_2 => C_2H_4$ (Reverse R3)	5e-13	0	19600	[68]
40	$C_2H_2 + CH_3 => CH_4 + C_2H$	3e-13	0	8700	[68]
41	Reverse	3e-12	0	250	[68]
42	$C_2H + H => C_2H_2$ (Reverse R4)	3e-10	0	0	[68]
43	$C_2H + CH_2 => C_2H_2 + CH$	3e-11	0	0	[68]
44	$CH_4 + H => CH_3 + H_2$	2.2e-20	3.0	4045	[68]
45	Reverse	4.8e-22	3.12	4384	[68]
46	$CH_4 + CH => C_2H_5$	2.7e-10	0	0	[68]
47	$CH_4 + CH => C_2H_4 + H$	5e-11	0	200	[68]
48	$CH_4 + CH_2 => C_2H_6$	1.7e-11	0	0	[68]
49	$CH_4 + CH_2 => 2CH_3$	2.1e-11	0.5	0	[68]
50	$CH_4 + CH_3 => C_2H_5 + H_2$	1.7e-11	0	11500	[68]
51	$CH_3 + H => CH_2 + H_2$	3.3e-11	0	0	[68]
52	Reverse	3.3e-11	0.5	0	[68]
53	$CH_3 + H => CH_4$	2e-9	-0.4	0	[68]
54	$CH_3 + CH => C_2H_3 + H$	5e-11	0	0	[68]
55	$CH_3 + CH_2 => C_2H_4 + H$	3e-11	0	0	[68]

Appendix A: (continued)

56	$CH_3 + CH_3 => C_2H_6$	1.7e-9	-0.64	0	[68]
No.	Bimolecular Reactions	A	β	E (K)	Ref.
57	$CH_2 + H => CH + H_2$	5e-11	0	0	[68]
58	$CH_2 + CH => C_2H_2 + H$	6.6e-11	0	0	[68]
59	$CH_2 + CH_2 => C_2H_4$	1.7e-12	0	0	[68]
60	$CH_2 + CH_2 => C_2H_2 + 2\ H$	1.8e-10	0	0	[68]
61	$CH_2 + CH_2 => C_2H_2 + H_2$	2e-11	0	400	[68]
62	$CH + CH => C_2H_2$	2e-10	0	0	[68]

No.	Unimolecular Reactions	A	β	E (K)	Ref.
63	$CH_4 => CH_3 + H$	8.3e13	0	52246	[68]
64	$C_2H_6 => 2\ CH_3$	1.2e22	-1.79	45834	[68]

A.3 Silane decomposition reactions

No.	Unimolecular Reactions	A	β	E(K)	Ref.
1	$SiH_4 => SiH_2 + H_2$	3.120e9	1.7	27550	[67]
No.	Unimolecular Reactions	A (1/s)	β	E(K)	Ref.
2	$SiH_4 => SiH_3 + H$	3.690e15	0	46830	[67]
3	Reverse	1.323e14	0	140	[67]

No.	Bimolecular Reactions	A	β	E (K)	Ref.
4	$SiH_2 + H => SiH_3$	3.810e13	0	1000	[67]
5	$SiH_2 + H => SiH + H_2$	1.204e13	0	0	[67]
6	$SiH_2 + SiH_2 => Si_2H_2 + H_2$	6.5e14	0	0	[67]
7	$SiH_3 + H => SiH_2 + H_2$	1.204e13	0	0	[67]
8	$SiH_3 + SiH_2 => Si_2H_5$	6.580e12	0	1000	[67]
9	$SiH_3 + SiH_3 => SiH_4 + SiH_2$	1.8e13	0	0	[67]
10	$SiH + H_2 => SiH_3$	3.45e13	0	1000	[67]
11	$Si_2H_5 + SiH_3 => SiH_2 + Si_2H_6$	9.033e13	0	0	[67]
12	$Si_2H_6 + H => Si_2H_5 + H_2$	1.445e14	0	1250	[67]
13	$Si_2H_6 + H => SiH_3 + SiH_4$	1.445e14	0	1250	[67]
14	$Si_2H_6 + SiH_3 => SiH_4 + Si_2H_5$	2.409e14	0	2500	[67]
15	$SiH_4 + H => SiH_3 + H_2$	1.686e13	0	1250	[67]
16	$SiH_4 + SiH => SiH_3 + SiH_2$	1.38e12	0	5640	[67]
17	$SiH_4 + SiH => Si2H_4 + H$	3e14	0	4535	[67]
18	$SiH_4 + SiH => Si_2H_5$	4.139e14	0	0	[67]
19	$Si2H_4 + H_2 => SiH_2 + SiH_4$	9.41e13	0	0	[67]
20	Reverse	9.43e10	1.1	2916	[67]
21	$Si_2H_4 + SiH_4 => SiH_2 + Si_2H_6$	1.73e14	0.4	0	[67]
22	Reverse	2.65e15	0.1	4267	[67]

Appendix A: (continued)

No.	Unimolecular Reactions	A	β	E (K)	Ref.
23	Si2H4 => Si2H2 + H2	3.16e14	0	26690	67
24	Reverse	2.450e14	0	1000	67
25	Si_2H_4 => Si + SiH_4	1.420e13	0.54	28980	67
26	Si_2H_6 => SiH_2 + SiH_4	1.810e10	1.7	27280	67
27	Si_2H_6 =>Si_2H_4 + H_2	9.090e9	1.8	27290	67

No.	Bimolecular Reactions	A	β	E(K)	Ref.
28	SiH_2 + Si => Si_2 + H_2	1.500e14	0	0	67
29	SiH_2 + Si => Si_2H_2	7.240e12	0	1000	67
30	SiH_4 + Si => 2 SiH_2	9.310e12	0	1000	67
31	$Si2H_6$ + Si => SiH_2 + Si_2H_4	1.300e15	0	6345	67
32	Si_2 + H => Si + SiH	5.150e13	0	2670	67
33	Si_2 + H_2 => 2 SiH	1.540e13	0	20140	67
34	Si_2 + H_2 => Si_2H_2	1.540e13	0	1000	67
35	Si_2 +SiH_2 => Si_3 + H_2	3.550e11	0	1000	67
36	Bimolecular Reactions	A	β	E(K)	Ref.
37	Si_2 + Si => Si_3	2.060e12	0	12135	67
38	Si_3 + Si => 2 Si_2	2.060e12	0	12135	67
No.	Bimolecular Reactions	A (cm^3/s)	β	E(K)	Ref.
39	Si_3 + H2 => Si + Si_2H_2	9.790e12	0	23770	67
40	Si_3 + SiH_2 => Si_2 + Si_2H_2	1.430e11	0	8160	67

No.	Unimolecular Reactions	A	β	E (K)	Ref.
41	Si_2 => 2 Si	1e15	0	37460	67

A.4 Hydrogen chloride decomposition reactions

No.	Unimolecular Reactions	A	β	E (K)	Ref.
1	HCl => H + Cl	4.365e13	0	41142	73

No.	Bimolecular Reactions	A	β	E (K)	Ref.
2	H + Cl => HCl (Reverse R1)	7.20e21	-2.0	0	72
3	Cl + H2 => HCl + H	4.786e13	0	2647.8	73
4	Cl + Cl => Cl_2	2.34e14	0	-902.1	72
5	H + Cl2 => HCl + Cl	8.59e13	0	589.37	72

Appendix A: (continued)

A.5 Organosilicon reactions

No.	Bimolecular Reactions	A	β	E (K)	Ref.
1	$SiH_3 + CH_3 => CH_4 + SiH_2$	3.372e13	0	-360	[67]
2	$SiH_4 + CH_3 => CH_4 + SiH_3$	7.762e11	0	3515	[67]

No.	Bimolecular Reactions	A	β	E (K)	Ref.
3	$SiH_4 + C2H_5 => C2H_6 + SiH_3$	5.370e11	0	3650	[67]
4	$Si_2 + CH_4 => Si_2C + 2H_2$	3.011e15	0	10000	[67]

A.6 Chlorinated species reactions

No.	Bimolecular Reactions	A	β	E (K)	Ref.
1	$Si + HCl => SiCl + H$	1.585e-9	0	6954.5	[74]
2	$Si + HCl => SiHCl$	4.169e11	0.5	0	[74]
3	$SiCl + HCl => SiCl_2 + H$	1.072e-10	0	9814.8	[74]
4	$SiCl + HCl => SiHCl_2$	4.193e-12	0	2372.6	[75]
5	$SiCl + H_2 => SiClH_2$	2.053e-11	0	31669	[75]
6	$SiCl + H_2 => SiHCl + H$	6.681e-10	0	16406	[75]
7	$SiCl + H_2 => SiH + HCl$	3.149e-11	0	15744	[75]
8	$SiHCl + HCl => SiCl_2 + H_2$	1.169e11	0.5	0	[74]
9	$SiHCl + HCl => SiH_2Cl_2$	2.455e-3	0	5137.1	[77]
10	$SiHCl + H => SiCl + H_2$	3.647e-16	1.736	-609.3	[75]
11	$SiHCl + H => SiH + HCl$	1.404e-10	0	8044.3	[75]
12	$SiH + HCl => SiH_2Cl$	1.106e-18	2.158	-1023	[75]
13	$SiH + HCl => SiHCl + H$	8.414e-11	0	8616	[75]
14	$SiH + HCl => SiCl + H_2$	1.559e-18	1.984	859.6	[75]
15	$SiH_2Cl_2 + HCl => SiHCl_3 + H2$	2.49e29	0	24957	[78]
16	$SiCl_2 + H => SiCl + HCl$	4.068e-10	0	9498.4	[75]
17	$SiCl_2 + H_2 => SiH_2Cl_2$	2.291e-3	0	19737	[77]
18	$SiHCl_3 + H => SiCl_3 + H_2$	2.455e12	0	1276.1	[74]
19	Reverse	1.4e10	0	472.8	[78]
20	$SiHCl_3 + CH_3 =>CH_4 + SiCl_3$	6.760e7	0	2162.6	[78]
21	$SiHCl_3 + Cl => HCl + SiCl_3$	7.230e9	0	0	[78]

No.	Unimolecular Reactions	A	β	E (K)	Ref.
22	$SiH_2Cl => SiH + HCl$	1.869e14	0	30971	[75]
23	$SiH_2Cl => SiCl + H_2$	3.975e13	0	46776	[75]
24	$SiHCl_2 => SiCl + HCl$	3.510e13	0	43047	[75]
25	$SiH_2Cl_2 => SiCl_2 + H_2$	7.943e13	0	37310	[76]
26	$SiH_2Cl_2 => SiHCl + HCl$	6.761e14	0	36564	[76]

Appendix A: (continued)

No.	Unimolecular Reactions	A	β	E (K)	Ref.
27	$SiHCl_3 => SiCl_2 + HCl$	4.898e14	0	37106	[74]

No.	Bimolecular Reactions	A	β	E (K)	Ref.
28	$CH_4 + Cl => CH_3 + HCl$	5e13	0	1960.5	[79]
29	$C_2H_2 + Cl => C_2H + HCl$	1.58e14	0	13531	[79]
30	$C_2H_4 + Cl => C_2H_3 + HCl$	1e14	0	29.3e3	[79]
31	$C_2H_3 + Cl_2 => C_2H_3Cl + Cl$	5.25e12	0	-240.6	[79]

No.	Bimolecular Reactions	A	β	E (K)	Ref.
32	$C_2H_5 + Cl_2 => C_2H_5Cl + Cl$	7.58e12	0	-120.3	[79]
33	$C_2H_6 + Cl => C_2H_5 + HCl$	4.64e13	0	84.2	[79]
34	$C_2H_3Cl + CH_3 => C_2H_3 + CH_3Cl$	3.15e11	0	12484	[79]
35	$C_2H_3Cl + Cl => CHCHCl + HCl$	5.00e13	0	3524.2	[79]
36	$C_2H_3Cl + Cl => CH_2CCl + HCl$	3.00e13	0	2766.4	[79]
37	$C_2H_3Cl + H => C_2H_3 + HCl$	1.00e13	0	3271.6	[79]
38	$C_2H_3Cl + H => CH_2ClCH_2$	8.25e9	-0.1	1768.1	[79]
39	$C_2H_3Cl + H =>C_2H_4 + Cl$	2.92e13	-0.1	2970.9	[79]
40	$CH_3Cl + H => CH_3 + HCl$	3.72e13	0	3824.9	[79]
41	$CH_3Cl + Cl => CH_2Cl + HCl$	3.20e13	0	13000	[79]
42	$CH_3Cl + Cl => CH_3 + Cl_2$	1.00e14	0	12581	[79]
43	$CH_3Cl + CH_3 => CH_4 + CH_2Cl$	3.31e11	0	4727	[79]
44	$CH_2Cl + H => CH_3Cl$	8.00e26	-5.05	1383.2	[72]
45	$CH_2Cl + H => CH_3 + Cl$	2.18e5	-0.24	108.3	[72]
46	$CH_2Cl + H_2 => CH_3Cl + H$	1.79e12	0	6567.2	[72]
47	$CH_2Cl + CH_3 => C_2H_5Cl$	1.62e43	-9.89	3800.2	[72]
48	$CH_2Cl + CH_3 => C_2H_5 + Cl$	2.68e14	-0.57	1202.8	[72]
49	$CH_2Cl + CH_3 => C_2H_4 + HCl$	4.26e19	-2.02	1816.2	[72]
50	$CH_2Cl + CH_2Cl => C_2H_3Cl + HCl$	4.21e22	-3.02	1900.4	[72]

	Unimolecular Reactions	A	β	E (K)	Ref.
51	$C_2H_3Cl => C_2H_2 + HCl$	7.64e33	-6.3	36492	[79]
52	$C_2H_3Cl => C_2H_3 + Cl$	5.15e45	-10	50529	[79]
53	$C_2H_5Cl => C_2H_4 + HCl$	6.03e27	-4.5	31164	[79]
54	$C_2H_5Cl => C_2H_5 + Cl$	7.62e49	-11	46078	[79]
55	$CH_3Cl => CH_3 + Cl$	3.71e38	-7.61	45188	[72]

Appendix B Reactions for the surface reaction model

The main surface reactions involved in the 3C-SiC deposition are listed in the following sections. S_{si} and S_c stand for Si and C surface sites, while a species marked with an asterisk (*) indicates an adsorbed species. The rate constants are written in the form $k = AT^{\beta}e^{-Ea/RT}$. The units of A are given in terms of [mol cm^{-2} s^{-1}], gas and surface concentrations units are [mol cm^{-3}] and [mol cm^{-2}], respectively. Subscripts S and C are for chloride on Si or C surface sites respectively.

B.1 Carbon species adsorption

No.	Surface Reactions	A	β	E(K)	Ref.
1	$CH_4 + S_{si}$ --> $C^* + 2H_2$	2.39 e09	0.5	0	82
2	$CH_3 + S_{si}$ --> $CH^* + H_2$	8.51 e11	0.5	0	
3	$CH_2 + S_{si}$ --> $C^* + H_2$	8.91 e11	0.5	0	
4	$CH + S_{si}$ --> CH^*	9.12 e11	0.5	0	
5	$C_2H_5 + 2S_{si}$ --> $C^* + CH^* + 2H_2$	5.75 e20	0.5	0	
6	$C_2H_4 + 2S_{si}$ --> $2C^* + 2H_2$	9.33 e17	0.5	0	
7	$C_2H_3 + 2S_{si}$ --> $C^* + CH^* + H_2$	5.88 e20	0.5	0	
8	$C_2H_2 + 2S_{si}$ --> $C^* + H_2$	1.20 e19	0.5	0	

B.2 Silicon species adsorption

No.	Surface Reactions	A	β	E(K)	Ref.
9	$SiH_2 + S_c$ --> SiH_2^*	6.02 e11	0.5	0	82
10	$SiH_4 + S_c$ --> $SiH_2^* + H_2$	3.16 e10	0.5	9399.657	
11	$SiH_3 + S_c$ --> $SiH^* + H_2$	6.02 e11	0.5	0	
12	$SiH + S_c$ --> SiH^*	6.16 e11	0.5	0	
13	$Si + S_c$ --> Si^*	6.30 e11	0.5	0	
14	$Si_2H_5 + 2S_c$ --> $SiH^* + Si^* + 2H_2$	3.89 e20	0.5	0	
15	$Si_2 + 2S_c$ --> $2Si^*$	4.07 e20	0.5	0	
16	$Si_2H_6 + 2S_c$ --> $2Si^* + 3H_2$	2.08 e20	0.5	9399.657	
17	$Si_2H_4 + 2S_c$ --> $2SiH_2^*$	3.98 e20	0.5	0	
18	$Si_2H_2 + 2S_c$ --> $2SiH^*$	4.07 e20	0.5	0	
19	$Si_3 + 3S_c$ --> $3Si^*$	2.29 e29	0.5	0	
20	$H_2 + 2S_c$ --> $2H^*$	2.29 e11	0.5	0	

Appendix B: (continued)

B.3 Mixed species adsorption

No.	Surface Reactions	A	β	E(K)	Ref.
21	$SiC_2 + S_c + 2S_{si}$ --> Si* + 2C*	8.70 e20		0	82
22	$Si_2C + 2S_c + S_{si}$ --> 2Si* + C*	1.14 e21	0.5	0	
23	$SiC_2H_2 + 2S_{si} + S_c$ --> C* + CH* + SiH*	4.36 e20	0.5	0	

B.4 Chlorinated species adsorption

No.	Surface Reactions	A	β	E(K)	Ref.
24	$SiHCl_3 + 2S_{si} + 2S_c$ --> SiCl* + H* + $2Cl_s$*	2.63 e16	0.5	0	82
25	$SiH_2Cl_2 + S_{si} + 3S_c$ --> SiCl* + 2H* + Cl_s*	3.80 e08	0.5	0	
26	$SiCl_4 + 2S_{si} + 2S_c$ --> SiCl* + Cl_c* + $2Cl_s$*	2.34 e16	0.5	0	
27	$SiCl_2 + 2S_c$ --> SiCl* + Cl_c*	3.09 e19	0.5	0	
28	$SiCl_2 + S_c + S_{si}$ --> SiCl* + Cl_s*	3.09 e19	0.5	0	
29	$HCl + S_{si} + S_c$ --> CH* + Cl_s*	3.54 e12	0.5	0	
30	$SiCl + S_c$ --> SiCl*	4.16 e11	0.5	0	
31	$SiHCl + 2S_c$ --> SiCl* + H*	3.31 e20	0.5	0	
32	$SiHCl + S_c$ --> Si* + HCl	4.16 e12	0.5	0	

B.5 Reaction between surface and gaseous species

No.	Surface Reactions	A	β	E(K)	Ref.
33	$H + CH^* \rightarrow C^* + H_2$	3.54 e12	0.5	0	82
34	$H + C^* \rightarrow CH^*$	3.54 e12	0.5	0	
35	$CH^* \rightarrow 0.5H_2 + C^*$	1.00 e23	0.5	28735.43	
36	$CH^* + H_2 \rightarrow S_{si} + CH_3$	2.29 e11	0.5	44262.63	
37	$CH^* + 0.5H_2 \rightarrow C^* + H_2$	2.29 e12	0.5	0	
38	$C^* + 0.5H_2 \rightarrow CH^*$	2.29 e12	0.5	0	
39	$SiCl^* + 0.5H_2 \rightarrow Si^* + HCl$	2.34 e15	0.5	30194.85	
40	$SiCl^* + H \rightarrow Si^* + HCl$	3.31 e15	0.5	30194.85	
41	$SiCl^* + HCl \rightarrow SiCl_2 + H + S_c$	3.54 e10	0.5	0	
42	$2Clc^* + H_2 \rightarrow 2HCl + 2S_c$	2.34 e12	0.5	39545.19	

Appendix B: (continued)

No.	Surface Reactions	A	β	E(K)	Ref.
43	$Cl_c^* + H \rightarrow HCl + 2S_c$	3.16 e12	0.5	0	82
44	$2Cl_c^* + SiCl_2 \rightarrow SiCl_4 + 2S_c$	3.23 e11	0.5	12581.19	
45	$2Cl_s^* + H_2 \rightarrow 2HCl + 2S_{si}$	2.34 e12	0.5	45194.65	
46	$Cl_s^* + H \rightarrow HCl + S_{si}$	3.16 e12	0.5	0	
47	$Cl_s^* + Cl_c^* + H_2 \rightarrow 2HCl + S_c + S_{si}$	2.34 e12	0.5	42368.41	
48	$Cl_s^* + Cl_c^* + SiCl_2 \rightarrow SiCl_4 + S_c + S_{si}$	3.23 e10	0.5	12581.19	

B.6 Reaction between surface species

No.	Surface Reactions	A	β	E(K)	Ref.
49	$2SiH^* \rightarrow Si^* + H_2$	1.00 e25	0	30698.1	82
50	$SiH_2^* \rightarrow Si^* + H_2$	1.00 e19	0	30698.1	
51	$SiCl^* + Cl_c^* \rightarrow SiCl_2 + 2S_c$	1.00 e19	0	10112.76	
52	$SiCl^* + Cl_s^* \rightarrow SiCl_2 + S_{si} + S_c$	1.00 e19	0	45194.65	
53	$2SiCl^* \rightarrow SiCl_2 + Si^* + 2S_c$	1.00 e19	0	45194.65	
54	$H^* + SiCl^* \rightarrow HCl + Si^* + S_c$	1.00 e23	0	25165.4	
55	$CH^* + Cls^* \rightarrow HCl + C^* + S_{si}$	1.00 e19	0	45194.65	
56	$Si^* + Cl_s^* \rightarrow SiCl^* + S_{si}$	1.00 e17	0	0	
57	$H^* + Cl_s^* \rightarrow HCl + S_c + S_{si}$	1.00 e23	0	45194.65	
58	$CH^* + Cl_c^* \rightarrow HCl + C^* + S_c$	1.00 e18	0	42368.41	
59	$Si^* + Cl_c^* \rightarrow SiCl^* + S_c$	1.00 e17	0	0	
60	$H^* + Cl_c^* \rightarrow HCl + 2S_c$	1.00 e23	0	42368.41	
61	$H^* + H^* \rightarrow H_2 + 2S_c$	1.00 e24	0	30698.1	
62	$CH^* + CH^* \rightarrow 2C^* + H_2$	1.00 e23	0	30698.1	
63	$CH^* + H^* \rightarrow H_2 + C^* + S_c$	1.00 e23	0	30698.1	
64	$CH^* + CH^* \rightarrow C_2H_2 + 2S_{si}$	1.00 e23	0	44262.63	

B.7 Desorption reactions

No.	Surface Reactions	A	β	E(K)	Ref.
65	$Si^* \rightarrow S_2 + Si$	1.00 e13	0	20381.53	82
66	$2Si^* + C^* \rightarrow Si_2C + 2S_c + S_{si}$	1.00 e24	0	0	
67	$Si^* + 2C^* \rightarrow SiC_2 + S_c + 2S_{si}$	1.00 e24	0	0	

Appendix B: (continued)

B.8 HCl etching reaction

No.	Surface Reactions	A	β	E(K)	Ref.
68	HCl + SiC(b) --> SiCl* + CH*	3.54 e10	0.5	0	[82]

B.9 Growth reactions

No.	Surface Reactions	A	β	E(K)	Ref.
69	$Si^* + C^* \rightarrow SiC_{(b)} + S_{si} + S_c$	1.00 e17	0	0	[82]
70	$2Si^* + C^* \rightarrow Si_2C_{(b)} + 2S_c + S_{si}$	1.00 e23	0	0	
71	$Si^* + 2C^* \rightarrow SiC_{2(b)} + S_c + 2S_{si}$	1.00 e23	0	0	
72	$SiCl^* + C^* \rightarrow SiC_{(b)} + S_c + S_{si} + Cl$	1.00 e17	0	0	
73	$Si^* + CH^* \rightarrow SiC_{(b)} + S_{si} + S_c + H$	1.00 e17	0	0	
74	$SiH^* + CH^* \rightarrow SiC_{(b)} + S_{si} + S_c + {}_2H$	1.00 e17	0	0	
75	$SiH^* + C^* \rightarrow SiC_{(b)} + S_{si} + S_c + H$	1.00 e17	0	0	
76	$SiCl^* + CH^* \rightarrow SiC_{(b)} + HCl + S_{si} + S_c$	1.00 e17	0	0	

Appendix C Simulation procedure

In order to perform the simulations the COMSOL Reaction Engineering Lab and COMSOL Multiphysics have to be used iteratively. The following sections summarize the main steps necessary to develop the model and obtain a solution.

C.1 Modeling using COMSOL Multiphysics

- Draw the desired reactor geometry
- Open Reaction Engineering Lab from COMSOL Multiphysics

C.2 Modeling using COMSOL Reaction Engineering Lab

Gas phase reactions

- Choose model/model
- Select the calculate thermodynamic properties and calculate transport properties
- Type process temperature and pressure
- Obtain gas phase reaction model
- Input gas phase reactions
- Input Arrhenius parameters: A, n, E_a
- Input species molecular weight
- Input species initial concentration
- Input species transport properties: ε\κ and σ
- Input species thermo parameters: NASA polynomial coefficients
- Select H_2 as solvent and choose lock concentration/activity
- Compute the solution

C.3 Exporting Model to COMSOL Multiphysics

- File/Export/Model to COMSOL Multiphysics
- Choose Geom1(2D)
- Select export mass balance

Appendix C: (continued)

- Choose application mode: Convection and Diffusion:New
- Type gas_mass in group name
- Select export energy balance
- Choose application mode: Convection and Conduction: New
- Type gas_energy in group name
- Select export momentum balances
- Choose application mode: Incompressible Navier-Stokes: New
- Type gas_momentum in group name
- Click export

C.4 Modeling using COMSOL Reaction Engineering Lab

Adsorption/Desorption

- Type T_surf in T edit field
- Type p_0 in p edit field
- Obtain surface reaction model
- Input surface phase reactions
- Input Arrhenius parameters: A, n, E_a
- Input species molecular weight
- Input species initial concentration

C.5 Export Model to COMSOL Multiphysics

- File/Export/Model to COMSOL Multiphysics
- From domain level list choose: Interior boundary
- Clear export energy balance check box
- Clear export energy balance check box
- Select export mass balance
- Choose application mode: Convection and diffusion(chcd)

- Type boundary_mass in group name edit field
- Click export

C.6 Modeling using COMSOL Multiphysics

- Verify that the model contains: Convection and Diffusion(chcd), Convection and Conduction(chcc) and Incompressible Navier-Stokes(chns)
- Type model global constants
- Choose: Convection and Diffusion(chcd)
- Select appropriate subdomain settings and boundary conditions
- Choose: Convection and Conduction(chcc)
- Choose: Incompressible Navier-Stokes(chns)
- Choose: Incompressible Navier-Stokes(chns)
- Select appropriate subdomain settings and boundary conditions
- Click ok

C.7 Mesh Generation

- Choose Mesh/Free Mesh parameters
- On global page, select Fine
- On Boundary page, select the substrate, then type 2e-3 in maximum element size
- Click ok

C.8 Computing the solution

- Click solver parameters button
- From solver list, select stationanry
- Click the advance tab and clear the Stop if error due to undefined operation checkbox
- Click Ok

Appendix C: (continued)

- Choose Solve/Solver manager
- On the Solve For page, select Convection and Conduction and Non-Isothermal Flow
- On the script page, select Automatically add commands when solving checkbox
- Click Apply, then click Solve. This step solves the momentum and energy balances to get the good initial value.
- On the Initial Value page, select Current Solution in the Initial Value area
- On the Solve For page, select only Convection and Diffusion
- Click Apply and then Click Solve to find the mass balance
- Finally, select all the application modes by clicking the Solve For tab and selecting Geom 1 folder.
- Click Aplly then Click Solve
- Now that the final solution have been obtained, go to Script page and clear the Automatically add commands when solving check box. This settings allow you to used the same solution technique if you which to alter parameters in the model and solve again.
- Save your document

Appendix D Statistical Design of Experiments (DOE)

D.1 2^{5-2} fractional factorial DOE construction

A fractional factorial design of experiments is a variation of the full factorial DOE in which only a subset of the experimental matrix is performed. A factorial design is an experimental strategy in which factors are varied together instead of one at a time. In this task; two factors levels will be considered. This means that a full factorial will explore all possible combinations of the factors levels; in this case 2^k possible combinations, where k is the number of factors under consideration and the number 2 represents the two levels for each factor.

The following discussion is intended to explain how fractional DOE's are constructed such that the experimenter can determine which fraction of the full factorial DOE has to be conducted. The following sample will be based on the construction of a one quarter fractional factorial design with 5 factors, each one studied at 2 levels (2^{5-2}) for a total of 8 experimental runs (henceforth referred to as simply runs) plus the center points instead of 32 runs if the full factorial design was applied.

To construct the design, what is called a defining relation (I) must be specified. I=ABD and I=ACE were chosen as design generators. These generators produce a design of experiments of resolution III which is the highest resolution for the quarter fractional factorial DOE in this case. By resolution III DOE is meant that no main effects are aliased with any other main effects but main effects are aliased with two-factor interactions and two factor interactions may be aliased to each other. For more details the reader is encourage to refer to external sources.[88]

In order to determine the runs to be performed the 2^5 full factorial DOE matrix is specified first. Then the quarter of the full factorial to be considered is determined based on the already defined generators I=ABD and I=ACE. This is shown in Table A.1. In the combination column represents the total number of combinations for the 2^5 full factorial DOE, equivalent to 32 runs. The columns A to E, represent the factors under

consideration. The numbers +1 and -1 represent the low and the high level value of each factor. The table is then filled by assigning a value of +1 to the corresponding factor specified on each row of the combination column and a -1 to the remaining factors. Finally, the design generators are used to determine the runs to be considered, in this case the runs where ABD, ACE are positives (highlighted). Since this is a quarter of the design then the other three quarters can be identified by using the following relationship combinations I=ABD with I= -ACE, I= -ABD with I=ACE and I= -ABD with I= -ACE. As far as the design selection, which quarter should be run should not affect the final analysis of the experimental matrix or the conclusions that are drawn from it.

Finally, once the design is constructed and executed the results are then analyzed via statistical techniques. Typically the analysis of variance (ANOVA) test is used. ANOVA refers to a collection of statistical model which compare means by splitting the overall observed variance into different parts due to different factors which are estimated and/or tested. Further details on how the ANOVA analysis is performed can be found elsewhere.[88]

Table D.1 Construction of the 2^{5-2} fractional factorial design (highlighted) from the 2^5 full factorial DOE when generators are I=ABD and I=ACE.

Run	Combination	A	B	C	D	E	ABD	ACE
1	-1	-1	-1	-1	-1	-1	-1	-1
2	a	1	-1	-1	-1	-1	1	1
3	b	-1	1	-1	-1	-1	1	-1
4	c	-1	-1	1	-1	-1	-1	1
5	d	-1	-1	-1	1	-1	1	-1
6	e	-1	-1	-1	-1	1	-1	1
7	ab	1	1	-1	-1	-1	-1	1
8	ac	1	-1	1	-1	-1	1	-1
9	ad	1	-1	-1	1	-1	-1	1

Appendix D: (continued)

Run	Combination	A	B	C	D	E	ABD	ACE
10	ae	1	-1	-1	-1	1	1	-1
11	bc	-1	1	1	-1	-1	1	1
12	bd	-1	1	-1	1	-1	-1	-1
13	be	-1	1	-1	-1	1	1	1
14	cd	-1	-1	1	1	-1	1	1
15	ce	-1	-1	1	-1	1	-1	-1
16	de	-1	-1	-1	1	1	1	1
17	abc	1	1	1	-1	-1	-1	-1
18	abd	1	1	-1	1	-1	1	1
19	abe	1	1	-1	-1	1	-1	-1
20	acd	1	-1	1	1	-1	-1	-1
21	ace	1	-1	1	-1	1	1	1
22	ade	1	-1	-1	1	1	-1	-1
23	bcd	-1	1	1	1	-1	-1	1
24	bce	-1	1	1	-1	1	1	-1
25	bde	-1	1	-1	1	1	-1	1
26	cde	-1	-1	1	1	1	1	-1
27	abcd	1	1	1	1	-1	1	-1
28	abce	1	1	1	-1	1	-1	1
29	abde	1	1	-1	1	1	1	-1
30	acde	1	-1	1	1	1	-1	1
31	bcde	-1	1	1	1	1	-1	-1
$32 = 2^5$	abcde	1	1	1	1	1	1	1

About the Author

Meralys Reyes-Natal received a Bachelor's Degree in Chemical Engineering from the University of Puerto Rico in 2003. Since that time she has been pursuing her Doctor of Philosophy degree in Chemical Engineering at the University of South Florida. Her research focus is on the heteroepitaxial growth of 3C-SiC layers by CVD using the SiH_4-C_3H_8-HCl-H_2 chemistry. This work was performed in the department of Electrical Engineering and has been supported by federal and industrial grants. Her dissertation work has been presented at the 2005 International Conference on Silicon Carbide and Related Materials (ICSCRM) (Pittsburg, PA), 2006 Spring Materials Research Society (MRS) meeting (San Francisco, CA), 2006 European Conference on Silicon Carbide and Related Materials (ECSCRM) (New Castle, UK), and lastly at the 2007 Electronic Materials Conference (EMC) (Notre Dame, IN).